

PHRAGMITES AUSTRALIS DETECTION USING RADARSAT-2: SINGLE-POLARIZED ANALYSIS
AND FULLY POLARIMETRIC DECOMPOSITION

By

Nicholas Ochoski, B.A. (Hons.)

A thesis submitted to

The Faculty of Graduate Studies and Research

In partial fulfillment of the requirements of the degree of

Master of Science

Department of Geography and Environmental Studies

Carleton University

Ottawa, Ontario

© Nicholas Ochoski, 2010



Library and Archives
Canada

Published Heritage
Branch

395 Wellington Street
Ottawa ON K1A 0N4
Canada

Bibliothèque et
Archives Canada

Direction du
Patrimoine de l'édition

395, rue Wellington
Ottawa ON K1A 0N4
Canada

Your file *Votre référence*
ISBN: 978-0-494-71593-2
Our file *Notre référence*
ISBN: 978-0-494-71593-2

NOTICE:

The author has granted a non-exclusive license allowing Library and Archives Canada to reproduce, publish, archive, preserve, conserve, communicate to the public by telecommunication or on the Internet, loan, distribute and sell theses worldwide, for commercial or non-commercial purposes, in microform, paper, electronic and/or any other formats.

The author retains copyright ownership and moral rights in this thesis. Neither the thesis nor substantial extracts from it may be printed or otherwise reproduced without the author's permission.

In compliance with the Canadian Privacy Act some supporting forms may have been removed from this thesis.

While these forms may be included in the document page count, their removal does not represent any loss of content from the thesis.

AVIS:

L'auteur a accordé une licence non exclusive permettant à la Bibliothèque et Archives Canada de reproduire, publier, archiver, sauvegarder, conserver, transmettre au public par télécommunication ou par l'Internet, prêter, distribuer et vendre des thèses partout dans le monde, à des fins commerciales ou autres, sur support microforme, papier, électronique et/ou autres formats.

L'auteur conserve la propriété du droit d'auteur et des droits moraux qui protègent cette thèse. Ni la thèse ni des extraits substantiels de celle-ci ne doivent être imprimés ou autrement reproduits sans son autorisation.

Conformément à la loi canadienne sur la protection de la vie privée, quelques formulaires secondaires ont été enlevés de cette thèse.

Bien que ces formulaires aient inclus dans la pagination, il n'y aura aucun contenu manquant.


Canada

ABSTRACT

Wetlands are a vital ecological component and protecting them from invasive vegetation species is of paramount importance. This research investigated the capacity for single-polarized and fully polarimetric radar (RADARSAT-2) to be used for the purpose of detecting the invasive common reed (*Phragmites australis*) in southern Ontario marshlands. Using single-polarized 3m pixel radar imagery, it was shown that small, circular patches of *Phragmites australis* could be distinguished from neighbouring vegetation types with an accuracy of approximately 75%; the best results were achieved using a combination of incidence angles and polarizations.

Fully polarimetric 8m pixel imagery was found to be capable of distinguishing larger patches of *Phragmites australis* using advanced decomposition (Cloude-Pottier, Touzi) parameters. Steep incidence angle, spring season imagery was found to produce the highest overall detection accuracies (~75%). The physical characteristics of the wetland vegetation (density, water level, height) played a direct role in the detection of *Phragmites australis*.

ACKNOWLEDGEMENTS

This thesis was made possible through the guidance, support and contributions of several people and institutions. The National Wildlife Research Centre at Environment Canada provided funding for the acquisition of remote sensing data and field work efforts. Special thanks go to Jason Duffe at Environment Canada for arranging funding and providing me with access to a workspace and the equipment needed to complete this research. Thanks to Evan Seed, Blair Kennedy, and Sarah Banks for their contributions to the planning and field work efforts and for providing support throughout the entire process; I could not have completed this project without their backing.

Many thanks to the *Department of Geography and Environmental Studies* at Carleton University, in particular Dr. Doug King and Dr. Scott Mitchell. I would like to sincerely thank Doug King for his guidance and support throughout the process and for acting as a mentor to me throughout my academic career. Thanks to both Doug and Scott for their comments and suggestions that have greatly improved the quality of this research effort.

A sincere thank you goes to my parents for always supporting me in my many endeavours. Without their unwavering support and encouragement I would not have achieved much of what I have over the course of my academic career. Finally, thank you to the other grad students in the Geography department. These past two years would not have been nearly as much fun without our many heated debates and celebrations.

Table of Contents

ABSTRACT	ii
ACKNOWLEDGEMENTS	iii
TABLE OF CONTENTS	iv
LIST OF TABLES	vii
LIST OF FIGURES	ix
1.0 INTRODUCTION	1
1.1 Objectives	6
1.2 Thesis Structure and Datasets	7
2.0 BACKGROUND	8
2.1 Invasive Common Reed (<i>Phragmites australis</i>)	8
2.1.1 Detrimental Effects of <i>P. australis</i>	13
2.1.2 Benefits of <i>P. australis</i>	14
2.2 National Wildlife Areas	15
2.3 Single-Polarized and Fully Polarimetric Radar Remote Sensing	16
2.4 Radar Remote Sensing of Wetland Ecosystems	25
2.4.1 Wetland Classification Based on Physical Characteristics	26
2.4.2 Radar Remote Sensing of Wetland Vegetation Types	28
2.4.3 Radar Remote Sensing of Other Wetland Variables	31
2.5 Deriving Information from Radar Backscatter: Polarimetric Plots	32
2.6 Incoherent Target Decomposition	34
2.6.1 Van Zyl Decomposition	35
2.6.2 Freeman-Durden Decomposition	36
2.6.3 Cloude-Pottier (H/α) Decomposition	36
2.6.4 Touzi Decomposition	39

3.0	METHODS	41
3.1	Study Area	41
3.2	Field Sites	43
3.3	Single-polarized RADARSAT-2 Imagery Acquisition and Processing	47
3.3.1	Speckle Filtering	50
3.4	Determination of an Optimal Image Data Set for Discrimination of Vegetation Types	51
3.4.1	Separability Analysis	51
3.4.2	Texture Analysis for Single-Polarized Radar Imagery	52
3.4.3	Separability Measures	55
3.4.4	Modelling and Mapping <i>P. australis</i> Distribution	59
3.5	Fully Polarized RADARSAT-2 Imagery Acquisition and Processing	59
3.5.1	Vegetation Class Discrimination Using Co-polarized and Cross-Polarized Scatter Plots	60
3.5.2	Polarimetric Plots	62
3.5.3	Vegetation Class Discrimination Using Polarimetric Decomposition	62
3.5.4	Decomposition Methods	63
3.6	Separability Analysis of Polarimetric Decompositions	64
3.6.2	Modelling and Mapping <i>P. australis</i> Distribution	68
4.0	RESULTS	69
4.1	Single-Polarized Results	69
4.1.1	Separability Analysis Based on Radar Texture and Brightness	69
4.1.2	Improving Separability through Image Channel Reduction	72
4.1.3	Overall Separability of <i>P. australis</i> vs. Other Samples	73
4.1.4	Examination of Physical and Textural Characteristics of <i>P. australis</i>	75
4.1.5	Modelling and Mapping <i>P. australis</i> Distribution	78
4.1.6	Accuracy Assessment of the Output Map	80
4.2	Quad-Polarized Results	82
4.2.1	Vegetation Class Discrimination Using Co-polarized and Cross-Polarized Scatter Plots	82
4.2.2	Polarimetric Plots & Pedestal Height	86
4.2.3	Vegetation Class Discrimination Using Polarimetric Decomposition	94

4.3	Separability Analysis of Polarimetric Decompositions	114
4.3.1	Improving Separability through Image Reduction	115
4.3.2	Separability of <i>P. australis</i> vs. Other Samples	116
4.3.3	Combining Decomposition Parameters	116
4.3.4	Examination of Physical and Textural Characteristics of <i>P. australis</i>	118
4.3.5	Modelling and Mapping <i>P. australis</i> Distribution	120
4.3.6	Accuracy Assessment of the Output Map	123
5.0	DISCUSSION AND CONCLUSIONS	124
5.1	Single-Polarized Imagery: Significant Findings	124
5.2	Single-Polarized Imagery: Research Limitations and Recommendations	126
5.3	Quad-Polarized Imagery: Significant Findings	127
5.4	Quad Polarized Imagery: Research Limitations and Recommendations	131
5.5	Conclusions	132
	REFERENCES	134
	APPENDIX 1	142

LIST OF TABLES

Table 1: Suitable wavelengths and polarizations for wetland mapping with SAR imagery as a function of wetland types.....	25
Table 2: Polarization, incidence angle and date of acquisition for all single-polarized RADARSAT-2 imagery.....	48
Table 3: Average root mean square for all single-polarized imagery.	50
Table 4: Image combinations for the separability analysis discriminating season and brightness/texture.	56
Table 5: Polarization, incidence angle and date of acquisition for all fully polarized RADARSAT-2 imagery.....	60
Table 6: Image combinations for polarimetric/decomposition separability analysis.	65
Table 7: Average BD separability results for the 3 image combinations.	69
Table 8: Subset of BD average separability results for 4/10 samples from spring texture image composition for <i>P. australis</i> and Other classes.....	71
Table 9: Subset BD average separability results for 4/10 from spring brightness/texture image composition for <i>P. australis</i> and Other classes.....	71
Table 10: Average BD separability results for 6 new image combinations (constrained for incidence angle) from the original spring texture average separability analysis.	73
Table 11: Average BD separability results for 2 new image combinations (constrained for polarization) from the original spring texture average separability analysis.	73
Table 12: Overall separability of <i>P. australis</i> and Other classes for 3 image combinations.	74
Table 13: Top 3 overall separability values for <i>P. australis</i> and Other classes for image combinations derived from a permutative channel reduction analysis of the spring texture imagery.....	74
Table 14: Physical and radar backscatter (0-255) characteristics of the 3 most separable <i>P. australis</i> samples derived from the single-polarized radar texture imagery.	77
Table 15: Physical and radar backscatter (0-255) characteristics of the 3 least separable samples derived from the single-polarized radar texture imagery.	77
Table 16: Average, 1 standard deviation, and 2 standard deviation statistics for the brightness values (0-255) derived from the radar texture imagery.....	76
Table 17: Average and standard deviation intensity values (dB) for the 3 vegetation classes and Water class for all of the polarimetric imagery.	85
Table 18: Raw pedestal heights for the 3 vegetation classes and Water class for the spring and summer seasons at shallow, medium and steep incidence angles.	87

Table 19: Dominant Van Zyl classes, based on 750 pixel samples, for each of the 3 vegetation classes and Water class for all 6 polarimetric images. The total percent that the dominant class makes up of the 750 total samples is included.	95
Table 20: Average scattering composition for the 3 vegetation classes and Water for each of the 6 polarimetric images derived from the Freeman-Durden decomposition. .	97
Table 21: Cloude-Pottier parameters based on 750 pixel samples for each of the 3 vegetation classes and Water class for all 6 polarimetric images. The numbers represent the mean values for each sample.	102
Table 22: Touzi parameters based on 750 pixel samples for each of the 3 vegetation classes and Water class for all 6 polarimetric images. The numbers represent the mean values for the total sample.	107
Table 23: Average BD separability results for the 3 image combinations.	114
Table 24: Average BD separability results for single decomposed spring imagery at varying incidence angles.	115
Table 25: Overall separability of <i>P. australis</i> and Other classes for single images, representing varying incidence angles, with decompositions applied.....	116
Table 26: Top 3 results from the permutative channel separability analysis derived from the steep incidence angle spring imagery.	117
Table 27: Physical and average Touzi decomposition parameters for the 3 most separable samples derived from the quad-polarized radar imagery.	119
Table 28: Physical and average Touzi decomposition parameters for the 3 least separable samples derived from the quad-polarized radar imagery.	119
Table 29: Average, 1 standard deviation, and 2 standard deviation statistics for the Touzi parameters derived from the steep, quad-polarized radar imagery.	120

LIST OF FIGURES

Figure 1: Spring (left) and summer (right) conditions of <i>P. australis</i> in Big Creek marshland. <i>P. australis</i> stands erect throughout the year, but loses its leaves in the fall resulting in less dense vegetation structures throughout the late fall to early spring time periods.	9
Figure 2: <i>P. australis</i> patch in the distance in the summer season. The patch is noticeably taller than the surrounding graminoid vegetation.	10
Figure 3: <i>P. australis</i> litter in the summer field season where no surface water was present.	11
Figure 4: <i>P. australis</i> shoot.	12
Figure 5: <i>P. australis</i> patch with low percent cover and surface water located in the Big Creek NWA study area.	13
Figure 6: The three major radar scattering types.	18
Figure 7: RADARSAT-2 C-band ultra-fine image acquired over Vancouver, Canada on January 6, 2008. The smaller images on the right-hand side are enlarged portions of the full image displayed on the left (Canadian Space Agency, 2008).	19
Figure 8: Horizontal and vertical polarizations of an electromagnetic wave along a vector over time.	23
Figure 9: Drawing of the electric vector E of a fully polarized wave in the x-y plane. The tip of the electric vector traces an ellipse, with a semi-major axis "a" and a semi-minor axis "b". The ellipticity (X) and orientation (Ψ) angles are defined as shown (CCRS, 2010).	32
Figure 10: Co-polarized and cross-polarized signature plots displaying the orientation, ellipticity, polarization, and pedestal height parameters. The pedestal height in this plot is very close to zero.	33
Figure 11: Long Point on Lake Erie. Big Creek NWA is found to the west, while Long Point NWA is further east (Environment Canada, 2009).	42
Figure 12: Oblique aerial Image of Long Point. The width of the point is approximately 200m across at the lighthouse (Environment Canada, 2009).	43
Figure 13: Spring 2006 aerial photo mosaic over the Big Creek National Wildlife Area showing the locations of all <i>P. australis</i> field transects (red) and several <i>P. australis</i> locations interpreted from the aerial imagery. The bottom left image displays a close-up view of some visible <i>P. australis</i> patches and sample transects. A single-polarized HH radar image is included for context. Big Creek NWA is highlighted in bright green (two sections); while Long Point NWA is highlighted in light blue.	45
Figure 14: Line intercept method for transecting <i>P. australis</i> patches.	46

Figure 15: *P. australis* patch (centre) under 3 filtering conditions; (a) unfiltered, (b) enhanced Lee, (c) standard Lee in a steep incidence angle HH, spring image. 51

Figure 16: Top - poor quality (shallow VV summer) and bottom - better quality (steep HH spring) Mean texture images derived from the single-polarized radar dataset. A combination of better quality texture images allows for a good characterization of the study area. 53

Figure 17: Sample window locations. The green arrows indicate the location of a *P. australis* sample used in the initial separability analysis from the Big Creek study area. 54

Figure 18: Sample window locations. The green arrows indicate the location of a *P. australis* sample used in the initial separability analysis from the Long Point study area. 66

Figure 19: Model derived from the separability analysis and further investigation of the radar texture values. The model outputs a classification showing areas of water (based on surface scattering) and land (based on volume scattering). Further criteria are implemented in order to classify patches of *P. australis*. 78

Figure 20: Classification map showing correctly identified (orange) and missed (black) patches of *P. australis* derived from the model. 80

Figure 21: Scatter plots displaying the co-polarized (HH/VV) and cross-polarized (HH/HV) intensity ratios for the spring and summer quad-pol imagery at shallow incidence angles. 83

Figure 22: Scatter plots displaying the co-polarized (HH/VV) and cross-polarized (HH/HV) intensity ratios for the spring and summer quad-pol imagery at medium incidence angles. 84

Figure 23: Scatter plots displaying the co-polarized (HH/VV) and cross-polarized (HH/HV) intensity ratios for the spring and summer quad-pol imagery at steep incidence angles. 84

Figure 24: Co-polarized and cross-polarized polarimetric plots showing the *P. australis* class during the spring and summer seasons at shallow, medium and steep incidence angles. 89

Figure 25: Co-polarized and cross-polarized polarimetric plots showing the Cattail class during the spring and summer seasons at shallow, medium and steep incidence angles. 90

Figure 26: Co-polarized and cross-polarized polarimetric plots showing the Grass class during the spring and summer seasons at shallow, medium and steep incidence angles. 92

Figure 27: Co-polarized and cross-polarized polarimetric plots showing the Water class during the spring and summer seasons at shallow, medium and steep incidence angles. 93

Figure 28: Spring season Van Zyl decomposition maps for the Long Point and Big Creek study areas. Top to bottom: steep, medium, shallow incidence angles, respectively. 'A' shows increased wave interaction and multiple scattering. 96

Figure 29: Spring season Freeman-Durden decomposition maps for the Long Point and Big Creek study areas. Top to bottom: steep, medium, shallow incidence angles, respectively. 'A' displays an increase in surface scattering. Red represents double-bounce scattering, green represents volume scattering, and blue represents surface scattering. 100

Figure 30: Spring season Cloude-Pottier decomposition maps representing Entropy (H) for the Long Point and Big Creek study areas. Top to bottom: steep, medium, shallow incidence angles, respectively. 103

Figure 31: Spring season Cloude-Pottier decomposition maps representing Alpha (α) angles for the Long Point and Big Creek study areas. Top to bottom: steep, medium, shallow incidence angles, respectively. 105

Figure 32: Spring season Touzi decomposition images representing the Alpha_S parameter for the Long Point and Big Creek study areas. Top to bottom: steep, medium, shallow incidence angles, respectively. A decrease in incidence angle increases homogeneity of the Alpha_S parameter over vegetation..... 108

Figure 33: Spring season Touzi decomposition maps representing the Touzi_Phase parameter for the Long Point and Big Creek study areas. Top down: steep, medium, shallow incidence angles. A steep incidence angle displays more heterogeneity over the study area. 110

Figure 34: Spring season Touzi decomposition parameters at 3 incidence angles..... 112

Figure 35: Summer season Touzi decomposition parameters at 3 incidence angles. ... 113

Figure 36: Model derived from the separability analysis and further investigation of the Touzi parameters applied to the steep incidence angle, quad-polarized image. The model outputs a classification showing areas of water (based on surface scattering) and land (based on volume scattering). Further criteria is implemented in order to classify patches of *P. australis*. 121

Figure 37: Classification map showing large patches of *P. australis* (red) identified by the model as well as areas classified as water (blue) and Other (green). 122

1.0 INTRODUCTION

Over the past century the ecological integrity of Canadian wetlands has been severely compromised by a host of negative influences including drainage, degradation, anthropogenic expansion, and the introduction of exotic species (Wilcox, 2003; Pertrie and Francis, 2003; Crowder and Bristow, 1998; Herdendorf, 1992; Smith et al., 1991). As these factors increase in frequency and magnitude, concerns over wetland loss and devastation are being brought to the forefront of public and private attention. Scientists, resource managers, and the general public have proposed that measures be implemented to control these issues, especially in Great Lakes wetlands (Wilcox, 2003). Of primary concern is the management of invasive species (Buckley, 2008). Once introduced, invasive species invade a site quickly and can take over a wetland community by crowding out native plants, changing marsh hydrology, altering wildlife habitat, and increasing fire potential (Lavoie, 2008).

Wetlands are a vital ecological component and core element in resource management programs, and therefore the detection and monitoring of these areas has assumed increasing importance in light of their benefits and the constant pressures they sustain from invasion (Henderson and Lewis, 2008). Wetlands can be broadly defined as land that is saturated with water long enough to promote wetland or aquatic processes as indicated by poorly drained soils, hydrophytic vegetation and the various kinds of biological activity which are adapted to a wet environment (National Wetlands Working

Group, 1997); wetlands include bogs, fens, marshes, swamps and shallow waters up to 2m in depth (National Wetlands Working Group, 1997). The classification and monitoring of wetlands, and more specifically wetland types based on an assessment of constituent land cover, is difficult due to fluxes in landscape structure over varying timescales. Henderson and Lewis (2008) state that the “magnitude of wetland detection and monitoring coupled with the dynamic nature and inaccessibility of wetland ecosystems has limited the use of on ground efforts and encouraged the use of various remote sensing platforms, given their ability to record large areas in comparatively short periods”.

Novitzki et al. (1996) states that wetlands help to control flooding, ameliorate droughts, provide habitat for a myriad of flora and fauna, maintain and improve water quality, provide storage for water, stabilize water supply, mitigate erosion, reduce [storm]-related damage and offer recreational possibilities. More specifically, wetlands are the primary source of renewable drinking water for an estimated 1.5-3 billion people and they provide approximately US\$34 billion to the gross world product every year through wetland-related fisheries and agriculture, such as mangrove forests (Millennium Ecosystem Assessment, 2005). Globally, wetlands, as methane generators and carbon sinks, are recognized as important contributors to weather and climate modification (Henderson and Lewis, 2008). Wetland preservation is of primary concern to numerous physical science researchers, many of whom have focused on the specific benefits of natural wetland areas (Daily et al., 1997; Horowitz et al., 2001; Woodward

and Wui, 2001; Manual, 2003, Meindl, 2004; Verhoeven et al., 2006; Grenier et al., 2007).

Research into wetland loss has presented the extensive, continuing damage that wetlands are suffering globally. According to the Millennium Ecosystem Assessment (2005), over 60% of European and North American marshes have been lost or degraded by clearing and draining for agricultural use. Canada alone holds over 24% of the world's wetlands and within it losses range from 65% to 80% of pre-settlement area (National Wetlands Working Group, 1988). The Great Lakes wetlands are of primary concern as, for example, less than 5% of western Lake Erie's original wetlands remain (Wilcox, 2003; Herdendorf, 1987).

Invaded landscapes and ecosystems are composed of multiple interacting networks and feed-back loops, sometimes leading to unexpected effects of management actions (Buckley, 2008). In order to plan measures of control for invaded ecosystems it is necessary to explicitly consider management goals before taking action. Any actions taken should be justified in terms of their effective impacts on invaders, amelioration of native species (both flora and fauna), contribution to the management goals and the costs incurred (Buckley, 2008).

Recent invasion of *Phragmites australis* (hereafter referred to as *P. australis*) is rapidly overtaking native flora in the wetlands of the Great Lakes. While *P. australis* is native to Europe, Africa and North America, invasive haplotypes, originating from Europe, are now widespread throughout North America (Arzandeh, 2003; Wilcox, 2003;

Saltonstall, 2002). *P. australis* primarily grows in marshes and swamps and along streams, lakes, ditches, and wet wastelands (Arzandeh, 2003; Duke, 1983) and grows well on both organic and mineral substrates, forming dense homogenous monocultures (Wilcox, 2003). *P. australis* prospers with the periodic flooding and drying along the shores of Lake Erie and is very difficult to eradicate, as the rhizomes may reach 10 m or more in length (Duke, 1983).

Loss of native flora species, such as cattail and various graminoids, to *P. australis* is threatening the habitat of migratory waterfowl and other species that rely on wetlands for habitat because it displaces the native species which the birds rely upon for nesting. It is therefore important to monitor the general vegetation change in Great Lakes wetlands in order to implement management strategies for invasive species before the delicate ecosystem is overrun. In order to reach the common goal of re-establishing and restoring native wetland plant communities in the Great Lakes region, controlling *P. australis* is a necessary step. Implementing selective control, as needed, will not only keep *P. australis* from re-establishing dominance, but will also allow for the recovery of native species of wetland vegetation (Tu et al., 2001).

Monitoring and adaptive management are integral components of a successful invasive species control plan. A detailed monitoring plan should be developed prior to implementation of control measures. Detection of *P. australis* monocultures provides the data needed to determine the effectiveness of initial control efforts and the types of follow-up control methods that are necessary (Tu et al., 2001).

Remotely sensed data are an important means for locating invasive species and identifying and analyzing land cover change (Arzandeh, 2003). The repetitive acquisition of satellite imagery provides the possibility to observe the seasonal and other temporal changes in the environment.

Traditionally, the mapping of vegetation, including wetlands, has been conducted with optical data, but the primary limitation of optical sensors for wetland mapping is their inability to actively penetrate surface materials, and thus their inability to remotely sense water levels and surface structure beneath herbaceous wetland vegetation which may lead to a better characterization of specific vegetation classes (Bourgeau-Chavez, 2001). Ancillary data such as topography and soils as well as intensive field surveys are often necessary when using optical data for wetland mapping. Since the early 1980s, L-band (23 cm wavelength) synthetic aperture radar (SAR) systems have been used in order to penetrate vegetation canopies and receive enhanced backscatter from forested and emergent wetlands (Bourgeau-Chavez, 2001; Ormsby et al., 1985; Richards et al., 1987). More recently, several studies have shown C-band (5.7 cm wavelength), single-polarized SAR data from the European ERS satellite can be useful for detecting and monitoring herbaceous and sparsely forested wetlands in North America (Bourgeau-Chavez, 2001; Tanis et al., 1994, Bourgeau-Chavez et al., 1996, Kasischke and Bourgeau-Chavez, 1997). Other studies have been conducted to determine the utility of polarimetric data, including NASA's Shuttle Imaging Radar-C (SIR-C) and AirSAR for wetland classification in tropical wetlands (Pope et al., 1994, 1997; Hess et al., 1995). These studies have demonstrated the utility of multi-band data and polarimetric

analyses (HH-VV phase difference) for mapping wetland vegetation and add value to the idea that radar can be used to detect invasive flora, especially if the vegetation being mapped can be discriminated based on unique structural characteristics or locally-unique water levels.

This thesis is a collaborative effort between the National Wildlife Research Centre, as part of their commitment to preserving Canada's natural wildlife habitat, and the Geomatics and Landscape Ecology Laboratory at Carleton University. The overall goal of this research was to determine if radar imagery could be used to detect *P. australis*, and if so, to determine the best type of imagery and under what field conditions detection was most feasible.

1.1 Objectives

1. Determine the optimal polarization, incidence angle and time of year for detecting small (< 150 m diameter) monocultures of *P. australis* using RADARSAT-2 single-polarized Ultrafine (3 m) imagery.
2. Establish the best image processing and decomposition methods for detecting large (> 150 m diameter) monocultures of *P. australis* using RADARSAT-2 fully polarimetric (8 m) imagery.
3. Based on the first two objectives, create classifications showing the extent and spatial distribution of *P. australis*.
4. Based on the success of the third objective, evaluate the accuracy of the classifications for detecting *P. australis*.

1.2 Thesis Structure and Datasets

This thesis makes use of two datasets (imagery) on which analyses are performed. The first set of data is single-polarized RADARSAT-2 imagery (3m spatial resolution), while the second data set is quad-polarized RADARSAT-2 imagery (8m spatial resolution). Both single-polarized and fully polarimetric imagery were utilized concurrently in this study in order to narrow down the limiting factors encountered when using each type of data. While single-polarized imagery is of a higher resolution, it lacks the phase and complex polarization information of the fully polarimetric data. The single-polarized imagery was used to detect small, generally circular, patches of *P. australis* in one section of the study area (Big Creek National Wildlife Area), while the quad-polarized imagery was used to detect much larger patches of *P. australis* in another section of the study area (Long Point). These areas are highlighted in the methods section of the paper (Chapter 3).

The Background section (Chapter 2) of this paper provides details related to the invasive species *P. australis*, National Wildlife Areas and their importance, radar remote sensing in general, previous research related to the remote sensing of wetlands, and complex polarimetric radar analysis (decomposition). Chapter 3 (Methods) outlines the study area and field sites, single-polarized radar imagery acquisition and processing, and quad-polarized imagery acquisition and processing. The Results section (Chapter 4) provides details on the results of both the single-polarized and fully polarized analyses,

while Chapter 5 (Discussion) talks about the significant findings and limitations derived from the research.

2.0 Background

2.1 Invasive Common Reed (*Phragmites australis*)

The Common Reed (*Phragmites australis*) is a perennial, emergent aquatic plant that can grow up to 6 m in height with a stem diameter of between 4 to 10 mm. The leaves of *P. australis* are smooth, 20 to 70 cm long and 1 to 5 cm broad, and taper to long slender points. The inflorescence, a cluster of flowers arranged at the top of the stem, grows to approximately 30 cm in length, is dull purple or yellow and bears many spikelets. There exists an indigenous variety (North American) of the common reed and a more invasive European variety. Fossil records indicate that the indigenous genotype has existed in North America for over 40,000 years (Hansen, 1978) while the invasive genotype was introduced within the last 200 years (Rice et al., 2000; Saltonstall, 2002). The native variety is much less aggressive than its alien counterpart (Mal and Narine, 2003). Figure 1 displays spring and summer season conditions of *P. australis*.



Figure 1: Spring (left) and summer (right) conditions of *P. australis* in Big Creek marshland. *P. australis* stands erect throughout the year, but loses its leaves in the fall resulting in less dense vegetation structures throughout the late fall to early spring time periods.

A single plant of the invasive variety spreads horizontally at a rate of 1 to 2 m per year and, once established, can form patches from $<1 \text{ m}^2$ to hundreds of m^2 (Mal and Narine, 2003). *P. australis* most commonly grows in low-lying wet areas such as fresh and salt-water marshes, shallow lake edges and drainage ditches. In North America, *P. australis* often forms extensive monocultures through the displacement of native vegetation types such as cattail, marsh meadow, and sedge/grass hummock (Wilcox et al. 2003). Displacement is most severe in the lower Great Lakes region and is primarily encouraged through rivers, canals, waterways, and increasingly, roads. Figure 2 displays a patch of *P. australis* in the summer.



Figure 2: *P. australis* patch in the distance in the summer season. The patch is noticeably taller than the surrounding graminoid vegetation.

P. australis colonizes a new area through the clonal dispersal of perennial rhizome fragments and, less commonly, by seeds which can be carried by water, animals and machinery (Marks et al., 1994). Rhizomes are the horizontal stems of a plant that are usually found beneath the soil surface. As they send out roots and shoots from their nodes, once the plant is established, new upright stems develop from the rhizomes. Along the north shore of the Great Lakes, *P. australis* begins to flower in late June and forms seeds by early August. In the fall, the leaves of the plant die and fall off; leaving behind only the dead vertical shoots and flower remnants. The build up of dead plant material, along with the pervasive rhizome system, prevents the growth of native plant species. The dead shoots remain standing for 3 to 4 years before falling to the level of the leaf litter. Figure 3 displays *P. australis* leaf litter in the summer season.



Figure 3: *P. australis* litter in the summer field season where no surface water was present.

P. australis abundance has been shown to increase with lower lake levels where soil remains at or near saturation and is reduced with higher water levels (Wilcox et al., 2003). In addition, higher air temperatures have been linked to an increase in abundance. This finding is of particular concern because temperatures have been on an upward trend in southern Ontario, while lake levels have been lowering, over the past several decades (Wilcox et al., 2003). Figure 4 displays a *P. australis* shoot found in a formerly saturated shoreline area. Figure 5 displays an overhead view of a patch of *P. australis* showing a 1 m² sampling frame.



Figure 4: *P. australis* shoot.

The most common *P. australis* control method is the use of herbicide, however it has not yet been approved in Canada, so cutting, burning, and complete drainage of the species' habitat have been used (Mal and Narine, 2003). Once established, *P. australis* is difficult to completely eradicate, although careful planning and long-term management has produced satisfactory results.



Figure 5: *P. australis* patch with low percent cover and surface water located in the Big Creek NWA study area.

2.1.1 Detrimental Effects of *P. australis*

Within North America, *P. australis* not only displaces its own native genotypes but it also out-competes other native species (Saltonstall, 2002). The available habitat for feeding and breeding by waterfowl and other waterbirds is generally reduced by the presence of *P. australis*, which results in an overall loss of bird-species richness and diversity (Chambers et al., 1999). In dense stands, the possibility of marsh fires is increased due to the accumulation of dry litter (Marks et al., 1994). *P. australis* often causes a financial burden to countries and communities due to its rapid and expansive

growth in public lakes and waterways which must be repeatedly cleared (Mal and Narine, 2003). Many wetlands which are dominated by *P. australis* suffer because of increased drainage and peat oxidation (Chambers et al., 1999), and alterations to soil properties such as salinity and microtopographic relief (Windham and Lathrop, 1999). Under some conditions, such as in drier areas, the unimpeded growth of *P. australis* leads to anaerobic conditions in which the development of secondary consumer populations which break down organic matter is prevented (Schleyer and Roberts, 1987). Lastly, bacteria found in the decomposing litter of *P. australis* has been found to produce excessive amounts of methane gas, which is a potent greenhouse gas and is linked to a recent increase in global temperatures (Chanton et al., 1993).

2.1.2 Benefits of *P. australis*

Despite the detrimental effects related to *P. australis* infestation in North America, some researchers have pointed to the benefits of the species, especially in Europe where it is considered non-invasive. The stems of *P. australis* are used for manufacturing cardboard, hardboard, paper, and packing materials (Hocking et al., 1983). Leaves of young shoots contain 18% crude protein and can be used for grazing by livestock. Because of the intricate nature of roots and rhizomes, reed beds can be used to protect banks of lakes, canals and rivers from erosion (Coops et al., 1996). The roots of *P. australis* are capable of biological detoxification through the absorption of heavy metals and other environmental pollutants such as DDT residues (Cooper et al., 1990; Dunbabin and Bowmer, 1992; Gassner and Neugubohrn, 1994). Despite these

advantages, within North America the detrimental issues associated with *P. australis* outweigh any of the currently utilized beneficial characteristics.

2.2 National Wildlife Areas

The Canadian government establishes and protects National Wildlife Areas (NWAs) in accordance with the Canadian Wildlife Act under the management of the Canadian Wildlife Service (CWS) of Environment Canada. NWAs provide protection from disturbance for natural features deemed to be essential to individual sites. Management activities include “monitoring wildlife, maintaining and improving wildlife habitat, conducting periodic inspections, enforcing regulations, maintaining facilities, and developing management plans” (Environment Canada, 2010). As well as conservation, wildlife research and interpretation are integral to the understanding of wildlife processes within NWAs.

A key component of the Canadian Wildlife Act is preserving natural habitats that are critical to migratory birds and other wildlife species, and in accordance with Section 3 (d) of the Canadian Wildlife Act, “no person shall, in any wildlife area, damage, destroy or remove a plant, unless he does so under and in accordance with a permit issued by the Minister” (Canadian Wildlife Act, 2009). Species considered to be detrimental to the overall health of the NWA may be controlled or removed by CWS or an outside party given written permission.

Many NWAs are wetland ecosystems which have been deemed internationally important as outlined in the RAMSAR Convention. The Convention on Wetlands

(Ramsar, Iran, 1971) is an intergovernmental treaty that aims to maintain the ecological integrity of wetland environments by preventing the loss and degradation of habitat. In addition to the marshlands commonly found in southern Canada, the RAMSAR Convention seeks to protect all types of wetlands, including “lakes and rivers, swamps, wet grasslands and peatlands, oases, estuaries, deltas and tidal flats, near-shore marine areas, mangroves and coral reefs, and human-made sites such as fish ponds, rice paddies, reservoirs, and salt pans” (Ramsar, 2010). A key component of the RAMSAR Convention is international cooperation, especially concerning transboundary wetlands, shared wetland systems and shared species.

2.3 Single-Polarized and Fully Polarimetric Radar Remote Sensing

Radar systems developed for the purpose of earth imaging are unique among the various types of remote sensing platforms in their ability to provide information regarding signal-target interactions (Lillesand and Keifer, 2004). Passive optical and short-wave infrared sensors capture the energy reflected/emitted from an object due to illumination from an outside source, usually the sun. In contrast, radar systems actively transmit a wave of energy in the microwave portion of the electromagnetic spectrum. This energy bounces off of a target on the ground and is scattered in various directions depending on the geometry and other physical properties of the object. The energy that reflects back in the direction of the radar antenna is called backscatter.

The radar backscatter is used to create the radar intensity image, and in a conventional visualization of the data, the more energy that reflects off of a target and

back towards the sensor, the brighter the target will appear in the image. This brightness information can be used to determine target characteristics on the ground. For example, in radar images water often appears dark because the incident energy reflects off of the smooth surface of the water and away from the sensor. This is known as specular scattering.

In comparison, ships, buildings and tall vegetation often have greater backscatter returns due to the vertical orientation of the structures, which results in the wave being reflected off of the ground, against the structure, and then back towards the sensor. This type of scattering is known as double-bounce scattering or corner reflection.

A third common type of reflection is known as diffuse scattering. Diffuse scattering occurs when an object directs energy in many directions. A common form of diffuse scattering is known as volume scattering, which occurs when the target is composed of a porous material, such as a vegetation canopy, and the incident wave is reflected in multiple directions due to the complicated geometry of the target. Figure 6 displays an example of the three main scattering types.

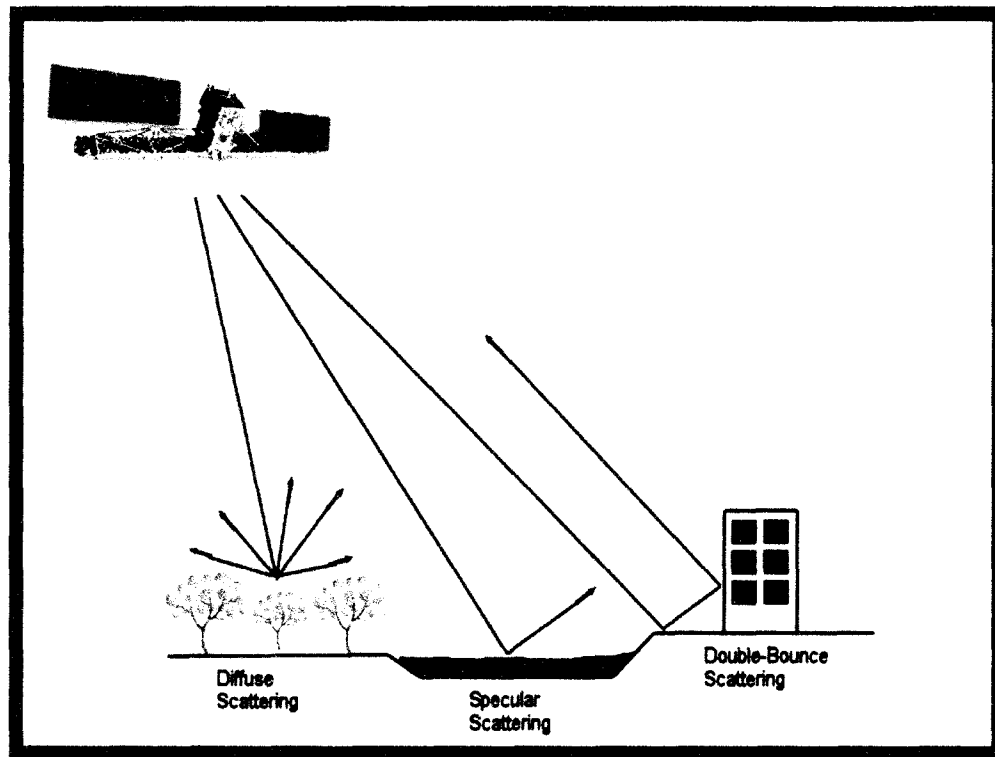


Figure 6: The three major radar scattering types.

Figure 7 is an example of a RADARSAT-2 C-band polarimetric radar image acquired over Vancouver in January, 2008. The water in the image is noticeably darker than the ships which are enlarged in the top right-hand portion of the image. Urban areas along the coast also appear bright due to double-bounce scattering.

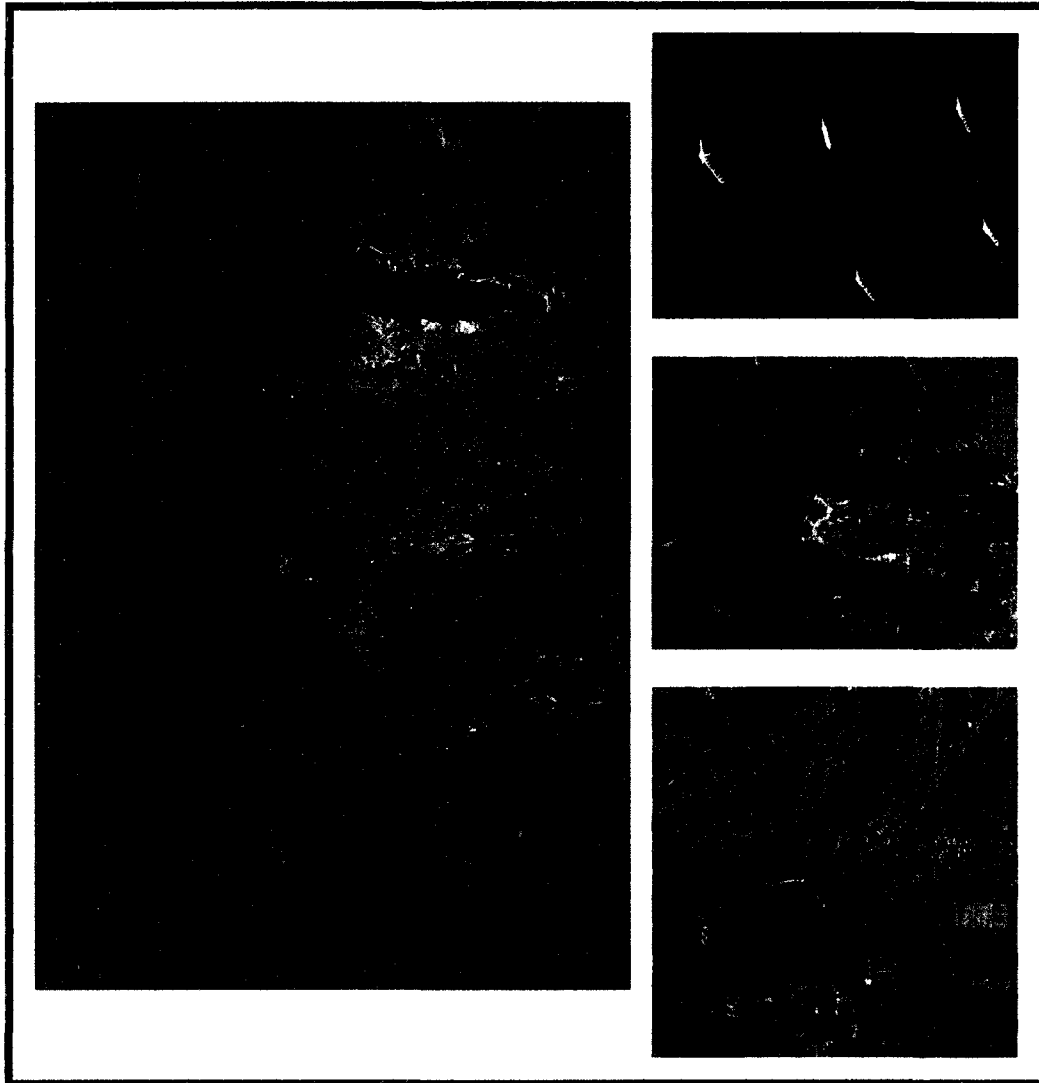


Figure 7: RADARSAT-2 C-band ultra-fine image acquired over Vancouver, Canada on January 6, 2008. The smaller images on the right-hand side are enlarged portions of the full image displayed on the left (RADARSAT-2 ©MacDONALD, DETTWILER AND ASSOCIATES LTD., 2008 – All Rights Reserved).

The scattering at a given pixel is affected by the dielectric constant of the surface material, which is an electrical property of matter that influences radar returns (CCRS, 2009). It is a fundamental (complex) parameter that describes the electrical properties

of a lossy medium (a medium that absorbs some electromagnetic radiation). By convention, the relative dielectric constant of a given material is used, defined as the absolute dielectric constant divided by the dielectric constant of "free space". For radar remote sensing applications of biological systems, the dielectric constant of vegetation is affected by water content. Vegetation with high water content or water on the surface of the vegetation has a higher dielectric constant than dry vegetation. As a result, water can cause a target to reflect a stronger signal. It is therefore desirable to acquire radar imagery of vegetation under drier conditions with no surface water present (e.g. from recent rainfall) on the vegetation.

Backscatter is most often expressed in decibels (dB). The most common way of describing backscatter for environmental applications is in ground range sigma nought (σ^0) format, which is a dimensionless number, giving the mean backscatter from an area of one square metre on the surface of the Earth (CCRS, 2010). Sigma nought is dependent on the properties of the scatterer and usually varies significantly with incidence angle, radar wavelength, and polarization.

Inherent in SAR images is a component known as speckle. Speckle refers to a noise-like characteristic produced by coherent systems and manifests as a random structure of image elements caused by the interference of electromagnetic waves scattered from targets (Lillesand and Keifer, 2004). Conventional image processing and analysis tasks often treat speckle as an undesirable feature. When transforming SAR signal data into actual imagery, 'multi-look' processing is usually applied in order to

reduce speckle (CCRS, 2008). Multi-looking refers to the averaging of independent images in order to create a single multi-look image; however, this does result in a loss of spatial resolution (Lillesand and Keifer, 2004). The speckle still inherent in the actual SAR image data can be reduced further through processing tasks such as filtering and smoothing, which tend to reduce statistical variance in conventional image classification schemes. Unlike system noise, speckle is a real electromagnetic measurement and can be exploited for use in SAR interferometry (CCRS, 2008).

Speckle filters are a radiometric enhancement technique that reduce speckle while minimizing the loss of information in a SAR image (Lillesand and Keifer, 2004). For most applications, they remove high frequency noise while preserving high frequency features such as edges. They are applied in a moving window that processes the centre pixel of the window based on the noise and edge properties of all the pixels within the window. Choosing the correct window size can be a complex process; if the filter is too large, subtle details of the image can be lost; if the filter is too small, the process will not be effective as it does not remove a sufficient amount of speckle. For wetland and other heterogeneous area applications where edge features are non-linear, in contrast to an urban setting for example, it is important to reduce speckle while preserving radiometric information and spatial signal variability (e.g. texture).

By filtering a radar image, better discrimination of image targets and easier automatic segmentation, through the use of software algorithms, can be achieved. In

addition to this, after an image has been filtered, other enhancement techniques, such as decomposition, can be applied with improved results.

Polarization is a property of an electromagnetic wave that describes the locus of the electric field vector as a function of time. In its raw format, the signal received by a polarimetric radar sensor for a given pixel is commonly described using the complex scattering matrix S in Eq.1, which is a representation of the received power at each of the four polarizations (HH, HV, VH, VV):

$$S = \begin{bmatrix} S_{HH} & S_{HV} \\ S_{VH} & S_{VV} \end{bmatrix} \quad [1]$$

A polarimetric radar records the intensity of scattering in four mutually coherent channels (typically HH, VV, HV and VH), but also retains the phase information associated with these polarizations during processing. In the special case of linearly polarized waves where the orientation of the electric field vector on transmission or reception is horizontal (H) or vertical (V), the polarization of a radar image can be HH (horizontal transmit, horizontal receive), VV (vertical transmit, vertical receive), HV (horizontal transmit, vertical receive), or VH (vertical transmit, horizontal receive). Radar images are labelled co-polarized when the transmitted and received polarizations are the same, and cross-polarized when the polarizations are orthogonal. Figure 8 displays a simple visualization of two forms of radar polarization; horizontal and vertical.

In polarimetric radar systems the orthogonal components (see Section 2.5) of the transmitted and received waves are preserved along with the phase information. Phase refers to the relative time it takes a wave to travel to a target and back to the sensor and is measured in rotational degrees (e.g. 0° - 360°) or radians (CCRS, 2008). Waves are considered in-phase if their origins of phase are perfectly aligned (e.g. 0°). Phase differences between polarizations can occur as a result of differential scattering of these polarizations from within the target. Precise knowledge of phase properties in radar signal data is a key element of polarimetric SAR.

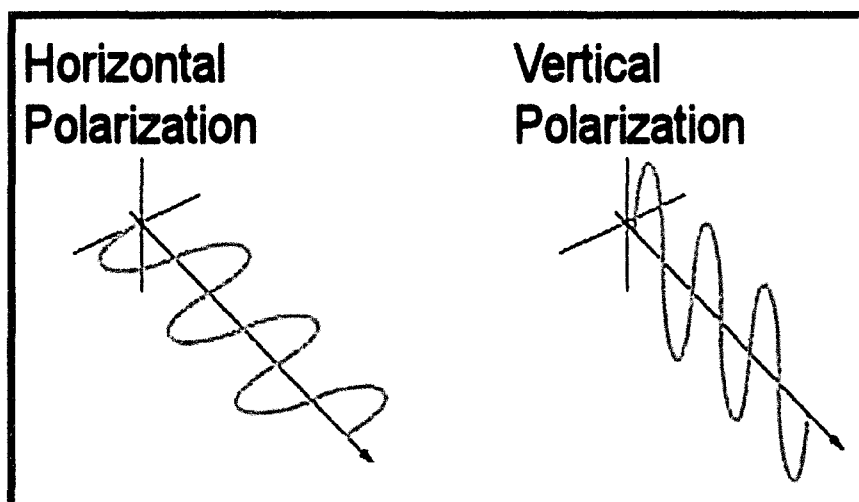


Figure 8: Horizontal and vertical polarizations of an electromagnetic wave along a vector over time.

The intensity of scattering from a target is dependent upon the target characteristics, primarily the geometric structure and dielectric properties of the target, as well as by the specific sensor configuration including the polarization of the incident wave, the angle of incidence and the frequency of the radar wave. The random

roughness of the target, as well as the orientation of dominant structures of the target, will also affect the strength of the radar response. For targets with significant vertical structure, incident waves tend to couple with this target structure. Depending on the SAR wavelength relative to the size of the target structure, this can result in greater attenuation or scattering of the incident vertically polarized wave, relative to horizontally polarized waves. Horizontally oriented waves couple less with this vertical structure and tend to penetrate the target to a greater extent and interact more with the underlying surface.

The wavelength of the energy allows microwaves to be classified into different bands. For example, an L-band microwave is longer than a C-band microwave. This is useful because longer wavelengths are capable of more penetration into the vegetation canopy (Hendersen and Lewis, 2008), so, it is often possible to use the longer L-band to detect surface water characteristics of wetlands through the vegetation canopy (Ramsey, 1998). On the other hand, C-band radar data has been found to be useful for mapping herbaceous wetland vegetation (Kasischke et al., 1997, Pope et al., 1997, Ramsey, 1998), and much of the previous work in the area of wetland mapping has relied upon identifying wetland types based on the constituent vegetation. Table 1 shows the suitable wavelengths and polarizations for wetland mapping as a function of wetland types derived from previous SAR studies. P-band radar, as seen in Table 1, is even longer than L-band.

Table 1: Suitable wavelengths and polarizations for wetland mapping with SAR imagery as a function of wetland types.

Wetland Type	Band	Polarization	Authors
forests, dense vegetation	P, L	HH	Kasischke <i>et al.</i> 1997; Ramsey, 1998
bog and inundated vegetation	L	HH	Yamagata and Yasuoka, 1993
herbaceous and sparse vegetation	C		Kasischke <i>et al.</i> 1997
low density marshes	C	VV	Pope <i>et al.</i> 1997
high density marshes	C	HH, VV	Pope <i>et al.</i> 1997; Ramsey, 1998
non-woody and herbaceous	C	HH, VV	Kasischke and Bourgeau-Chavez, 1997

2.4 Radar Remote Sensing of Wetland Ecosystems

In order to efficiently make use of remote sensing technology, the desired information that is to be derived from targets on the ground should be known in advance. The remote sensing of wetlands primarily deals with distinguishing between vegetation types (Augusteijn and Warrender, 1998; Simard *et al.*, 2002; Sgrenzaroli *et al.*, 2004). Alternatively, a sensor can be used to measure other physical characteristics of an ecosystem, such as water levels or topography (Hess *et al.*, 1990; Ramsey, 1995; Wang *et al.*, 1995; Kasischke *et al.*, 2003; Walfir *et al.*, 2005). This form of monitoring is based on a deterministic framework. In terms of operational radar systems, there is a commonly known interaction between the incident microwave and the various surfaces with which it interacts. This interaction is quantified by researchers and used to create visualizations of the composition and configuration of the on-ground elements. Models that are developed through most radar remote sensing initiatives are analytical in the sense that there exist known empirical relations between the transmitted microwaves and objects with certain physical characteristics (Lillesand and Keifer, 2004).

When an ecosystem composed of new targets is to be imaged it is up to researchers to discover the deterministic interactions which will allow them to quantify the unique features within the image. Once such relations are known it is possible to apply the same methods to other areas. This is in keeping with a primary purpose of remote sensing: to accurately monitor large areas over short periods of time. By determining the cause and effect relations between the radar wave and the backscatter return it is possible to develop models of the environmental systems that are being imaged. Like models in physical science, those developed through remote sensing are formal representations of the essential elements of the system.

The evolution and ingenuity of research in terms of ability to distinguish more complex wetland types shows that as researcher experience and technology increases it is becoming more possible to accurately monitor the hydrological component of wetlands, mainly related to surface water and soil moisture detection. When remote sensing first began to be used for wetland monitoring it was only possible to distinguish between areas with or without surface water, but it has become increasingly possible to measure different levels and spatial distributions of surface water and soil saturation (Hendersen and Lewis, 2008).

2.4.1 Wetland Classification Based on Physical Characteristics

Various studies have examined the utility of remotely sensed data for the classification of wetlands based on the physical characteristics of vegetation and other features found within the wetland structures. Hess et al. (1990) reviewed a series of 34

articles focusing on wetland monitoring using synthetic aperture radar (SAR) and optical imagery and found accuracies up to 93% for flooded forest classification based on surface water detection. They did, however, find some sources of error and confusion relating to the ability to distinguish between flooded forests and flooded non-forests, such as marshes (Hess et al., 1990). These errors were directly related to the classification of wetland types and therefore strongly suggest that field analysis or supplementary data is necessary in cases where confidence in classification is low. In addition to this, it is important to note that continuous water cover provides a consistent and known surface roughness and dielectric constant which simplifies wave-vegetation interactions, thereby simplifying surface water detection (Hess et al., 1990). This idea suggests that more heterogeneous wetlands will be more difficult to classify both in definition and through physical/remote sensing techniques.

Pope et al. (1997) found that it was possible to separate dry or partially flooded marsh from flooded marsh using polarimetric C-band SAR. Ramsey (1995) used the same type of imagery to monitor seasonal water levels in Florida coastal wetlands. In a later review paper, Ramsey (1998) concluded that a temporal analysis of wetland water budgets was possible, especially in cases of flood detection as long as flooding was continuous over large areas. In the same review it was found that where vegetation type could not be ascertained, soil moisture measurement was crucial to wetland detection (Ramsey, 1998). Frappart et al. (2005) improved upon previous methods by using multi-date SAR imagery in order to accurately classify four wetland ecosystems: (1) occasionally flooded forest, (2) occasionally flooded low vegetation, (3) permanently

flooded forest, and (4) submerged vegetation. Using a combination of Landsat-5 and Radarsat-1 data, Walfir et al. (2005) were able to distinguish between seven wetland land cover classes that were strongly influenced by surface water presence: (1) Young intertidal mangrove, (2) intertidal mangrove, (3) supratidal mangrove, (4) outer salt marsh, (5) inner salt marsh, (6) degraded mangrove, and (7) regenerated mangrove. A common finding across studies that employed remote sensing was that multi-date imagery was superior to single-date imagery when classifying wetlands as varying water levels play a significant role in wetland classification (Kasischke et al., 2003; Frappart et al., 2005; Li and Chen, 2005; Racine et al., 2005).

Crevier et al. (1996) found that frost development leading up to the winter season was a suitable indicator for measuring moisture variations over saturated areas and could therefore be used to delineate wetlands based on soil and above-ground surface moisture within the Ottawa region. This finding also leads into an evaluation of the temporal aspects of monitoring wetlands. Since frost cannot be used as a hydrological indicator during the warmer months in the Ottawa area, it would be most suitable to visually detect wetlands around late-October/early-November. This finding provides a specific timeline for field analysis and imagery acquisition.

2.4.2 Radar Remote Sensing of Wetland Vegetation Types

The biological component of wetlands includes both the plant and animal species that are present. For the purpose of detecting and monitoring a dynamic physical environment, vegetation types are often the focus of biological analysis (e.g.

assessments and surveys). The adaptations of vegetation to living in saturated conditions allows for the distinction between wetland and non-wetland plant species (Cronk and Fennessy, 2001). These flood-tolerant species are labeled hydrophytes (Mitsch and Gosselink, 2007). In general, the type of vegetation present can be used for the purpose of classifying wetlands.

By focusing on vegetation type, it is possible to generalize the classification of wetlands. For example, bogs are wetlands that are dominated by mosses and lichens whereas marshes are primarily composed of graminoids such as grasses, rushes, reeds, and sedges (Mitsch and Gosselink, 2007). Wetland classification based on constituent vegetation types allows for an accurate and minimally time consuming classification process as long as the physical characteristics of contrasting vegetation types can be determined.

Pope et al. (1997) were able to distinguish three classes of marshes based on an examination of the constituent vegetation type. They used C-band and L-band polarimetric radar data to classify (1) rush, (2) sawgrass, and (3) cattail dominated marshes (Pope et al. 1997). Their classifications relied heavily upon an examination of the known relation between water levels and vegetation type such as the presence of tall emergent vegetation (sawgrass) in areas of high water (Pope et al. 1997). In a similar study, Wang et al. (1998) used radar imagery to classify western Ontario wetlands, specifically looking at swamp-treed wetlands and reed marshes. They found that by using multi-date imagery they could increase mapping accuracy from 51% to greater

than 85% when compared with single-date imagery because of measurable fluctuations in local water levels. By using Radarsat-1 combined with Landsat ETM+ imagery, Grenier et al. (2007) were able to map five classes of wetlands based on the Canadian Wetland Inventory system: bog, fen, marsh, swamp and shallow water (Grenier et al. 2007).

Bourgeau-Chavez et al. (2001) cited Pope's (1997) study while using the same sensor to further the field of radar-based wetland analysis. The authors focused on flood detection beneath vegetated canopies and the differentiation between woody and herbaceously vegetated wetlands. They demonstrated the need for both L-band and C-band radar for flood detection beneath vegetated canopies and determined that the HH polarization was superior to VV for wetland discrimination.

Touzi (2007) developed a new way of analyzing the data retrieved by the sensor from wetland targets by having his decomposition output a new set of parameters that were not included in previous decomposition techniques (see Section 2.6.4). Specifically, Touzi included a unique Phase parameter, for which the purpose was to characterize the relative time it takes a wave to travel to a target and back to the sensor, which helps to identify depolarization and scattering types within imagery. It is now possible to apply this new technique to the methods, and more specifically the classification schemes, of Bourgeau-Chavez et al. (2001). Through this, it might be possible to increase wetland classification accuracy.

2.4.3 Radar Remote Sensing of Other Wetland Variables

Beyond vegetation type there are other variables that can be measured and monitored. Novo et al. (1998) focused on an examination of the relations between radar incident angle and five biophysical variables: wet weight, dry weight, percentage moisture, stand height, and percentage ground cover. The authors found that the use of multiple incident angles was beneficial to the accurate monitoring of all five variables, especially for land cover classification. Mougín et al. (1999) used several vegetation parameters in order to model biomass within the Amazon Basin using airborne polarimetric SAR. The vegetation parameters were tree height, tree diameter at breast height (DBH), tree density, basal area and total above ground biomass. The authors found that radar backscatter and above ground metrics were strongly correlated with total biomass. In a similar study of biomass, Ramsey et al. (1999) found that L-band SAR data could be used to monitor stages of regrowth in burned black needlerush dominated marshes.

By measuring the presence and condition of various biophysical variables, information about the type and physical state of wetlands can be derived. Through the association of biophysical variables with wetland vegetation types and structure it is possible to define and then classify wetland types using on-ground measurements and/or remote sensing techniques.

2.5 Deriving Information from Radar Backscatter: Polarimetric Plots

The polarization signature is defined as the relative variation of the received energy as a function of the ellipse polarization angles, ellipticity [χ] and orientation [ψ] (Figure 9); these angles can be used to produce a polarization plot (van Zyl et al., 1987). If the ellipticity is zero, the wave is linearly polarized. If the ellipticity is $\pm 45^\circ$, the wave is circularly polarized. For ellipticities between zero and 45° , the wave is elliptically polarized. If the ellipticity is negative, the rotation of the tip of the electric vector around the ellipse is clockwise, looking in the direction of propagation (referred to as right-handed). If the ellipticity is positive, the rotation of the electric vector is counter-clockwise, or left-handed. For linearly polarized waves, the orientation angle determines whether the wave is horizontally ($\psi=0^\circ$ or 180°) or vertically ($\psi=90^\circ$ or 270°) polarized.

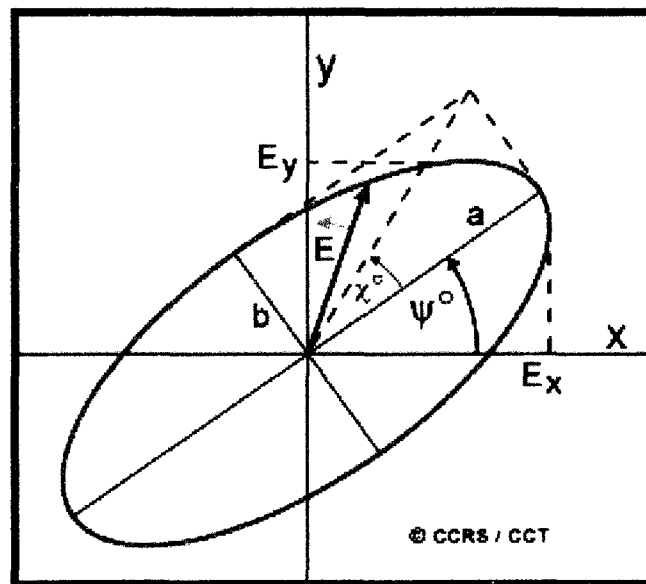


Figure 9: Drawing of the electric vector E of a fully polarized wave in the x-y plane. The tip of the electric vector traces an ellipse, with a semi-major axis "a" and a semi-minor axis "b". The ellipticity (χ) and orientation (ψ) angles are defined as shown (CCRS, 2010).

A polarimetric image contains information regarding the four linear polarizations (HH, HV, VH, VV), in addition to other polarization states (e.g. RR, RL, LR, LL), which allows for the production of a plot that represents all possible ellipticity and orientation angles.

Polarimetric plots give further insight into the scattering mechanisms involved in polarimetric images because these mechanisms depend on the nature of the imaged targets. There are two types of polarimetric plots; co-polarized and cross-polarized (Figure 10).

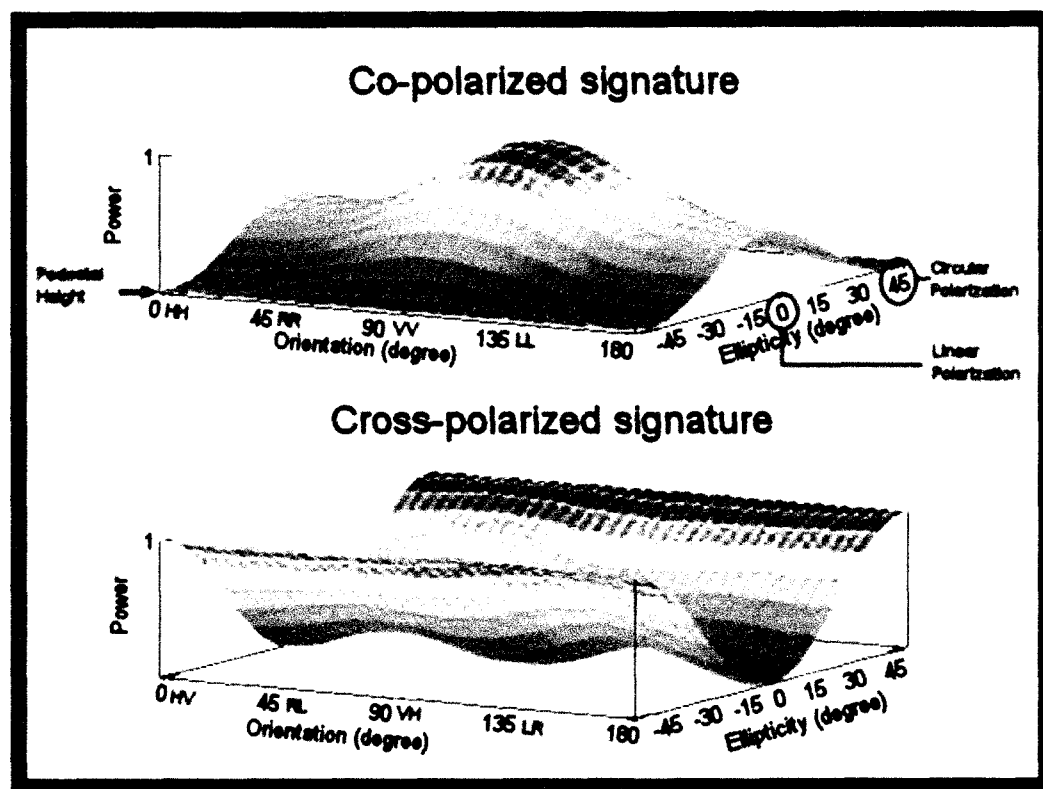


Figure 10: Co-polarized and cross-polarized signature plots displaying the orientation, ellipticity, polarization, and pedestal height parameters. The pedestal height in this plot

is very close to zero. The arrow points to the location on the y-axis that is the pedestal height.

Polarimetric plots take the average value of the selected pixels so the overall response may contain components from multiple scattering mechanisms. When analyzed in the power domain these components are additive (van Zyl et al., 1987).

Polarization signature plots include a parameter called the pedestal height, which is the minimum value of scattered power occurring within the co-polarized state for a set of pixels. The pedestal height illustrates both the de-polarization within an image, where higher values indicate a higher amount of depolarization, and a greater number of different scattering mechanisms within a target. Depolarization is a measure of how much a target changes the degree of polarization of an electromagnetic wave upon scattering (CCRS, 2008). A volume scatterer such as a forest canopy usually creates depolarization because of the many random scatterings that take place. If the pedestal height is equal to 0, the backscattered wave from a target is fully polarized. Conversely, if the pedestal height is greater than 0 there exist multiple, dissimilar scatterers within the target, and therefore a more random signal is generated.

2.6 Incoherent Target Decomposition

The objective of incoherent target decomposition is to express the average scattering mechanism (surface, diffuse, double-bounce) as the sum of the independent elements of these 3 mechanisms, which possess known physical properties (van Zyl et al.,

1987). By doing this it is possible to associate a physical mechanism with each component of the scattering matrix (HH, HV, VH, VV).

Decomposition allows the user to create a thematic map of a study area which indicates the type of land cover present at each location in the image based on differences in their backscatter properties. By combining the information contained within each polarization of a polarimetric radar image into a set of unique parameters, decomposition minimizes the negative influences of measurement noise, system calibration issues and the mixing of scattering mechanisms at one or more target pixels within an image (Hendersen and Lewis, 2008). In terms of decomposition methods, for the purpose of this thesis, the physics and mathematical aspects, which are quite complex, are not described. Instead, the aspects related to target scattering properties that can be derived from each decomposition method and their interpretation with respect to water and vegetation characteristics are presented in the results (see Section 4) portion of the paper.

2.6.1 Van Zyl Decomposition

The Van Zyl decomposition (Van Zyl et al., 1987) determines the scattering mechanism with the highest contribution to a given pixel's backscatter characteristics and then assigns it a value based on that mechanism. The possible pixel values are: 1 (odd number of reflections [surface scattering]), 2 (even number of reflections [dihedral/double-bounce scattering]), 3 (diffuse/volume scattering), and 4 (non-classifiable).

2.6.2 Freeman-Durden Decomposition

The Freeman-Durden decomposition (Freeman and Durden, 1998) determines the amount that each of the three scattering mechanisms contributes to a given pixel's backscatter characteristics and then outputs a percentage for each mechanism. Unless the backscatter from a pixel is fully polarized upon return to the sensor, which is very unlikely in real-world applications, it will contain additive contributions from two or three of the scattering mechanisms. For example, a water target will produce mostly surface scattering, but slight variations in the water's surface will cause some diffuse scattering, and even some double-bounce scattering if there are significant wave or orientation effects.

The Freeman-Durden decomposition operates similarly to the Van Zyl decomposition, but differs in the sense that it partitions the total scattered power into contributions from the three scattering mechanisms and returns all three contributions for a single pixel, whereas the Van Zyl decomposition finds the single dominant scatterer type for each pixel and assigns the pixel to the corresponding class.

2.6.3 Cloude-Pottier (H/α) Decomposition

The Cloude-Pottier method determines the amount that each of the three scattering mechanisms contributes to a given pixel's backscatter characteristics by outputting four parameters: Entropy (H), Alpha (α) angle, Beta (β) angle, and Anisotropy (A) (Cloude and Pottier, 2006). These parameters characterize the properties of partially coherent scattering.

In vector format the complex scattering matrix is represented in the Pauli basis shown in Eq.2, where T is the transpose operation:

$$\vec{k}_{3P} = \frac{1}{\sqrt{2}} [S_{HH} + S_{VV} \quad S_{HH} - S_{VV} \quad 2S_{HV}]^T \quad [2]$$

In order to compute the H and α parameters it is necessary to build the coherency matrix, which is based on the Pauli vector; Eq.3:

$$[T] = \langle \vec{k}_{3P} \vec{k}_{3P}^T \rangle = \frac{1}{2} \begin{bmatrix} \langle |S_{HH} + S_{VV}|^2 \rangle & \langle (S_{HH} + S_{VV})(S_{HH} - S_{VV})^* \rangle & 2\langle (S_{HH} + S_{VV})S_{HV}^* \rangle \\ \langle (S_{HH} - S_{VV})(S_{HH} + S_{VV})^* \rangle & \langle |S_{HH} - S_{VV}|^2 \rangle & 2\langle (S_{HH} - S_{VV})S_{HV}^* \rangle \\ 2\langle S_{HV}(S_{HH} + S_{VV})^* \rangle & 2\langle S_{HV}(S_{HH} - S_{VV})^* \rangle & 4\langle |S_{HV}|^2 \rangle \end{bmatrix} \quad [3]$$

The classification parameters (H/α), which describe the three independent scattering mechanisms in the Cloude-Pottier decomposition are based on the eigenvalues and eigenvectors derived from the coherency matrix. The Cloude-Pottier algorithm decomposes the symmetrised coherency matrix into a 3x3 unitary matrix and 3x3 diagonal matrix (Cloude and Pottier, 1996). Each eigenvector represents an orthogonal scattering mechanism, specified as a Pauli component. The diagonal of the matrix has three real, non-negative elements that represent the eigenvalues of the three scattering mechanisms. The four parameters are computed from the real eigenvalues and complex eigenvectors in the unitary and diagonal matrices.

Entropy (H) is the degree of incoherence found in the dominant scatterer and its value varies between 0 (single scatterer) and 1 (pure noise). When Entropy lies between

these two bounds there exists some form of diffusion in the target backscatter. For example, water targets usually have an Entropy value approaching 0 because the backscatter is dominated by a single surface scatterer, while vegetation targets generally have values closer to 1 since multiple scattering mechanisms affect the target backscatter.

The Alpha angle (α) identifies the type of scattering for a given target and its values range between 0° and 90° . Where $\alpha=0^\circ$ the target is a surface scatterer. Values falling between 0° and 45° indicate a diffuse scatterer, between 45° and 90° a double-bounce scatterer.

The Anisotropy (A) falls between 0 and 1 and characterizes the amount of mixing between the second and third scattering mechanisms. Where $A=0$ the two scattering mechanisms are mixed in equal proportions and their eigenvalues can be said to be equal. When $A\sim 1$ the second mechanism is dominant over the third and therefore the second eigenvalue is much larger.

The Beta (β) angle, which falls between 0° and 90° , is the orientation angle of the scatterer. The overall values of the Alpha and Beta angles at every pixel are derived as weighted averages for the values for the three eigenvectors. The weight of each value is computed for its eigenvalue divided by the sum of all three eigenvalues.

2.6.4 Touzi Decomposition

The Touzi decomposition method (Touzi, 2007) determines the amount that each of the three scattering mechanisms contributes to a given pixel's backscatter characteristics through the same means as the Cloude-Pottier decomposition, but with the addition of a complex Phase parameter (ϕ).

The Touzi decomposition output represents the orientation angle (ψ), the Dominant Eigenvalue (λ), the angle of the symmetric scattering vector in the trihedral-dihedral basis (Alpha_S : representing odd (trihedral) or even (dihedral) number of reflections), the phase (wave propagation time) difference between the vector components of the trihedral-dihedral basis (ϕ) and Helicity (τ). All of the outputs are represented in radians.

Similar to the Cloude-Pottier decomposition, the Touzi decomposition is based on the characteristic decomposition of the coherency matrix. For reciprocal (symmetrical) targets, the characteristic decomposition leads to the representation of the coherency matrix as the incoherent sum of the three independent scatterers, each weighted by its normalized and positive eigenvalue. The Touzi decomposition uses the Touzi scattering vector model (Touzi, 2007), which describes target scattering based on the Touzi parameters, to represent each coherency eigenvector in terms of unique target characteristics. Each coherency eigenvector is uniquely characterized by the 5 independent parameters listed above. Scattering type is described with a complex entity, whose magnitude (Alpha_S) and Phase (ϕ) characterize the magnitude and phase

of target scattering. The Helicity (τ) characterizes the symmetric-asymmetric nature of the target scattering. Target scattering can be characterized by an analysis of the parameters of the three eigenvectors.

3.0 METHODS

3.1 Study Area

While *P. australis* is found throughout southern Canada, the most affected wetlands are along the north shore of Lake Erie and Lake Ontario. The Big Creek and Long Point National Wildlife Areas (42°32'47"N, 80°08'24"W – see Figures 11 and 12) are part of a peninsulaic sandspit located on the north shore of Lake Erie. The Long Point peninsula is approximately 35 kilometres in length and has developed over centuries through the erosion of land to the west and the accumulation of sand along the south beach (Environment Canada 2009). The spit partially encompasses and protects a 280,000 ha lacustrine embayment (Inner Bay) and 24,000 ha of palustrine wetlands. As a result, the older vegetation communities are found to the west and north. Younger communities are found to the south and east. Typically, the older wetlands have deeper water and are often dominated by aquatic plants such as cattails, rushes and *P. australis*. Younger wetlands have a wider assortment of plants, many of which are rare in Canada (Environment Canada, 2009). The government of Ontario considers Long Point and Big Creek to be provincially, nationally, and internationally (RAMSAR) significant wetlands, which means that they provide habitat to approximately 31 endangered or threatened species and contain multiple vegetation types. Hundreds of thousands of waterfowl migrate through Long Point every spring and autumn. More than 300 different bird species migrate through the peninsula and more than 80 bird species nest on the point. There are more than 60 species of fish and many rare plants,

reptiles and amphibians. Long Point is part of a major waterfowl migration route; known as the Atlantic flyway (Environment Canada, 2009). It experiences a growing season from approximately May to August and is frozen over during the winter months, limiting the growth and spread of vegetation.

Although it has been present for >50 years, evidence suggests that since 1995, *P. australis* has been rapidly expanding across Long Point, displacing native species and potentially threatening local and migratory wildlife habitat (Wilcox et al., 2003). Individual study sites were located within the Big Creek and Long Point NWAs as well as in proximity to the NWA's borders in order to assess the potential for *P. australis* migration into, and out of wetlands.

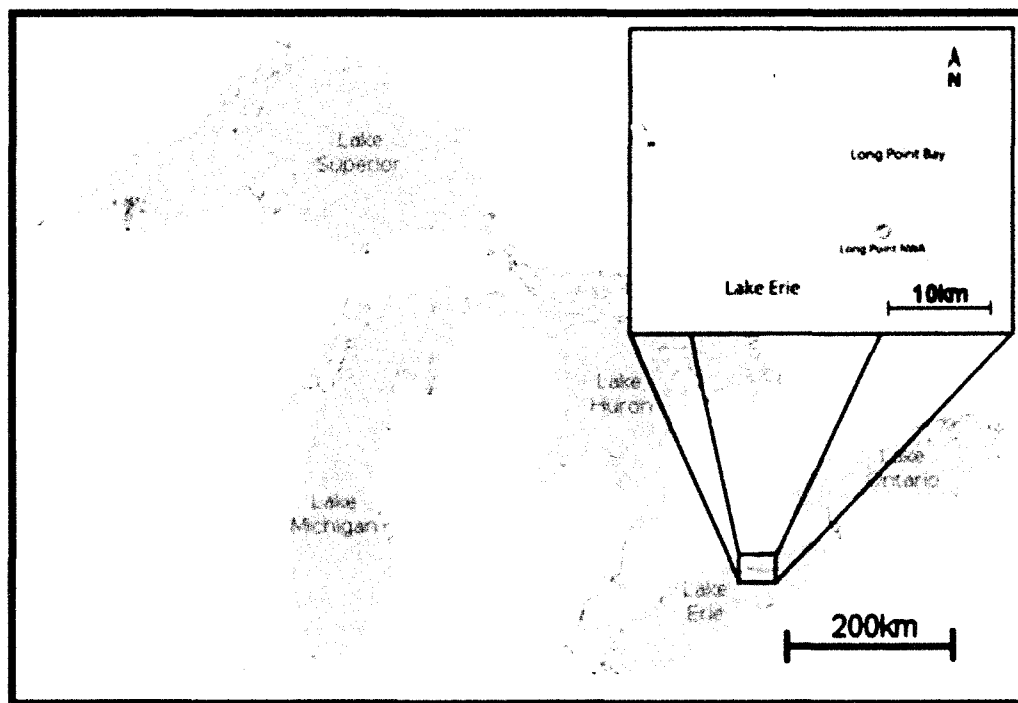


Figure 11: Long Point on Lake Erie. Big Creek NWA is found to the west, while Long Point NWA is further east (Environment Canada, 2009).

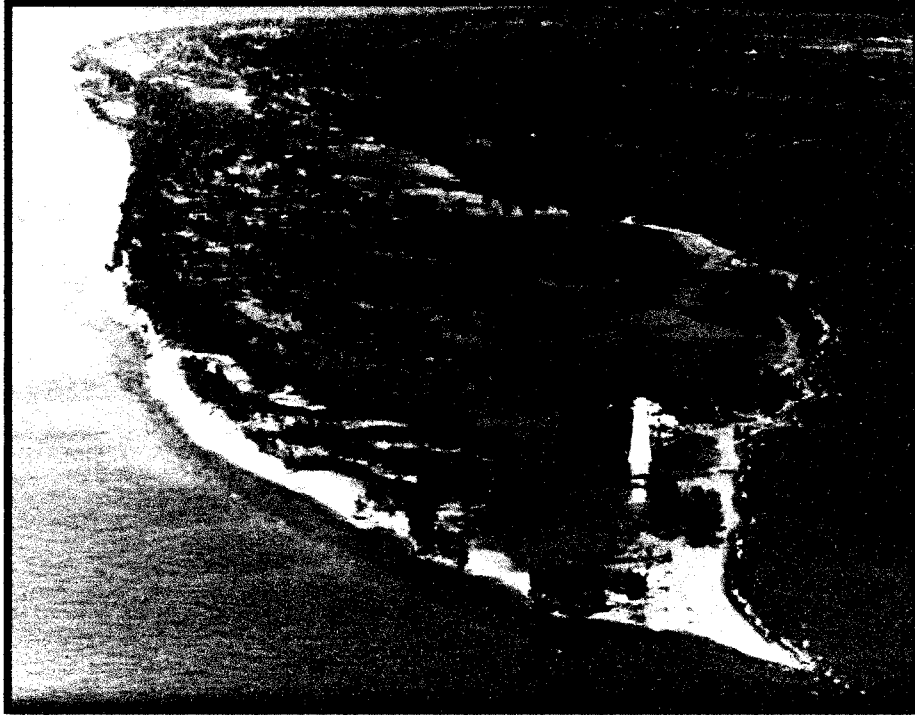


Figure 12: Oblique aerial Image of Long Point. The width of the point is approximately 200m across at the lighthouse (Environment Canada, 2009).

3.2 Field Sites

The purpose of the field data collection was to gain a quantitative understanding of the interaction of the radar signal with *P. australis* and the surrounding land cover. The field data for this research were collected in April and July/August 2009 to correspond to both the spring and summer seasons. While *P. australis* remains standing throughout the year it loses its leaves and the inflorescence begins thinning during the fall. The most common surrounding vegetation types are cattail (*typha* spp.) and various graminoid species, which senesce and are flattened as the growing season ends and the snow begins to exert force on the plants. In addition to the physical changes in the

vegetation, water levels are different between seasons. The spring snow melt causes water levels in the marsh to rise, whereas this water gradually diminishes throughout the summer. Figure 13 displays a spring 2006 aerial photo mosaic over the Big Creek and Long Point National Wildlife Areas showing the locations of all *P. australis* field transects and several *P. australis* locations derived from the aerial imagery.

A line intercept method was employed in order to collect information about patches of *P. australis* during the spring and summer seasons. A total of 25 transects, the same for both seasons, were run through patches of *P. australis*, along which measurements were taken every 3 m (Figure 14). Where the adjacent land cover to *P. australis* patches was vegetation, the transects began and ended a minimum of 12 m away from the edge of the given patch in order to gather information regarding the type and physical characteristics of the adjacent cover. In cases where the adjacent cover was water, the transects started at the water's border with the *P. australis* patch. In the case of larger patches more than one transect was used, but the total number of transects for each patch never exceeded three.

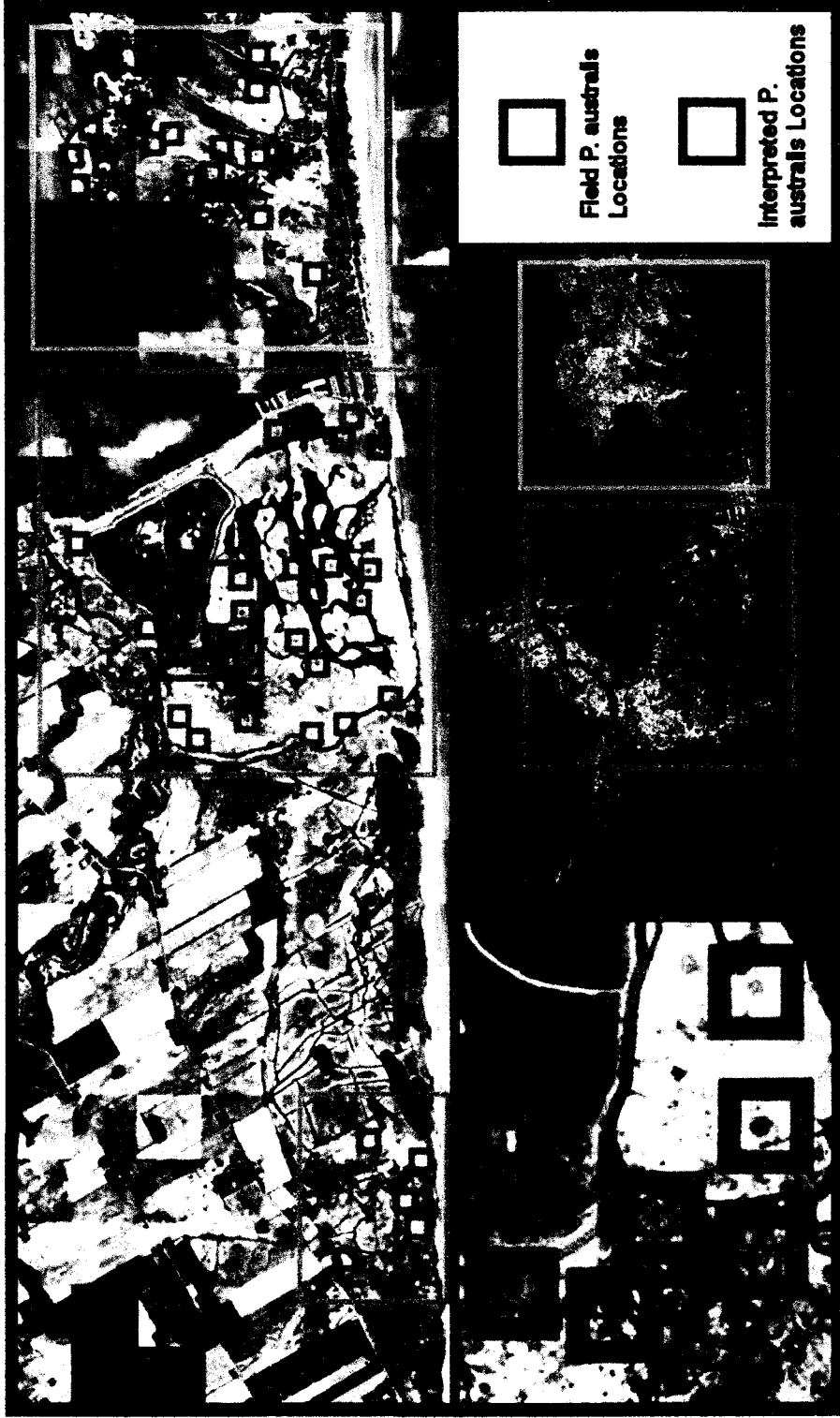


Figure 13: Spring 2006 aerial photo mosaic over the Big Creek National Wildlife Area showing the locations of all *P. australis* field transects (red) and several *P. australis* locations interpreted from the aerial imagery. The bottom left image displays a close-up view of some visible *P. australis* patches and sample transects. A single-polarized HH radar image is included for context (lower right). Big Creek NWA is highlighted in bright green (two sections); while Long Point NWA is highlighted in light blue.

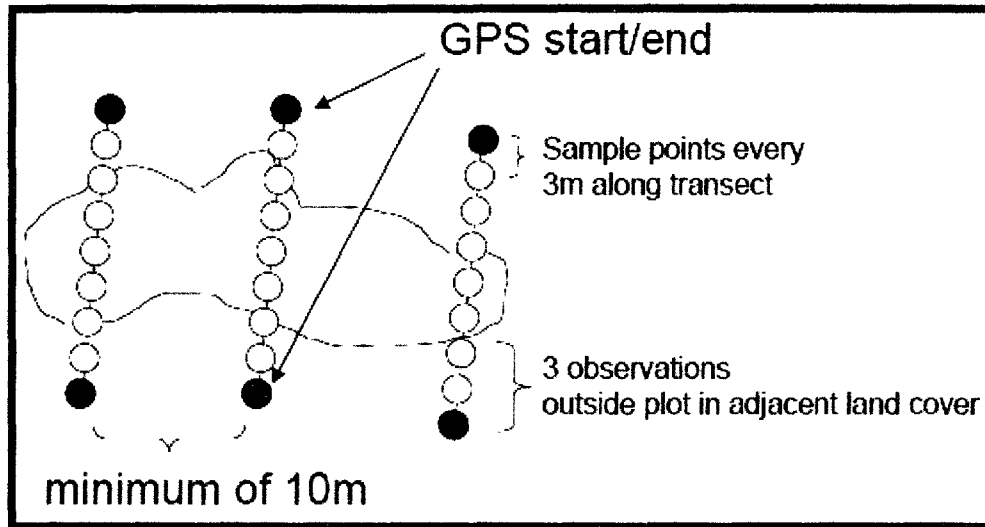


Figure 14: Line intercept method for transecting *P. australis* patches.

The start and end point of each patch was marked with a differential GPS point with an expected error of <math><1.5\text{ m}</math> (Trimble, 2009). A compass was used in order to maintain a straight path through the patches, while a surveyor's measuring tape was used to determine the distance to each data collection point at 3m intervals. At each interval, water depth (cm), cover type (general, species) and vegetation condition (flushing, senescent) were recorded. The Braun-Blanquet method (Wikum and Shanholtzer, 1978) was used to record the dominant vegetation height, maximum vegetation height and percent cover; these measures were used later in an analysis of vegetation separability. In addition to these measures, comments were made in regards to the overall structure of the vegetation at each point (flattened, broken, orientation) and digital images were taken for later reference. If more than one vegetation species

was present at a given point, the above information was collected for each species present. The specific classes discussed in this study are referred to as *P. australis*, Cattail, Grass (various graminoids), and Water.

3.3 Single-polarized RADARSAT-2 Imagery Acquisition and Processing

Objective 1 was to determine the optimal polarization, incidence angle and time of year for detecting small monoculture *P. australis* patches using RADARSAT-2 single-polarized Ultrafine (3m nominal ground pixel size) imagery. To do this, a total of 12, 20 km x 20 km images covering the study area were acquired; six in the spring and six in the summer, in order to correspond with the field data acquisition (Table 2). For both sets of six images, three were VV polarized and three were HH polarized, and for each set of these three images three incident angles were selected: steep (30°-36°), medium (37°-42°), and shallow (43°-48°). The incidence angles were grouped into simplified categories for ease of testing the optimal angle for *P. australis* detection. The shallow VV and steep VV spring imagery was acquired with only a 3° difference, as this was the best that could be achieved given the acquisition window.

Table 2: Polarization, incidence angle and date of acquisition for all single-polarized RADARSAT-2 imagery.

	Polarization	Incidence Angle	Incidence Category	Date
Spring	HH	30	Steep	04/26/2009
	HH	38	Medium	04/20/2009
	HH	48	Shallow	04/22/2009
	VV	30	Steep	04/02/2009
	VV	40	Medium	04/12/2009
	VV	43	Shallow	04/03/2009
Summer	HH	34	Steep	07/11/2009
	HH	40	Medium	06/17/2009
	HH	48	Shallow	07/20/2009
	VV	30	Steep	07/24/2009
	VV	40	Medium	07/10/2009
	VV	48	Shallow	07/08/2009

All of the imagery was acquired in right-look, ascending mode and the acquisitions were planned so that images with the same polarization were acquired as near in time to each other as possible. For example, the three spring HH images were acquired on April 20th (medium), 22nd (shallow), and 26th (steep). While it was not possible to control for weather, as each image acquisition was planned approximately a month in advance, no imagery was acquired during or within 12 hours of a rainfall. This timing ensured that the dielectric constant of the surface materials was not influenced by moisture from a recent occurrence of rain.

The single-polarized analysis focused on the Big Creek National Wildlife Area where the vast majority of small *P. australis* patches are found. The patches in this area

are generally circular, located in the interior of the wetland, and <100m in diameter, as opposed to the patches in Long Point study area where they are very large (often >150m), non-circular and coastal. The polarimetric imagery, with 8m pixels, would not have a high enough resolution to detect the smaller patches after filtering had been applied. The boundaries of these two areas are highlighted in Figure 13.

Each image, in ground-range sigma nought format (dB), was georeferenced using the Radar Specific Model for RADARSAT-2 (PCI Geomatics, 2009), which resulted in an RMS error of <(0.60, 0.60) pixels. The minimum number of ground control points (GCPs) used for each image was 12. The DEM used in the georeferencing process was a 1:50000 20 m cell size set of two tiles acquired from Geobase (NRCan, 2009). The DEM files were converted to raster images, merged, and then reprojected from GCS North American 1983 to match the RADARSAT-2 imagery in the WGS 1984 UTM Zone 17T N projection. An orthorectified aerial photo mosaic with 30 cm pixel size provided by the Canadian Wildlife Service was used to gauge the accuracy of alignment for the radar imagery and the ground GPS points. Toutin's (PCI Geomatics, 2009) radar orthorectification model was also tested, but it was found to produce much less accurate alignment. Once georeferenced, all of the imagery was clipped to a size of 10 km x 5 km, which covered the entire study area and allowed for much faster processing. Table 3 displays the RMS georeferencing error for the single-polarized radar images.

Table 3: Average root mean square for all single-polarized imagery.

	Polarization	RMS Error Pixels (x,y)
Spring	HH	0.48, 0.53
	HH	0.52, 0.54
	HH	0.44, 0.49
	VV	0.45, 0.57
	VV	0.45, 0.54
	VV	0.52, 0.53
Summer	HH	0.43, 0.51
	HH	0.45, 0.56
	HH	0.52, 0.60
	VV	0.52, 0.56
	VV	0.45, 0.54
	VV	0.51, 0.52

3.3.1 Speckle Filtering

Several image filter algorithms were tested, including: Standard Deviation (Lee and Jurkevich, 1994), Boxcar (Lee and Jurkevich, 1994), Frost Adaptive (Frost, 1982), Enhanced Frost Adaptive (Lopes, 1990), Lee Adaptive (Lee, 1981), Enhanced Lee Adaptive (Lopes, 1990), and Kuan (Kuan, 1987). The filters were assessed based on a visual inspection of their ability to distinguish known patches of *P. australis* from the surrounding vegetation; all images were tested using 3 window sizes, 3x3, 5x5, and 7x7. The 3x3 Lee Standard filter was determined to be the best based upon a visual inspection of the imagery. The larger window sizes (5x5 and 7x7) were found to blur the boundaries of visible vegetation patches and waterways. The Lee Standard filter focuses more on the removal of high-frequency noise and less on edge preservation, unlike the Lee Adaptive filter, which was found to be unsuitable for small vegetation patches with

non-distinct and non-linear edge features. Figure 15 displays a *P. australis* patch under different filtering conditions.

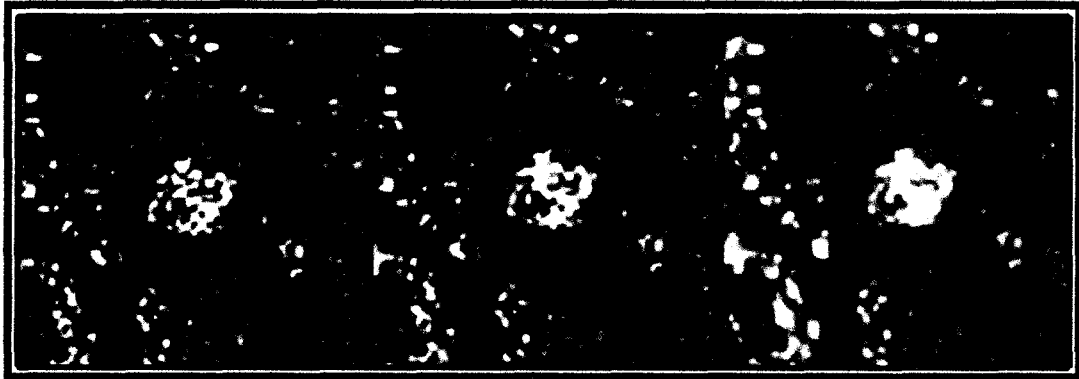


Figure 15: *P. australis* patch (bright circle in the centre of each box) under 3 filtering conditions; (left) unfiltered, (centre) enhanced Lee, (right) standard Lee in a steep incidence angle HH, spring image.

3.4 Determination of an Optimal Image Data Set for Discrimination of Vegetation Types

3.4.1 Separability Analysis

A separability analysis based on radar brightness (σ^0) and radar texture imagery was used as a means of assessing the degree to which *P. australis* could be separated from other vegetation types across multiple images. The goal of this analysis was to determine the best combination of seasonal imagery, polarizations and incidence angles for detecting *P. australis*. In essence, a separability analysis can be used to determine whether or not classes should be merged before performing a classification and it is possible to use multiple images as the input to the separability analysis, which allows

multi-temporal, multi-spatial, multi-sensor, and multi-spectral analysis to be conducted (Lillesand and Keifer, 2004). For this study, both the filtered radar brightness (3x3 Lee Standard) and radar texture images were used in the separability analysis.

3.4.2 Texture Analysis for Single-Polarized Radar Imagery

Texture is a measure of the spatial variance observed in a moving window across an image and is defined as the frequency of tonal change and spatial distribution associated with those changes (Lillesand and Keifer, 2004). In radar applications, texture is commonly referred to as “graininess” or “roughness”. Texture analysis can provide vital information related to the spatial and structural arrangement of targets within an image.

The Mean grey level co-occurrence matrix (GLCM) texture measure (Equation 4) with a window size of 5x5 (15x15m) was used in this study as it produced the most separable visual results based on a test of several texture measures (Homogeneity, Contrast, Dissimilarity, Standard Deviation) and window sizes (3x3, 5x5, 7x7, 9x9, 11x11). The GLCM is a two-dimensional matrix that computes the probability of combinations of two pixel grey values within a defined window size (Arzandeh and Wang 2002). The Mean texture measure uses both tone and texture to calculate the average grey level pairs by calculating the variance between grey levels in each line in the GLCM matrix (PCI Geomatics, 2009), and has been shown to be a useful measure for classifying land cover types in radar images (Sokol, 2003; Pultz and Brown, 1987; Treitz et al., 2000; Treitz and Howarth 2000).

$$\mu_i = \sum_{i,j=0}^{N-1} i(P_{i,j})$$

[4]

Where:

N = number of grey levels

P = probability of the pixel grey values (i,j) in the normalized symmetric GLCM of dimension N x N

Figure 16 shows examples of poor quality (homogenous) and better quality (heterogeneous) Mean texture images derived from the single-polarized dataset. The latter has greater information content with respect to land cover type and condition.



Figure 16: Top - poor quality (shallow VV summer) and bottom - better quality (steep HH spring) Mean texture images derived from the single-polarized radar dataset. A combination of better quality texture images allows for a good characterization of the study area.

The Mean texture measure was extracted from all of the single-polarized Radarsat-2 images using 10 randomly selected sample windows (7x7 pixel window, selected by trial and error) derived from the *P. australis* field transects and 10 randomly selected sample windows (7x7 pixel window) derived from non-*P. australis* areas of known vegetation composition (Cattail and Grass) (Figure 17).



Figure 17: Sample window locations. The green arrows indicate the location of a *P. australis* sample used in the initial separability analysis from the Big Creek study area.

Since some confusion was expected when working with 3 vegetation classes and the goal of this research was to detect only *P. australis*, it was necessary to aggregate the non-*P. australis* vegetation into one class (Other). This process also simplified the

separability analysis applied in the next step since there were only two classes to compare (*P. australis* vs. Other). All of the sample windows were derived from homogeneous (single-class) areas of the imagery representing at least 25 x 25m on the ground. The images were not filtered before the Mean texture measure was computed in order to reduce the smoothing of image tones and variations between grey level values. A sample spacing of 1 pixel and omni-directional sampling (Sokol, 2003) were used. The output texture images were input into the separability analysis along with brightness images as described below.

3.4.3 Separability Measures

The Bhattacharyya Distance (BD) is a distance measure inversely weighted by sample variance, which measures the similarity of two discrete or continuous probability distributions and quantifies the amount of overlap between two statistical samples (Jensen, 2007).

The BD separability measure results in a value between 0 and 2, which is related to the probability of correct classification between the two input classes. Where the value is 0 the classes are not separable at all, meaning the signatures are identical. Where the value is 1.9-2 the classes are distinctively different. When the values are below 1.0, the classes cannot be distinctly defined and separability is classified as “very poor”. A separability value between 1.0 and 1.7 indicated that the two input classes are somewhat different, but not confidently separable. For such values it is possible that there may be too much internal variation, which would not cause a “very good”

classification and result in insufficient information for decision support. Richards (1994) provides a graph of separability verses potential classification accuracy, indicating values above 1.7 correspond to potential accuracies of greater than 80%. The separability analysis was conducted between same-class samples (*P. australis* vs. *P. australis* samples) as well as across classes (*P. australis* vs. Other) in order to characterize the between-class variance and within-class variance. Table 4 displays the image combinations utilized in the initial separability analysis, which discriminate vegetation classes based on season and brightness/texture. A further analysis (Section 4.1.2) focused on further discrimination based on incidence angles and polarization. All of the samples used in the separability analysis were confirmed to be normally distributed using a series of probability plots.

Table 4: Image combinations for the separability analysis discriminating season and brightness/texture.

Image Composition (label)	Images Included in Separability Analysis
Bright_All	All filtered (3x3 Lee) Radarsat brightness images (12 images) (12 channels)
Spring_Bright	Spring (3x3 Lee) Radarsat brightness images (6 images) (6 channels)
Summer_Bright	Summer (3x3 Lee) Radarsat brightness images (6 images) (6 channels)
Texture_All	Texture (Mean 7x7) images (12 images) (12 channels)
Spring_Texture	Spring texture (Mean 7x7) images (12 images) (12 channels)
Summer_Texture	Summer texture (Mean 7x7) images (12 images) (12 channels)
Radar_All	All filtered (3x3 Lee) and all texture (Mean 7x7) images (24 images)
Spring_Bright_Texture	Spring filtered (3x3 Lee) and Spring texture (Mean 7x7) images (12 images)
Summer_Bright_Texture	Summer filtered (3x3 Lee) and Summer texture (Mean 7x7) images (12 images)

The goal of the initial analysis was to select images that had the most information content and were therefore heterogenous across the different classes in terms of brightness and texture values. Based on a visual inspection, many of the images

were very homogeneous (see Figure 16) and it was not possible to separate within-class (*P. australis* vs. *P. australis*) or cross-class (*P. australis* vs. Other) samples. For this reason all of the samples, both within-class and cross-class, were utilized in the first separability analysis. Although the overall goal would normally be to select images that reduce within-class separability while increasing cross-class separability, this was found to be impossible given that the images that reduced within-class separability also greatly reduced cross-class separability, which indicated that those images were very noisy. The solution was to run the initial separability analysis on all samples in order to select the most heterogeneous images for further analysis.

The output separability matrices were used to determine the most suitable combination of images for separating the vegetation classes. The matrices allowed for an examination of the single most useful image and the combination of images, which proved to be the most suitable for separating the vegetation classes based on polarization, incidence angle, and time of year.

The separability analysis was repeated using 10 different class samples derived from the field data to ensure that the test was repeatable and accurate. When the analysis was rerun the separability values did not vary significantly so only the results from the first run are discussed here.

The initial separability analysis, based on season and texture/brightness, indicated that the spring season texture imagery and spring season texture/brightness imagery produced the highest level of separability (between-class and cross-class), as

described in Section 4.1.1. Since the spring texture imagery produced the best results with the fewest number of channels, the six images included in this dataset were further analyzed in order to determine the optimal combination of polarizations and incidence angles for detecting *P. australis*. First, the spring texture imagery was assessed for incidence angle by breaking the original dataset into smaller groups (e.g. Steep only; HH and VV). The imagery was also assessed for polarization alone (e.g. HH only; 3 incidence angles). Then, combinations of polarization and incidence angle were tested.

Since the goal of this study was to detect only *P. australis*, the next part of the separability analysis involved assessing only cross-class separability (*P. australis* vs. Other), as opposed to overall separability, which was assessed in the previous steps. All permutations of the six texture images were assessed for cross-class separability. This included using anywhere from 1-6 images and the top 3 results were selected for discussion.

The final portion of the separability analysis involved examining the physical characteristics of *P. australis* patches in order to determine which features made them more or less separable. This analysis looked at the three most separable patches and three least separable patches derived from the initial 10 sample windows used in the separability analysis. The physical characteristics that were assessed were patch size, average water depth (cm), dominant height (m), maximum height (m), and percent cover. The values from these parameters were compared to the texture values derived from the imagery and reasons for good/poor separability were discussed.

3.4.4 Modelling and Mapping *P. australis* Distribution

Once the optimal single-polarized images for *P. australis* detection were identified the appropriate image values were examined for most and least separable cross-class samples. These values were compared to the field data in order to determine the physical characteristics associated with patch separability. The results from the separability analysis (optimal images) and brightness statistics (detectable values), based on the physical patch characteristics, were input into a simple model, based on the standard deviation of texture values, in order to allow patches of *P. australis* to be mapped. The standard deviation of texture values was selected because it was a simple way of utilizing a range-based measure which could be adjusted during the testing of the classification rules. A map of the Big Creek study area, where the majority of the circular *P. australis* patches was found, was created using a combination of this simple moving window (standard deviation of pixel values) classifier and object-based classifier which outlined the extent of the *P. australis* patches. The map was later assessed for accuracy.

3.5 Fully Polarized RADARSAT-2 Imagery Acquisition and Processing

Objective 2 was to establish the best image processing and decomposition methods for detecting large patches of *P. australis* using RADARSAT-2 fully polarimetric (8m nominal ground pixel size) imagery. To do this, a total of six, 25 km x 25 km images covering the study area were acquired; three in the spring and three in the summer in

order to correspond with the field data acquisition (Table 5). For each set of three images three incident angles were selected; steep (22°-26°), medium (27°-31°), and shallow (32°-40°).

Table 5: Polarization, incidence angle and date of acquisition for all fully polarized RADARSAT-2 imagery.

	Incidence Angle	Incidence Category	Date
Spring	23	Steep	04/23/2009
	28	Medium	04/06/2009
	40	Shallow	05/06/2009
Summer	23	Steep	07/28/2009
	30	Medium	07/31/2009
	39	Shallow	07/25/2009

The same imaging criteria were applied as described in Section 3.3: right-look, ascending mode images acquired close in time (e.g. July 25th (shallow), 28th (steep), and 31st (medium)) with no imagery acquired during or within 12 hours of rainfall. The spring image acquisitions were spaced further apart, but the structure of the vegetation did not change drastically as the study area had not yet begun the spring growth period.

3.5.1 Vegetation Class Discrimination Using Co-polarized and Cross-Polarized Scatter Plots

The polarimetric analysis began with the creation of co-polarized and cross-polarized scatter plots based on radar intensity (decibel) values as described in Section 2.5. These scatter plots allowed for visual analysis of between-class separability within the imagery and provide a simple means of determining which images may produce the most informative datasets for subsequent use in decomposition since the most

separable images should contain the most useful informational content as there is a relationship between backscatter at different polarizations and the decomposition parameters.

The raw polarimetric images were first filtered using the Enhanced Lee filter with a 5x5 pixel window size, which was found to be optimal based on tests similar to those used for the single-polarized imagery, in order to reduce noise in the imagery. For each of the three vegetation classes (*P. australis*, Grass, Cattail) and Water class, 30 samples were extracted from a combination of known field site transects and aerial imagery interpretation. A sample window was created at each sample location, under which a 5x5 pixel-size sub-section of data was extracted from each image layer (HH, HV, VH, VV). This allowed 750 individual pixels (30 for each sample) for all of the 4 classes to be input into each scatter plot. The same sample window extraction method was applied to all 6 polarimetric images and the extracted data were confirmed to be normally distributed using a Student's *t*-test before being input into the scatter plots. Since the purpose of this study was to generate maps over entire wetland areas, or at least large sub-sections of these areas, average class values were used. Otherwise, the parameters on which the vegetation classes are classified would be too specific to detect specific vegetation classes throughout the study area. Variations within the vegetation classes, on a per-sample basis, are discussed later when classification maps are created using information derived from the field data. For each polarimetric image all possible scatter plots were created: HH/VV, HH/HV, HH/VH, VV/HV, and VV/VH.

3.5.2 Polarimetric Plots

For each of the 6 polarimetric images a representative set of polarimetric plots, derived from field transect locations, were created for the 3 vegetation classes and Water class. Therefore, a total of 24 co-polarized and 24-crosspolarized plots were output from the imagery. The plots are based on the average backscatter responses of 5 randomly selected field locations for each class to ensure a representative sample of the inter-class variability.

3.5.3 Vegetation Class Discrimination Using Polarimetric Decomposition

The four polarimetric decomposition methods described in section 2.6 were utilized for this research: Van Zyl, Freeman-Durden, Cloude-Pottier, and Touzi. The Van Zyl and Freeman-Durden decompositions are relatively simple, as they focus on revealing which of the three scattering mechanisms (double-bounce, volume, surface) produce a given pixel value in an image. The Cloude-Pottier and Touzi decompositions expand upon this and make use of additional parameters that are derived in various ways from the backscatter intensity and phase information at a given pixel.

This research makes use of the first two decompositions as a means of deriving basic scattering information from the image classes, while the latter two decompositions are utilized as a way of extracting more precise information that can be used to make inferences about more detailed target characteristics such as density and water presence. The output from the decompositions was analyzed in order to gain

insight into the information that can be extracted from such methods, from simple (Van Zyl/Freeman Durden) to complex (Cloude-Pottier/Touzi). The unique parameters derived from the more complex decompositions that best characterized differences in the vegetation classes were input into a separability analysis.

3.5.4 Decomposition Methods

The dominant scattering mechanism for each pixel in the polarimetric images was derived using the Van Zyl decomposition. The Van Zyl decomposition internally converts the input polarimetric data set to the symmetrised covariance format. The effective number of looks, which determines the spatial resolution of an image based on the averaging of intensity values over a range of pixels, was increased to a minimum of 25 using the Enhanced Lee (5x5) filter and the output for each of the 6 polarimetric images was a single-channel byte image with pixel values that represented the Van Zyl class number (from 1 to 4). In addition to this image the dominant class percentage (%), based on pixel count, was output.

The contribution of each scattering mechanism to individual pixels within the polarimetric images was derived using the Freeman-Durden decomposition. The Freeman-Durden decomposition was run on each of the 6 polarimetric images with the Enhanced Lee (5x5) filter applied. The output pixel values represent the same physical quantity as the input data set (σ^0) and are represented by a 3-channel floating point

pixel file, signifying the total power at each pixel from the three Freeman-Durden scattering mechanisms.

The contribution of each scattering mechanism to individual pixels within the polarimetric images was derived using the Cloude-Pottier decomposition. The Cloude-Pottier decomposition was run on each of the six polarimetric images with the Enhanced Lee (5x5) filter applied. The output file contained four floating point pixel channels with the Entropy, Anisotropy, Beta angle, and Alpha angle defined. The two angles were represented in degrees.

The contribution of each scattering mechanism to individual pixels within the polarimetric images was derived using the Touzi decomposition. The Touzi decomposition was run on each of the six polarimetric images with a 5x5, 7x7 and 11x11 window size. All output values were represented in radians.

3.6 Separability Analysis of Polarimetric Decompositions

A separability analysis based on the output of the polarimetric decompositions was used as a means of assessing the degree to which *P. australis* could be separated from other vegetation types using the decomposition output parameter images. The goal of this analysis was to determine the best combination of seasonal imagery, polarizations, incidence angles, and decomposition methods for detecting *P. australis*.

As in the single-polarized image analysis, the Bhattacharyya Distance was used as the separability measure and the initial analysis focused on selecting the most heterogeneous (least noisy) images. Table 6 displays the image combinations used in the initial separability analysis which focused on determining the optimal season and decomposition method for separating vegetation samples (between-class and cross-class).

Table 6: Image combinations for polarimetric/decomposition separability analysis.

Image Composition (label)	Images Included in Separability Analysis
All_Radar_Filtered	All filtered (5x5 Enhanced Lee) images (6 images) (24 channels)
Summer_Filtered	Summer filtered (5x5 Enhanced Lee) images (3 images) (12 channels)
Spring_Filtered	Spring filtered (5x5 Enhanced Lee) images (3 images) (12 channels)
All_Touzi	All Touzi images (6 images) (30 channels)
Touzi_Summer	Summer Touzi images (3 images) (15 channels)
Touzi_Spring	Spring Touzi images (3 images) (15 channels)
All_CP	All Cloude-Pottier images (6 images) (24 channels)
CP_Summer	Summer Cloude-Pottier images (3 images) (12 channels)
CP_Spring	Spring Cloude-Pottier images (3 images) (12 channels)
Touzi_CP	All Touzi and all Cloude-Pottier images (12 images) (54 channels)
Touzi_CP_Summer	Summer Touzi and Cloude-Pottier images (6 images) (27 channels)
Touzi_CP_Spring	Spring Touzi and Cloude-Pottier images (6 images) (27 channels)
Touzi_Filtered	All Touzi and all filtered (5x5 Enhanced Lee) images (12 images) (54 channels)
Touzi_Filtered_Summer	Summer Touzi and filtered (5x5 Enhanced Lee) images (6 images) (27 channels)
Touzi_Filtered_Spring	Spring Touzi and filtered (5x5 Enhanced Lee) images (6 images) (27 channels)
CP_Filtered	All Cloude-Pottier and all filtered (5x5 Enhanced Lee) images (12 images) (48 channels)
CP_Filtered_Summer	Summer Cloude-Pottier and filtered (5x5 Enhanced Lee) images (6 images) (24 channels)
CP_Filtered_Spring	Spring Cloude-Pottier and filtered (5x5 Enhanced Lee) images (6 images) (24 channels)

Similar to the single-polarized analysis, separability was calculated for 10 randomly selected samples (Figure 18) from each of two classes: the *P. australis* class and an aggregated class derived from known locations of both Cattail and Grass classes (Other). The separability analysis was repeated using a different randomly selected combination of samples derived from the field data to ensure that the test was repeatable.

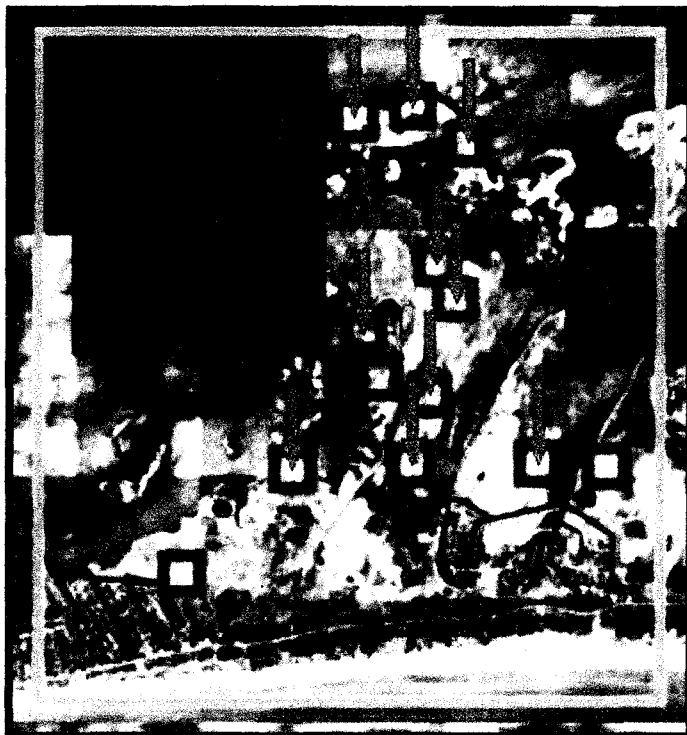


Figure 18: Sample window locations. The green arrows indicate the location of a *P. australis* sample used in the initial separability analysis from the Long Point study area.

All of the samples used in this analysis were selected from the Long Point study area since those located in the Big Creek study area were too small to be detected in the polarimetric imagery. Of the 25 field transects, only 12 could be used for the polarimetric analysis because the remaining 13 were not large enough in the imagery to accommodate the window sizes from the filtering and decomposition algorithms, so some of the samples included in the first separability analysis were also included in the second. There were an additional eight visually interpreted patches of *P. australis* located in the Long Point study area, so these were added to the separability analysis.

When the analysis was rerun the separability values did not vary significantly so only the results from the first run are discussed in Section 4.3.

The output separability matrices were used to determine the most suitable combination of images for separating *P. australis* from the other vegetation types based on season and decomposition method. Once the separability analysis was completed, the best results were selected for further in-depth analysis in order to determine the optimal incidence angle and specific decomposition parameters for detecting *P. australis*.

As the spring season imagery with the Touzi decomposition produced the best results in the initial analysis, followed closely by the same imagery with the Cloude-Pottier decomposition (see Section 4.3.1), cross-class separability was then tested across incidence angles for the Touzi and Cloude-Pottier decompositions of the spring imagery.

Several decomposition parameters were selected from both the Touzi and Cloude-Pottier decompositions based on previous analyses. These parameters were combined into a new separability analysis in order to determine if separability could be increased by extracting information from more than one decomposition method. All possible combinations of these parameters were tested.

3.6.2 Modelling and Mapping *P. australis* Distribution

Once the optimal quad-polarized parameters (season, incidence angle) and decomposition method for *P. australis* detection were identified the appropriate decomposition parameters were examined for the most and least separable cross-class samples. These values were compared to the field data in order to determine the physical characteristics associated with patch separability. As for the single polarization analysis (Section 3.4), the results from the separability analysis and the resulting optimal image and decomposition parameters which were based on the physical patch characteristics were input into a simple rule-based model in order to allow patches of *P. australis* to be mapped. The model is described in detail in Section 3.4.4 as the model parameters depended on the results of the analytical phase of the study. A map of the Long Point study area, where the majority of the very large *P. australis* patches were found was created and assessed for accuracy using a basic commission/omission analysis of patch presence.

4.0 RESULTS

4.1 Single-Polarized Results

4.1.1 Separability Analysis Based on Radar Texture and Brightness

The average separability for each of the nine image combinations was calculated and is presented in Table 7. Approximately half of the image combinations resulted in “very poor” or “poor” average separability, which indicated that these images were very homogenous. Two of the image combinations had average separability values above 1.7, which have been shown to produce accuracies of up to 80% (Richards, 1994). Two of the image combinations produced “very good” average separability results, including the spring texture and spring texture/brightness images. The remainder of this analysis will focus on the two image combinations that produced average separability values of 1.9 or greater.

Table 7: Average BD separability results for the three image combinations.

Image Composition	Average Separability	Minimum Separability	Maximum Separability	Separability Class
Spring_Texture	1.9	1.5	2.0	Very Good
Spring_Bright_Texture	1.9	1.4	2.0	Very Good
Bright_All	1.8	1.3	1.9	Good
Texture_All	1.7	0.6	2.0	Good
Bright_All	1.3	0.3	2.0	Poor
Radar_All	0.9	0.3	2.0	Very Poor
Summer_Bright_Texture	0.8	0.3	1.8	Very Poor
Summer_Texture	0.8	0.6	1.8	Very Poor
Summer_Bright	0.4	0.3	1.7	Very Poor

The spring texture images (six channels) and spring brightness/texture images (12 channels) produced average separability results with the same level of success. This indicated that many of the sample sites, even within-class, had distinct features and were separable from each other in some, but not all cases. In the same vein, since the spring texture images, with only six channels, produced the same results as the brightness/texture images, with 12 channels, the spring texture images can be considered superior, as this combination requires less information to produce the same level of separability. As previously stated, it was not possible to reduce within-class separability while increasing cross-class separability using the imagery acquired for this study. Within-class separability was found to decrease at approximately the same rate as cross-class separability as a result of noise in the imagery, so the initial separability analysis was used as a means of selecting the most heterogeneous imagery which could later be used to separate only cross-class (*P. australis* vs. Other) samples.

The spring texture imagery generally showed high separability (Table 8). Tables 8 and 9 are subsets of the entire 20x20 matrices showing the first four of 10 total samples for both the *P. australis* and Other classes. The best separability was found to be between the *P. australis* and Other in all but one case (*P. australis*2 and Other3). As was expected, the lowest average separability values were found when comparing similar *P. australis* patches, derived from the sample windows, indicating that in some cases these samples could not be separated. An examination of the field data showed that when comparing *P. australis* samples that did not have any surface water present, the average separability was low (e.g. *P. australis*3 and *P. australis*4). In cases where

surface water was present for both samples, or when surface water was present for one and not for the other, average separability was found to be higher.

Table 8: Subset of BD average separability results for 4/10 samples from spring texture image composition.

	<i>P. australis</i> 1	Other1	<i>P. australis</i> 2	Other2	<i>P. australis</i> 3	Other3	<i>P. australis</i> 4	Other4
Other1	2.0							
<i>P. australis</i> 2	1.7	2.0						
Other2	1.9	1.8	1.9					
<i>P. australis</i> 3	1.6	2.0	1.6	1.9				
Other3	1.9	1.9	1.8	1.9	2.0			
<i>P. australis</i> 4	1.7	2.0	1.7	2.0	1.5	1.9		
Other4	2.0	1.7	1.9	1.9	1.9	1.8	2.0	

The spring brightness/texture imagery generally showed high separability, but lower separability was found between the *P. australis* and Other classes (Table 9) when compared to the texture imagery alone. The high average separability values across all classes was balanced out by an increase in the number of Other samples that were found to be well distinguished from each other (e.g. Other1 and Other4). This makes sense since several of the samples were comprised of different vegetation classes (Cattail vs. Grass).

Table 9: Subset BD average separability results for 4/10 from spring brightness/texture image composition.

	<i>P. australis</i> 1	Other1	<i>P. australis</i> 2	Other2	<i>P. australis</i> 3	Other3	<i>P. australis</i> 4	Other4
Other1	1.9							
<i>P. australis</i> 2	1.8	1.9						
Other2	1.8	1.9	2.0					
<i>P. australis</i> 3	1.6	1.7	1.7	2.0				
Other3	1.9	1.9	2.0	1.9	1.7			
<i>P. australis</i> 4	1.7	1.9	1.6	1.9	1.4	1.8		
Other4	1.9	2.0	1.9	1.9	2.0	2.0	1.9	

In both of the above cases, the majority of class pairs were separable (in spite of the specific class), indicating that the radar texture outputs are sensitive to variability in the structural and wetness characteristics of the individual samples.

The remaining two image combinations that produced average separability values of 1.7 or greater (Bright_All and Texture_All) can be considered to be good class separators, but they both contain information from the top two image combinations, meaning that their slightly lower average separability values are due to additional noise. In terms of this separability analysis, fewer images produce better separability results as long as the optimal images are selected. Therefore, GLCM Mean texture alone is the best at distinguishing the classes.

4.1.2 Improving Separability through Image Channel Reduction

Since high levels of successful separability can be achieved with only six image channels (texture) representing seasonal and brightness/texture characteristics, it is possible that even fewer channels can be used to produce the same or even better levels of separability. By constraining the image channels related to polarization and incidence angle in the already successful average separability analysis, a new separability output was produced (Table 10 and Table 11).

Table 10: Average BD separability results for six new image combinations (constrained for incidence angle) from the original spring texture average separability analysis.

Original Image Composition	Images Contained in New Composition	Average Separability	Minimum Separability	Maximum Separability	Separability Class
Spring_Texture	Steep Only (2 channels)	1.9	1.6	2.0	Very Good
	Medium Only (2 channels)	1.9	1.5	2.0	Very Good
	Shallow Only (2 channels)	1.6	1.5	1.9	Poor
	Steep/Medium (4 channels)	1.8	1.5	2.0	Poor
	Steep/Shallow (4 channels)	1.7	1.5	2.0	Good

Table 11: Average BD separability results for two new image combinations (constrained for polarization) from the original spring texture average separability analysis.

Original Image Composition	Images Contained in New Composition	Average Separability	Minimum Separability	Maximum Separability	Separability Class
Spring_Texture	HH Only (3 channels)	1.8	1.5	2.0	Good
	VV Only (3 channels)	1.7	1.5	2.0	Good

The above tables indicate that constraining incidence angle (to steep) in the spring texture imagery produces the same average separability value as the spring texture image combination from all incidence angles, but also increases the minimum separability from 1.5 to 1.6. Therefore, if class specifics are ignored as a means of selecting the most heterogeneous imagery, slightly better separability results can be achieved using only two images, including a steep incidence angle HH polarized spring texture image and a steep incidence angle VV polarized spring texture image. Constraining the original texture image combination for polarization did not improve the overall separability between classes.

4.1.3 Overall Separability of *P. australis* vs. Other Samples

While constraining the texture imagery to only the steep incidence angle HH and VV polarizations increased non-class-specific separability (*P. australis* vs. *P. australis*, *P.*

australis vs. Other, and Other vs. Other), it did not produce the highest level of overall separability between the two distinct classes (*P. australis* vs. Other) (Table 12). In order to determine overall separability all *P. australis* samples, combined, were compared to all Other samples, combined.

Table 12: Overall separability of *P. australis* and Other classes for three image combinations.

Image Combinations	Overall Separability
Spring_Texture	1.717
Spring_Bright_Texture	1.128
Steep_Only	1.213

The above results show that the texture imagery in the spring produced the best between-class separability. Since it would not be desirable to acquire six texture images (3 incidence angles; HH and VV) in the spring over one area a further channel reduction analysis was performed on all possible permutations of the six images, including single (e.g. Steep HH) images. Table 13 shows the top three results.

Table 13: Top three overall separability values for *P. australis* and Other classes for image combinations derived from a permutative channel reduction analysis of the spring texture imagery.

Image Combinations	Overall Separability
Steep HH, Steep VV, Shallow VV	1.789
Steep HH, Steep VV, Shallow HH	1.724
Steep HH, Steep VV, Medium VV	1.719

The top three results all contained three images. A high level of separability (associated with >80% distinction) between the *P. australis* class and Other class was

achieved using only three spring texture images, including: a steep incidence angle HH image, and steep incidence angle VV image, and a shallow incidence angle VV image. No two image combinations were found to be as good at separating *P. australis* from the Other vegetation class, however, utilizing just the Steep HH and Steep VV imagery, an overall separability of 1.671 (Poor) was achieved. Similarly, an overall separability of 1.115 (Very Poor) was achieved using only the Steep HH imagery.

4.1.4 Examination of Physical and Textural Characteristics of *P. australis*

The brightness values (0-255) extracted from the texture images were examined for the three (of 10) most separable samples from the separability analysis (Table 14). The three least separable samples from the separability analysis can be found in Table 15.

Starting with patch size, there is a marked difference between the most and least separable patches. In the most separable group, patch size was considerably larger than in the least separable group (Tables 14 & 15). The average water depth in the most separable group was approximately 19 cm in the spring and 5 cm in the summer, while the least separable group had an average water depth of 27 cm in the spring and 20 cm in the summer. The dominant and maximum height of the plants was slightly lower for the three least separable patches and the percent cover was significantly lower. The three most separable patches had a percent cover of 80% or higher, whereas the three least separable patches had a percent cover equal to or less than 80%. Based on these

small sample sizes the best detectable patches should be larger than 40 m x 45 m, should average approximately 4 m in (dominant) height, and should have a percent cover of at least 80%.

The least separable patches were the smallest, had the most surface water, and lowest percent cover, which could contribute to an increase in surface scattering, and therefore explain the lower texture values across both the HH and VV channels and steep/shallow incidence angles.

This examination of the field variables was repeated again on 10 randomly selected field samples in order to gain a better understanding of the texture values, which characterized patches of *P. australis*. Table 16 displays the average and standard deviation texture values for the Steep HH, Steep VV, and Shallow VV spring texture images obtained from the averaging of six of the most separable samples. The rule-based classifier described in the next section makes use of these values in order to identify *P. australis* based on texture values.

Table 14: Average, 1 standard deviation, and 2 standard deviation statistics for the *P. australis* brightness values (0-255) derived from the radar texture imagery.

	Texture Value (HH Steep)	Texture Value (VV Steep)	Texture Value (VV Shallow)
Average	247	33	115
1 StDev (68%)	36	12	24
2 StDev (95%)	72	24	48

Table 15: Physical and radar backscatter (0-255) characteristics of the three most separable *P. australis* samples derived from the single-polarized radar texture imagery.

	Patch Size (m)	Average Water Depth (cm) Spring	Average Water Depth (cm) Summer	Dominant Height (m)	Maximum Height (m)	Percent (%) Cover	Average Texture Value (HH Steep)	Average Texture Value (VV Steep)	Average Texture Value (VV Shallow)
Phrags1	42x50	15	5	4	4.5	90	245	36	111
Phrags4	45x100	18	0	4.5	4.5	80	242	29	124
Phrags8	58x60	25	10	3.5	4	85	250	39	109

Table 16: Physical and radar backscatter (0-255) characteristics of the three least separable samples derived from the single-polarized radar texture imagery.

	Patch Size (m)	Average Water Depth (cm) Spring	Average Water Depth (cm) Summer	Dominant Height (m)	Maximum Height (m)	Percent (%) Cover	Average Texture Value (HH Steep)	Average Texture Value (VV Steep)	Average Texture Value (VV Shallow)
Phrags6	20x25	30	15	3.5	4	75	64	15	28
Phrags7	40x45	25	25	4	4.5	70	201	21	120
Phrags9	30x40	25	20	3.5	4	80	197	14	90

4.1.5 Modelling and Mapping *P. australis* Distribution

While separability was found to be high overall, the separability analysis could not indicate whether or not a sample was actually composed of *P. australis* without input from known field (training) data. In order to automate the process of *P. australis* patch detection the results from the separability analysis (optimal images) and texture statistics (detectable values) were input into a simple model (Figure 19).

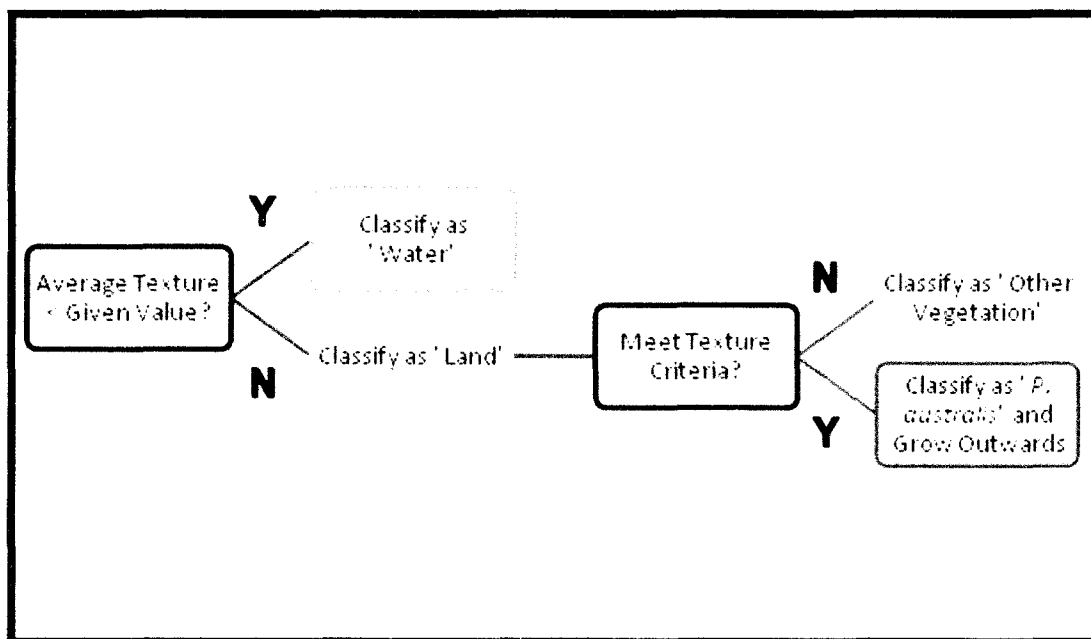


Figure 19: Model derived from the separability analysis and further investigation of the radar texture values. The model outputs a classification showing areas of water (based on surface scattering) and land (based on volume scattering). Further criteria are implemented in order to classify patches of *P. australis*.

The model was run on a subset of the radar imagery covering the Big Creek study area, where the majority of the circular patches of *P. australis* are located. Several

iterations of the model were implemented using the known statistics from the radar texture analysis and a trial and error process. The first part of the model determines whether or not a given pixel is simply water (dominant surface scattering) or land (dominant volume scattering). The average texture values for vegetation were very low (generally <20) across all three texture images, so this rule was implemented with a moving window function. If the majority of the pixels in a 5x5 window (12 pixels) were found to have values that were not >20, the centre pixel was classified as water. The window was then “grown” outwards, classifying any pixel with a value of less than 20 as water. This was repeated across the image as the window moved. Once the window reached an “edge” (several volume scattering pixels) it would start over at the next group of pixels that contained a dominant surface scattering component. Eventually the whole map was classified as either “land” or “water”.

The next step in the model operated similarly. A 5x5 moving window was used to apply the texture criteria for identifying *P. australis* to the imagery. The texture criteria was related to the average standard deviation of values derived from the texture imagery. When the window came across an area containing a majority of pixels that fell within two standard deviations of the Mean texture for each of the three images those pixels were classified as *P. australis*. Similar to the classification of land and water, the *P. australis* objects were grown outwards in all directions (not square), until no more connecting pixels which met the texture criteria were detected. The resulting image contained three classes: water, land, and *P. australis*. Since the image still contained some extraneous pixel noise it was run through a simple object segmentation algorithm

that digitized the boundaries of all 3 classes by tracing the outlines of like pixels. Figure 20 is the resulting map derived from application of the model described in Section 3.4.4.

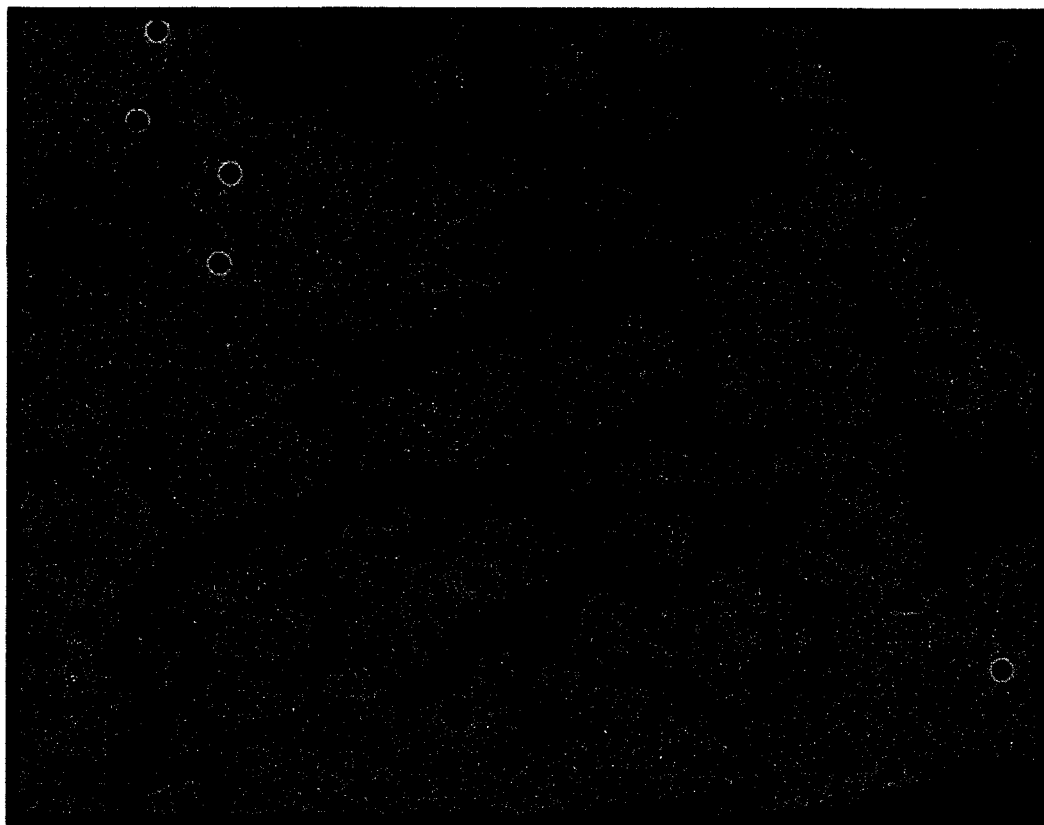


Figure 20: Classification map showing correctly identified (orange) and missed (black) patches of *P. australis* derived from the model.

4.1.6 Accuracy Assessment of the Output Map

There were a total of 15 patches identified as *P. australis* on the map and 5 missed patches that were identified in the field. In addition to this, one of the patches identified on the map as *P. australis* was not identified in the field or in the aerial image interpretation. It is not known whether this is an error of commission or actually correct.

Ignoring this patch, the detection accuracy of the model/map was 75% (15 of 20 correctly identified patches of *P. australis*).

The northwest corner of the map contained four of the five missed patches. It also displayed a large amount of water that appeared to be land in the aerial photographic imagery. An examination of the field data showed that the average water depth in the spring for these four patches was greater than 25 cm. Likewise, these four patches had lower than average percent cover (~75%). It is possible that the local physical characteristics (high water, low percent cover) contributed to the misclassification of these patches. Surface scattering would be greatly increased in this area since there was more water for the radar wave to interact with, and texture would be reduced as a result. Since these patches are all located near each other, this conclusion seems likely.

The correctly identified patches of *P. australis* on the map all appeared larger, by approximately 15% on average, than they did in the aerial imagery; however, the aerial imagery was acquired three years prior to the radar imagery and *P. australis* can spread rapidly. Overall, the patch sizes on the map were within 10-15 m in diameter of those recorded along the transects in the field.

4.2 Quad-Polarized Results

The quad-polarized results are discussed in the following order: scatter plot analysis, polarimetric plot analysis, decomposition analysis, and separability analysis. All of the analyses involve deriving class-specific information, which is later used to reinforce the findings of the quantitative investigation using separability measures.

4.2.1 Vegetation Class Discrimination Using Co-polarized and Cross-Polarized Scatter Plots

Based on an examination of the mean and standard deviation of intensity values (dB) for each class and a t-test analysis, the spring imagery acquired at a steep incidence angle was found to present the best vegetation-class separability in both the co-polarized and cross-polarized states (Table 17). Figures 21, 22 and 23 display the co-polarized and cross-polarized scatter plots for the spring and summer season imagery at each of the 3 incidence angles. For these plots the codes 'SH' = shallow, 'ME' = medium, and 'ST' = steep, while 'SP' = spring and 'SU' = summer are used.

In most cases, the Grass and Cattail classes were inseparable as there was significant overlap between the mean and standard deviation of their intensity values under almost all polarizations and incidence angles.

The *P. australis* class was inseparable from the Grass and Cattail classes in the shallow incidence angle imagery for both the spring and summer seasons, but it showed some separability in the cross-polarized medium incidence angle imagery. This separability increased in the steep incidence angle imagery and was pronounced in both

the co-polarized and cross-polarized states. Due to the high standard deviation, there is large amount of overlap in the samples even though the mean is separable. In order to reduce redundancy only the most applicable scatter plots, based on separability information, are discussed in the main body of this paper. The remaining plots are included as appendices (Appendix 1).

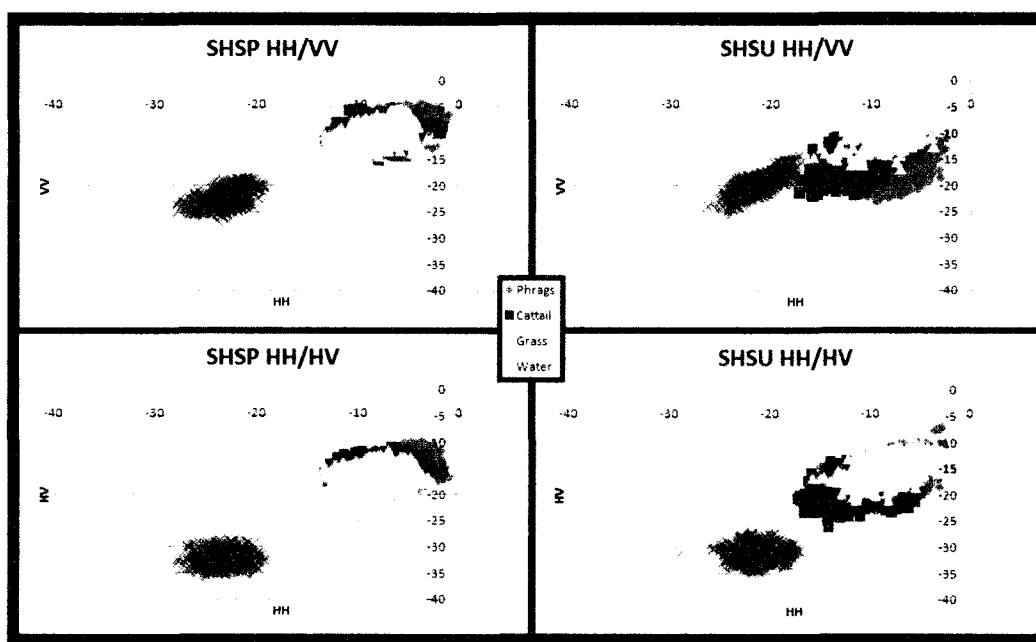


Figure 21: Scatter plots displaying the co-polarized (HH/VV) and cross-polarized (HH/HV) intensity ratios for the spring and summer quad-pol imagery at shallow incidence angles.

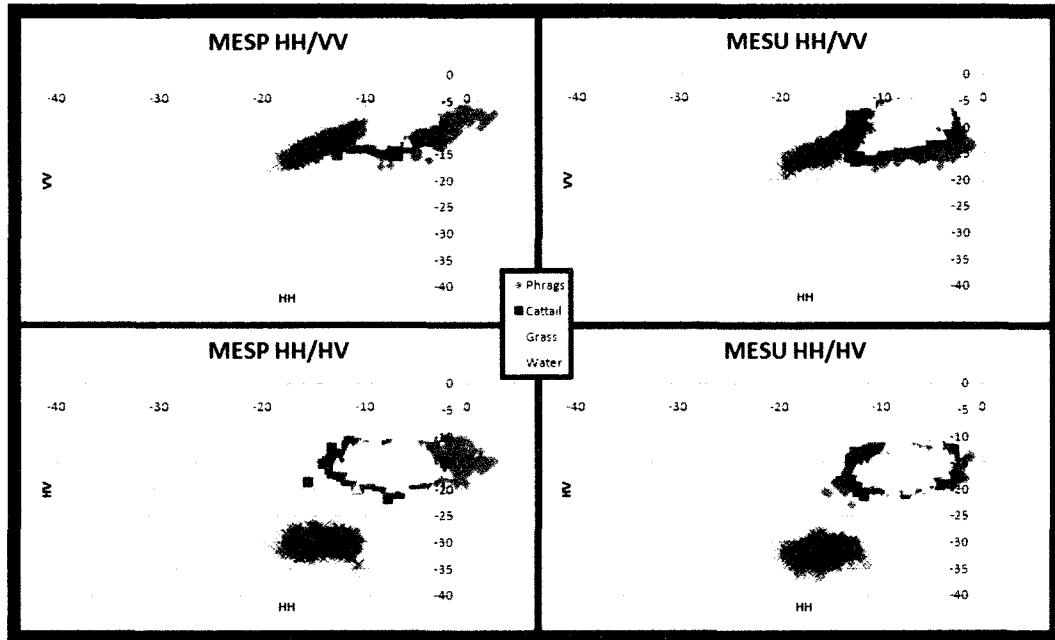


Figure 22: Scatter plots displaying the co-polarized (HH/VV) and cross-polarized (HH/HV) intensity ratios for the spring and summer quad-pol imagery at medium incidence angles.

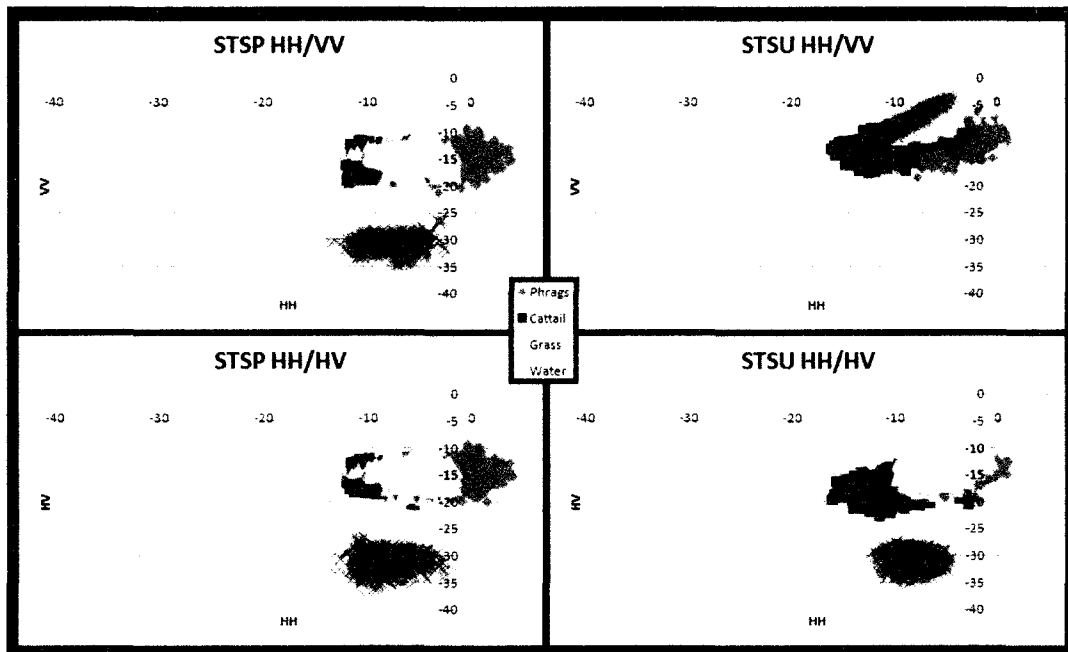


Figure 23: Scatter plots displaying the co-polarized (HH/VV) and cross-polarized (HH/HV) intensity ratios for the spring and summer quad-pol imagery at steep incidence angles.

Table 17: Average and standard deviation intensity values (dB) for the 3 vegetation classes and Water class for all of the polarimetric imagery.

Shallow Spring								
	HH		HV		VH		VV	
	Avg.	StDev.	Avg.	StDev.	Avg.	StDev.	Avg.	StDev.
<i>P. australis</i>	-5.467	1.938	-14.344	1.715	14.201	1.708	-8.488	1.948
Cattail	-8.337	1.900	-15.349	1.472	-15.415	1.524	-10.153	1.749
Grass	-8.265	2.049	-16.518	2.054	-16.530	2.086	-10.629	1.889
Water	-23.251	1.783	-32.278	1.539	-32.478	1.561	-22.372	1.801
Shallow Summer								
	HH		HV		VH		VV	
	Avg.	StDev.	Avg.	StDev.	Avg.	StDev.	Avg.	StDev.
<i>P. australis</i>	-7.996	2.489	-17.411	1.979	-17.418	1.972	-16.102	2.908
Cattail	-11.110	2.549	-18.490	2.478	-18.615	2.467	-15.651	3.089
Grass	-7.837	2.374	-14.700	1.975	-14.835	1.898	-8.778	2.144
Water	-21.363	1.916	-30.924	1.659	-31.107	1.601	-19.849	2.072
Medium Spring								
	HH		HV		VH		VV	
	Avg.	StDev.	Avg.	StDev.	Avg.	StDev.	Avg.	StDev.
<i>P. australis</i>	-4.600	2.758	-14.941	1.559	-14.895	1.606	-9.865	1.974
Cattail	-8.309	2.095	-15.554	1.675	-15.381	1.529	-10.608	1.758
Grass	-7.448	1.942	-14.955	1.638	-14.966	1.599	-8.263	1.754
Water	-14.384	1.959	-30.220	1.631	-30.407	1.642	-13.337	1.919
Medium Summer								
	HH		HV		VH		VV	
	Avg.	StDev.	Avg.	StDev.	Avg.	StDev.	Avg.	StDev.
<i>P. australis</i>	-6.936	2.531	-16.716	1.721	-16.891	1.689	-12.049	2.104
Cattail	-8.058	2.547	-16.121	1.911	-16.246	1.957	-10.984	2.114
Grass	-7.420	1.788	-15.612	1.620	-15.779	1.573	-8.889	1.980
Water	-15.868	1.890	-31.890	1.679	-31.461	1.413	-14.452	1.841
Steep Spring								
	HH		HV		VH		VV	
	Avg.	StDev.	Avg.	StDev.	Avg.	StDev.	Avg.	StDev.
<i>P. australis</i>	-1.701	2.263	-14.850	1.814	-7.507	2.063	-14.816	1.834
Cattail	-7.088	2.006	-15.044	1.670	-9.273	1.900	-14.914	1.648
Grass	-5.460	1.934	-14.640	1.753	-6.011	1.793	-14.653	1.732
Water	-7.752	2.283	-31.243	1.918	-7.274	2.329	-30.827	1.571
Steep Summer								
	HH		HV		VH		VV	
	Avg.	StDev.	Avg.	StDev.	Avg.	StDev.	Avg.	StDev.
<i>P. australis</i>	-5.808	3.033	-15.315	1.610	-15.459	1.702	-11.647	2.062
Cattail	-9.530	2.456	-17.036	1.894	-17.005	1.908	-11.351	2.058
Grass	-5.693	1.791	-14.072	1.629	-14.036	1.613	-6.409	1.912
Water	-8.230	1.770	-30.823	1.628	-30.507	1.799	-7.646	1.859

4.2.2 Polarimetric Plots & Pedestal Height

The co-polarized and cross-polarized polarimetric plots and class-specific pedestal heights highlight the distinct backscatter features which aid in distinguishing between the three vegetation classes and Water class (Table 18). All three vegetation classes were shown to display unique characteristics.

The pedestal heights indicated that the *P. australis* class produced the most depolarized component, most likely associated with rougher surface scattering and increased volume scattering, in all of the images except the shallow and steep incidence angle summer imagery where the Cattail class pedestal height was higher. On average, the Grass class produced the least amount of depolarization of the vegetation classes, except in the shallow and steep incidence angle spring imagery and shallow summer incidence angle imagery, while the Water class produced the least depolarized component overall.

Table 18: Co-polarized, pedestal heights for the 3 vegetation classes and Water class for the spring and summer seasons at shallow, medium and steep incidence angles.

Shallow Spring	Pedestal Height	Shallow Summer	Pedestal Height
<i>P. australis</i>	0.121	<i>P. australis</i>	0.027
Cattail	0.058	Cattail	0.062
Grass	0.077	Grass	0.039
Water	0.002	Water	0.002
Medium Spring	Pedestal Height	Medium Summer	Pedestal Height
<i>P. australis</i>	0.100	<i>P. australis</i>	0.070
Cattail	0.073	Cattail	0.056
Grass	0.061	Grass	0.053
Water	0.004	Water	0.003
Steep Spring	Pedestal Height	Steep Summer	Pedestal Height
<i>P. australis</i>	0.076	<i>P. australis</i>	0.070
Cattail	0.067	Cattail	0.079
Grass	0.069	Grass	0.050
Water	0.005	Water	0.003

The polarimetric plots associated with the *P. australis* class in the spring imagery (Figure 24) displayed a maximal response in the VV polarization of the co-polarized state. A decrease in VV backscatter at steeper incidence angles may be evidence of greater canopy penetration and attenuation by the vertically oriented plant elements.

In the spring, as the incidence angle steepened the pedestal height decreased, indicating that the signal is more polarized. This is likely a result of greater penetration and reduced numbers of bounces within the canopy, but possibly including double bounce scattering from the water-plant interface. The response in the HH polarization did not vary significantly across incidence angles. This indicates that the angle of incidence has little effect on the strength of the signal in the HH polarization.

In the summer imagery, the response in the VV polarization increases at steeper incidence angles. The density of the *P. australis* stands increases in the summer. An increase in VV response at these steeper angles suggests that greater penetration at steeper angles is providing increased interaction and scattering from this denser canopy. As in the spring imagery, the response in the HH polarization did not vary significantly across incidence angles. Depolarization was found to be lower at shallow incidence angles as evidenced by a slight lowering the pedestal heights. This is due to reduced number of bounces as scattering at shallow angles is mostly from the canopy surface.

The spring co-polarized polarimetric plots associated with the Cattail class (Figure 25) displayed a similar, but lower overall, maximum response in the VV state and a much higher HH response at all incidence angles. This is likely due to greater penetration at HH resulting in greater interaction of the radar wave with canopy as well as the soil and water. The pedestal height (Table 18) indicated that the amount of depolarization varied across incidence angles and seasons, but depolarization was found to be higher in the steeper incidence angle imagery when compared to the shallow incidence angle imagery. In both the spring and summer imagery, the response in the HH state increased with steepening incidence angles, likely as a result of the same increase in canopy, soil and water interaction.

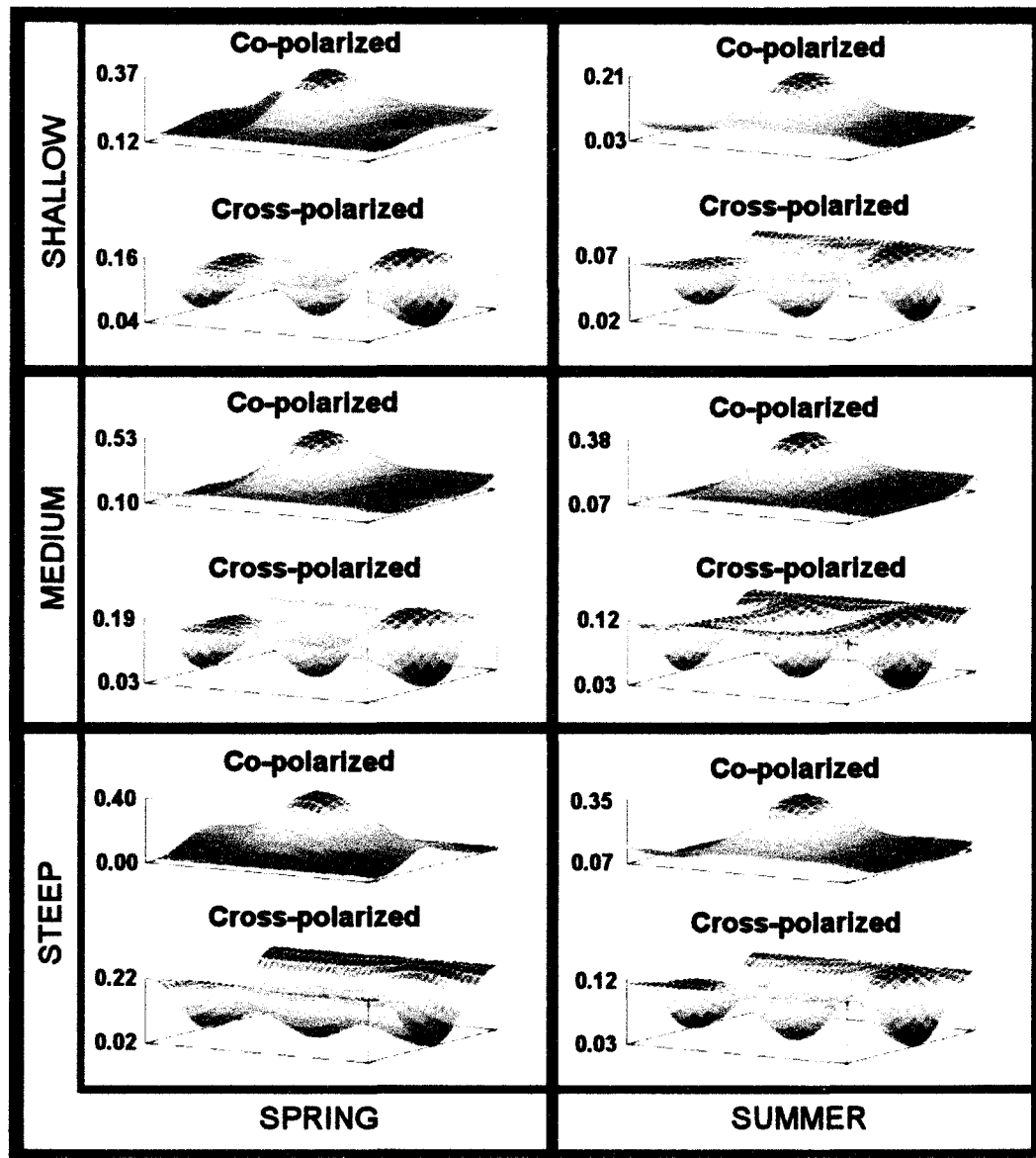


*Figure 24: Co-polarized and cross-polarized polarimetric plots showing the *P. australis* class during the spring and summer seasons at shallow, medium and steep incidence angles.*

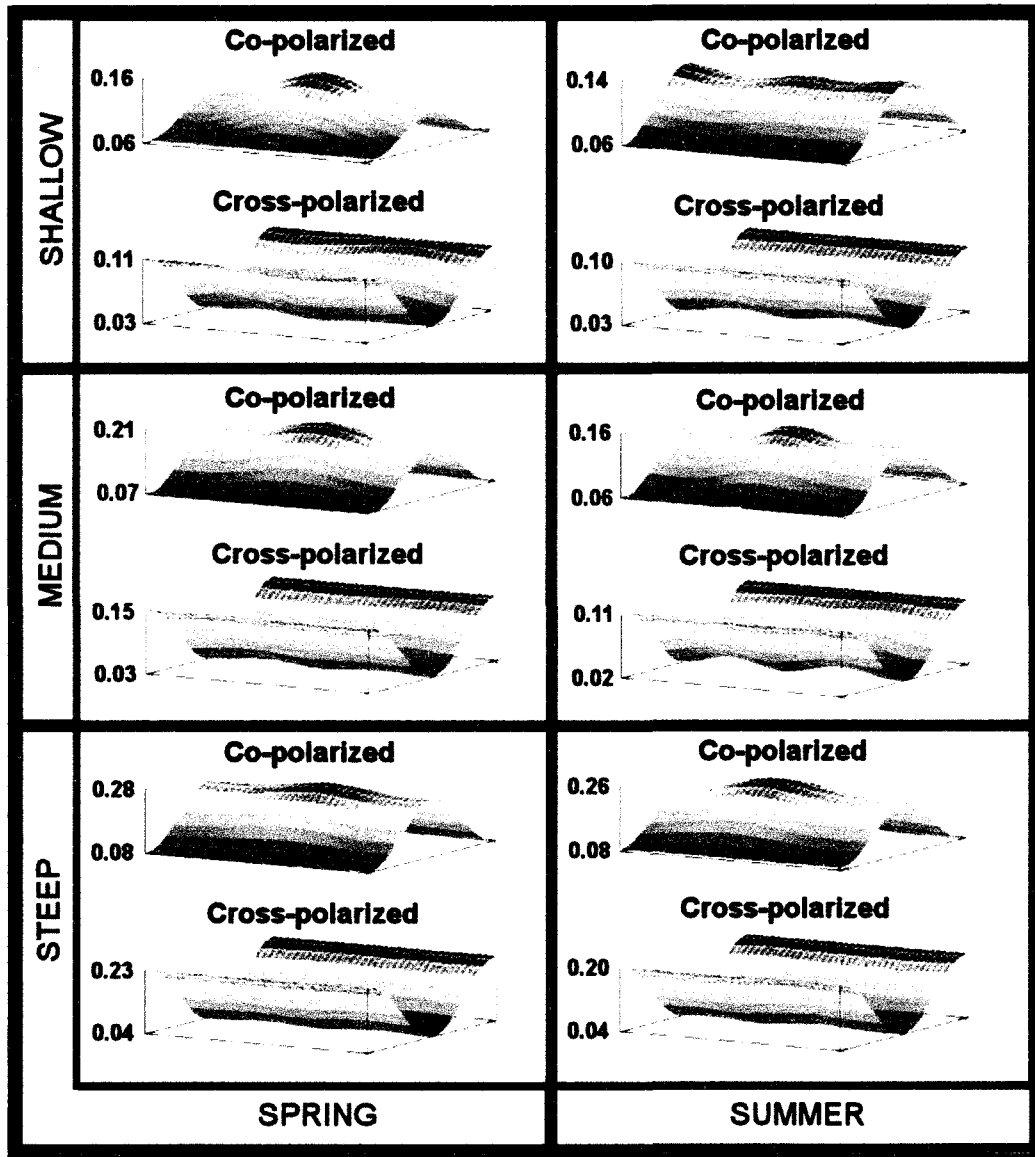


Figure 25: Co-polarized and cross-polarized polarimetric plots showing the Cattail class during the spring and summer seasons at shallow, medium and steep incidence angles.

The polarimetric plots associated with the Grass class (Figure 26) displayed a similar response to the *P. australis* class, but with lower average backscatter and a relatively more pronounced volume scattering component, highlighted by the higher response in the HH polarization. The volume scattering component increased as the incidence angle steepened, while the relative contribution of the surface scattering component was reduced, as indicated by the relative increase of the response in the HH state. The depolarization of the Grass class did not follow a significant pattern with varying incidence angle or across the two seasons. This is likely a result of the uniform coverage of the Grass class compared to that of the *P. australis* and Cattail classes where there are larger gaps among the plants which allow for different sources of scattering.

The polarimetric plots associated with the Water class (Figure 27) displayed low average backscatter as it is dominated by surface scattering away from the sensor. This is also shown in the relative levels of HH and VV returns, especially in the steeper incidence angle imagery. In addition to this, the pedestal height (Table 18) was very low at all incidence angles and during both seasons, indicating very little depolarization of the radar signal.

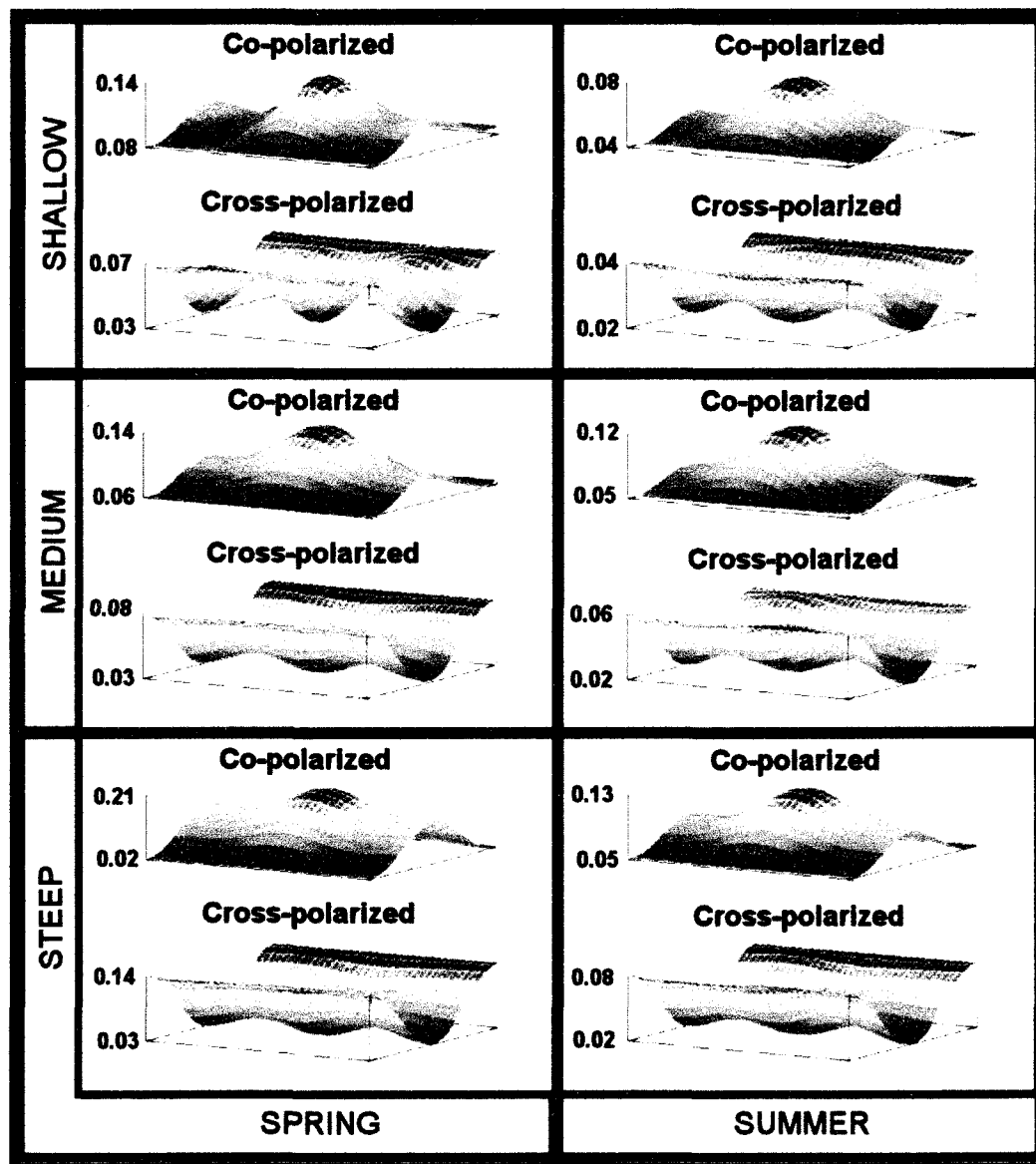


Figure 26: Co-polarized and cross-polarized polarimetric plots showing the Grass class during the spring and summer seasons at shallow, medium and steep incidence angles.

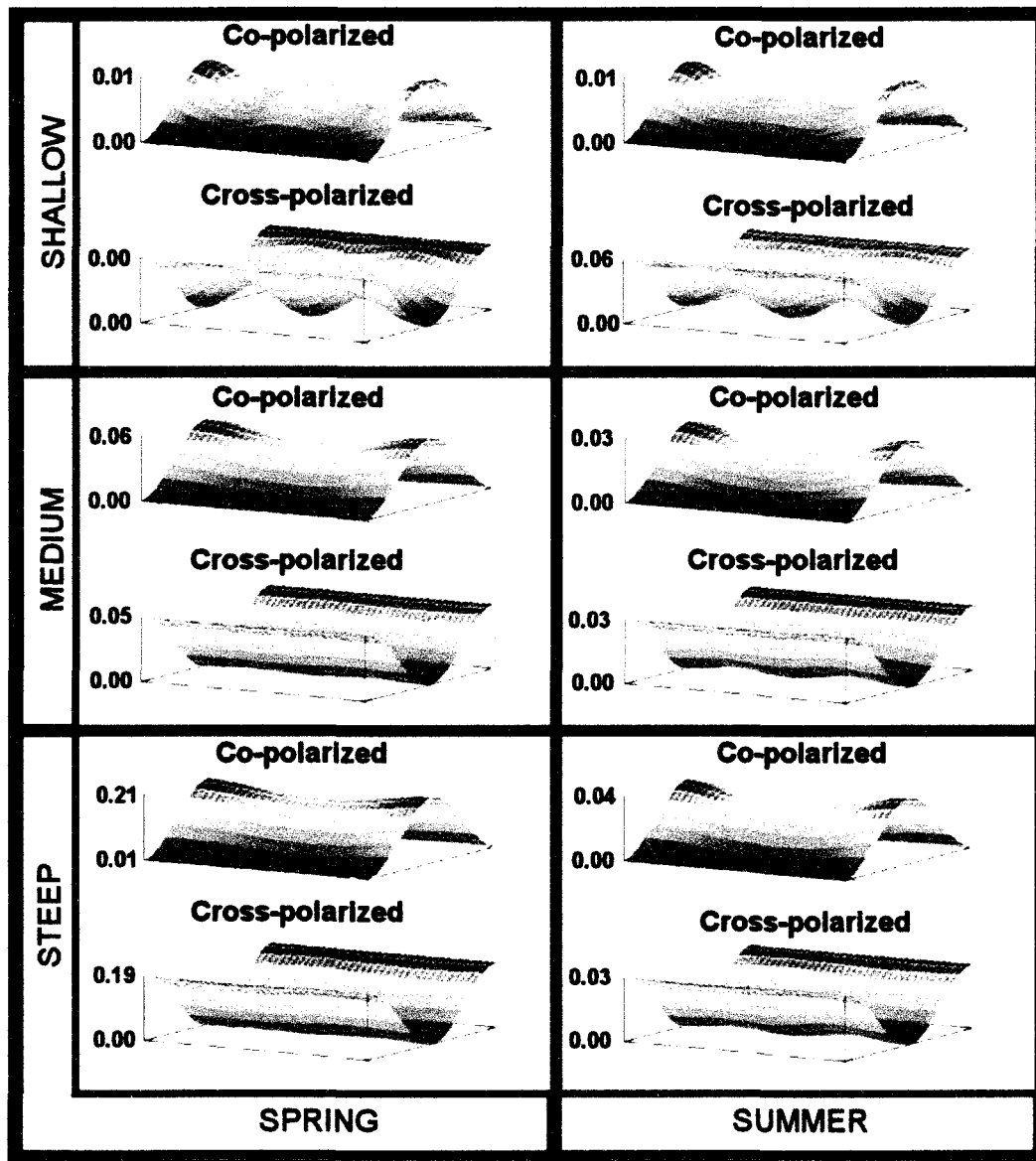


Figure 27: Co-polarized and cross-polarized polarimetric plots showing the Water class during the spring and summer seasons at shallow, medium and steep incidence angles.

4.2.3 Vegetation Class Discrimination Using Polarimetric Decomposition

4.2.3.1 Van Zyl Decomposition

The expected classes for the Van Zyl output, based on the type of scattering, were: *P. australis* (volume), Cattail (volume), Grass (volume), and Water (Surface). This was found to be true for all cases, except for the Grass class in the steep incidence angle spring imagery, where the dominant class was characterized by surface scattering as a result of vegetation penetration and water presence (Table 19). The dominant class percentage was calculated by dividing the number of pixels in the dominant class by the total number (750) of pixels. The dominant class percentage was low (36%) in this case. Water was best classified (as surface scattering) in the steep incidence angle imagery because, as the incidence angle became shallower, the dominant class percentage decreased as a result of wave action causing multiple scattering, which can be seen in Figure 28 (at 'A').

Table 19: Dominant Van Zyl classes, based on 750 pixel samples, for each of the 3 vegetation classes and Water class for all 6 polarimetric images. The total percentage of the dominant class in the 750 samples is included.

	<i>P. australis</i>	Cattail	Grass	Water
Shallow Spring				
Dominant Class	3	3	3	1
Percent (%)	82	64	54	84
Medium Spring				
Dominant Class	3	3	3	1
Percent (%)	74	67	59	94
Steep Spring				
Dominant Class	3	3	1	1
Percent (%)	64	68	36	100
Shallow Summer				
Dominant Class	3	3	3	1
Percent (%)	86	72	74	82
Medium Summer				
Dominant Class	3	3	3	1
Percent (%)	76	68	72	93
Steep Summer				
Dominant Class	3	3	3	1
Percent (%)	81	76	79	100
Legend				
Surface (odd)	1			
Double-Bounce (even)	2			
Volume	3			
Non-Classifiable	4			

The dominant class percentage for all vegetation classes did not vary by more than 18% in all of the summer imagery, with the lowest class percentage being 68% for the Cattail class in the medium incidence angle summer imagery. This can be

characterized as a good representation of volume scattering presence for all classes given the simplistic (single scatterer) analysis the Van Zyl decomposition presents.

In the spring imagery the *P. australis* class dominance percentage decreased as incidence angle increased, while the Cattail and Grass classes had about the same dominance percentage at all incidence angles, aside from the mis-classification of Grass as a dominant surface scatterer in the steep incidence angle spring imagery. The structural spacing (percent cover) of the *P. australis* class is significantly lower in the spring allowing more of the incident radar wave to interact with the surface water.

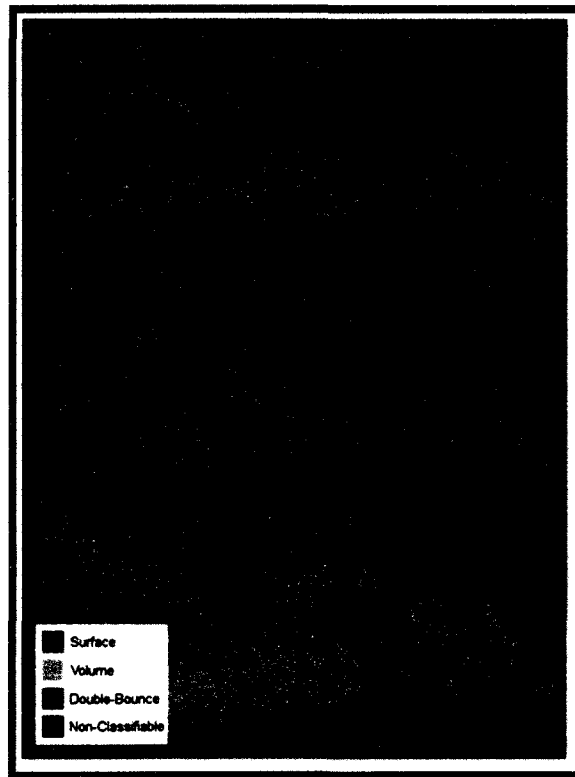


Figure 28: Spring season Van Zyl decomposition maps for the Long Point and Big Creek study areas. Top to bottom: steep, medium, shallow incidence angles, respectively. 'A' shows increased wave interaction and multiple scattering.

Overall, the Van Zyl decomposition cannot be used to separate vegetation classes, but it can provide some information with regards to the dominant scattering type at a given location. This method can be used as a very simple means of identifying anomalies, such as vegetation dominated by surface scattering, in an image.

4.2.3.2 Freeman-Durden Decomposition

As was expected, in the spring and summer imagery the volume scattering component was highest for the vegetation classes, while the surface scattering component was highest for the Water class, with one exception; the surface scattering component was highest for the Grass class in the steep incidence angle spring imagery (Table 20) as found for the Van Zyl decomposition.

Table 20: Average scattering composition for the 3 vegetation classes and Water for each of the 6 polarimetric images derived from the Freeman-Durden decomposition.

	<i>P. australis</i>	Cattail	Grass	Water
Shallow Spring				
Surface	0.007	0.028	0.101	0.007
Double-Bounce	0.168	0.074	0.025	0.002
Volume	0.320	0.243	0.217	0.003
Medium Spring				
Surface	0.012	0.063	0.157	0.085
Double-Bounce	0.212	0.041	0.017	0.002
Volume	0.273	0.239	0.269	0.006
Steep Spring				
Surface	0.248	0.115	0.342	0.398
Double-Bounce	0.265	0.048	0.026	0.006
Volume	0.296	0.269	0.293	0.005
Shallow Summer				
Surface	0.034	0.024	0.098	0.015
Double-Bounce	0.095	0.028	0.041	0.001
Volume	0.256	0.127	0.288	0.004
Medium Summer				
Surface	0.091	0.083	0.152	0.063
Double-Bounce	0.098	0.053	0.024	0.003
Volume	0.178	0.115	0.228	0.003
Steep Summer				
Surface	0.105	0.073	0.270	0.344
Double-Bounce	0.147	0.022	0.030	0.044
Volume	0.245	0.137	0.332	0.005

For the *P. australis* class in the spring imagery, volume scattering remained fairly consistent while surface and double-bounce scattering increased steadily with increasing steepness. The same trend was observed in the summer imagery, but to a lesser degree. The mean values for *P. australis* surface scattering in the spring increased from 0.007 (shallow) to 0.248 (steep), but in the summer the values increased from 0.034 (shallow) to only 0.105 (steep). Since there is significantly more vegetation cover in summer, there is less interaction with surface water, even at a steep incidence angle, since the C-band radar wave would not penetrate most of the vegetation canopy. An increase in double-bounce scattering in both seasons does, however, suggest that at least some penetration to the surface water is occurring. The above findings are similar to those derived from the Van Zyl decomposition, but they do provide more insight into why the dominant class percentage (volume) decreases as incidence angle increases in the Van Zyl dataset.

The Cattail class showed consistent levels of volume scattering in both seasons, but an increase in surface scattering in the steep incidence angle spring imagery as a result of surface water interaction. Otherwise, the parameters remained fairly constant.

The Grass class also showed consistent levels of volume scattering throughout both seasons, however, the average levels were slightly higher in the steep incidence angle imagery in both seasons. Surface scattering increased in both seasons as incidence angles steepened, which indicates that more surface water interaction occurred as the angles increased. Overall, Grass had very little double-bounce scattering, which makes

sense since it is very short and does not often stand completely erect, increasing the chance that the radar signal will scatter multiple times within the vegetation, or simply reflect off the top when the surface is flattened or when surface water is present and vegetation is sparser.

As expected, surface scattering was found to be the main component of the Water class. In many cases surface scattering values were noticeably separable from the volume and double-bounce components in the shallow incidence angle imagery; however, the steep incidence angle imagery shows a dominant surface component. For example, in the spring imagery the surface scattering component increases from 0.007 (shallow) to 0.398 (steep). Results were found to be similar for the summer imagery, except in the case where double-bounce scattering was found to increase in the steep incidence angle summer imagery. This can be explained by wave interaction with emergent vegetation in some of the inland Water sites. Overall, the above findings indicate that the Water class is more poorly characterized in the shallow incidence angle imagery, mostly as a result of wave interaction at the water's surface. Figure 29 displays spring Freeman-Durden decomposition maps for the study area. More surface scattering can be seen through the shoreline vegetation in the steep incidence angle imagery (vegetation appears more translucent) at 'A'.

The information gained from the Freeman-Durden decomposition was found to be consistent with the class characteristics derived from the polarimetric plots. Once a good understanding of the three vegetation and Water class characteristics in the

imagery was obtained, it became possible to delve further into the data using more complex decomposition techniques with confidence. The output of the Freeman-Durden decomposition could be input into a simple classifier based on trends that were evident as described above, but for the purpose of this research, only the best decomposition results were used to map *P. australis*.

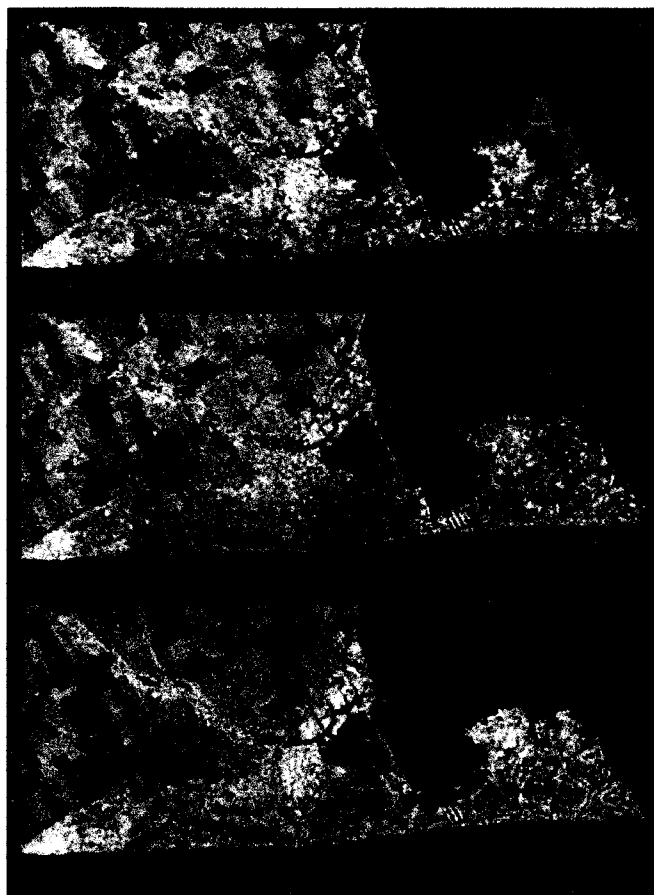


Figure 29: Spring season Freeman-Durden decomposition maps for the Long Point and Big Creek study areas. Top to bottom: steep, medium, shallow incidence angles, respectively. 'A' displays an increase in surface scattering. Red represents double-bounce scattering, green represents volume scattering, and blue represents surface scattering.

4.2.3.3 Cloude-Pottier Decomposition

Using the Cloude-Pottier decomposition, degree of incoherence, represented by Entropy (H), decreased as incidence angle increased for all 3 vegetation classes and the Water class in the spring imagery (Table 21). The *P. australis* class had the largest decrease in incoherence; 0.814 to 0.561 (Figure 30). In the summer imagery the Grass and Water classes were the only ones with a decrease in incoherence across incidence angles meaning that an increase in wave interaction with surface water contributes to an increase in signal coherence.

The average Anisotropy (A) in both the spring and summer imagery remained fairly constant for all 3 vegetation classes; between ~0.200 and ~0.400, indicating that the amount of mixing between the second and third scattering mechanisms was fairly equal. This is to be expected as these values are averaged across 750 samples, however, the maximum Anisotropy did not generally exceed 0.600 for any of the vegetation classes. It did, however, exceed 0.600 in both seasons for the Water class, indicating that the second most dominant scattering mechanism is often much stronger than the third.

Table 21: Cloude-Pottier parameters based on 750 pixel samples for each of the 3 vegetation classes and Water class for all 6 polarimetric images. The numbers represent the mean values for each sample.

	<i>P. australis</i>	Cattail	Grass	Water
Shallow Spring				
Entropy (H)	0.814	0.884	0.764	0.643
Anisotropy (A)	0.401	0.327	0.275	0.637
Alpha	44.449	44.701	26.937	14.277
Beta	74.121	69.838	65.651	69.488
Medium Spring				
Entropy (H)	0.723	0.877	0.774	0.212
Anisotropy (A)	0.249	0.195	0.145	0.417
Alpha	43.452	31.869	18.135	5.240
Beta	82.671	72.596	55.824	77.283
Steep Spring				
Entropy (H)	0.561	0.820	0.634	0.105
Anisotropy (A)	0.410	0.284	0.290	0.723
Alpha	35.408	29.301	15.025	3.528
Beta	82.393	69.146	50.522	74.623
Shallow Summer				
Entropy (H)	0.616	0.821	0.824	0.478
Anisotropy (A)	0.330	0.259	0.261	0.410
Alpha	47.188	38.953	28.491	11.910
Beta	69.063	62.158	58.769	67.652
Medium Summer				
Entropy (H)	0.694	0.812	0.756	0.251
Anisotropy (A)	0.356	0.310	0.264	0.644
Alpha	38.704	35.456	22.011	6.872
Beta	71.069	69.843	62.379	75.775
Steep Summer				
Entropy (H)	0.691	0.798	0.703	0.091
Anisotropy (A)	0.276	0.276	0.280	0.638
Alpha	44.223	26.583	18.067	3.360
Beta	73.453	58.377	49.760	75.626



Figure 30: Spring season Cloude-Pottier decomposition maps representing Entropy (H) for the Long Point and Big Creek study areas. Top to bottom: steep, medium, shallow incidence angles, respectively.

The average Alpha (α) value for all of the vegetation classes was between 0° and 45°, indicating that volume scattering was the dominant scatterer type for these classes in both the spring and summer imagery. The *P. australis* class generally had values close to 45°, indicating contributions from surface scattering and possibly some double-bounce scattering. In the spring imagery the Alpha value decreased as incidence angle increased meaning that there was a higher amount of surface scattering at shallower angles. Aside from the shallow incidence angle spring imagery, the Alpha value decreased across the 4 classes with *P. australis* being the highest, followed by Cattail, Grass, and Water, respectively. As would be expected, the Water class had the lowest average Alpha values in all of the imagery, but did not reach 0 as there was always some interference from multiple scatterers across the samples. Figure 31 displays spring season Cloude-Pottier decomposition maps representing Alpha (α) angles for the Long Point and Big Creek study areas.

Between the shallow and steep incidence angles in both seasons the values for Beta increased for *P. australis* and the Water class, decreased for the Grass class, and stayed about the same for the Cattail class. While there were measurable differences in Beta across incidence angles, the amount of change was found to be minimal and therefore would not represent a good discriminator for vegetation types. Across the two seasons there was a slight decrease in the values for Beta in all cases, except for the Grass class at medium incidence angles where the value for Beta was found to increase.

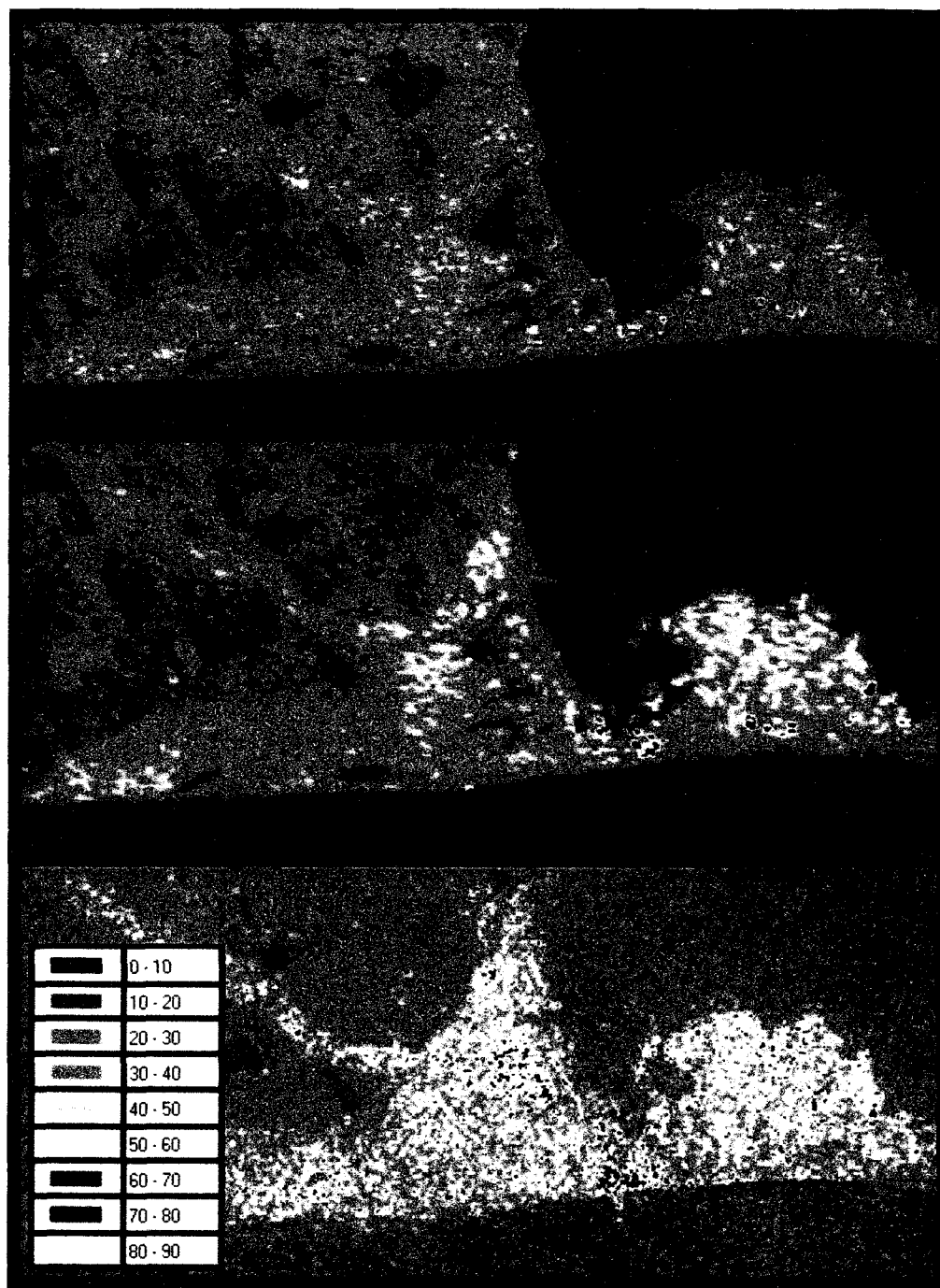


Figure 31: Spring season Cloude-Pottier decomposition maps representing Alpha (α) angles for the Long Point and Big Creek study areas. Top to bottom: steep, medium, shallow incidence angles, respectively.

4.2.3.4 Touzi Decomposition

The Touzi decomposition with a 7x7 window was found to be the most capable of separating vegetation classes across the imagery as the 5x5 window and 11x11 window sizes were found to be too constrained and too broad, respectively. Table 22 displays the mean values for the Touzi parameters based on 750 pixel samples for each of the vegetation classes and Water class for all 6 of the polarimetric images. The parameters from the Touzi decomposition are discussed in order of ease of interpretability.

The Alpha_S parameter (Figure 32) displayed a step-like pattern where the values were highest for *P. australis*, second highest for Cattail, third highest for Grass, and lowest for Water, indicating the presence of multiple scattering, particularly for *P. australis*. This trend was consistent throughout all of the imagery. These values increased as incidence angle decreased in both the spring and summer imagery except for *P. australis* in summer.

Table 22: Touzi parameters based on 750 pixel samples for each of the 3 vegetation classes and Water class for all 6 polarimetric images. The numbers represent the mean values for the total sample.

	<i>P. australis</i>	Cattail	Grass	Water
Shallow Spring				
Psi Angle	-0.056	-0.036	-0.038	0.020
Dominant Eigenvalue	0.666	0.606	0.690	0.750
Alpha_S	0.767	0.692	0.356	0.253
Phase	-0.274	0.178	-0.157	0.100
Tau Angle (Helicity)	0.056	0.024	-0.009	-0.007
Medium Spring				
Psi Angle	-0.019	0.000	0.032	0.011
Dominant Eigenvalue	0.721	0.652	0.720	0.950
Alpha_S	0.696	0.498	0.221	0.085
Phase	-0.228	-0.054	-0.030	0.168
Tau Angle (Helicity)	0.021	0.006	0.002	-0.003
Steep Spring				
Psi Angle	-0.011	0.006	0.098	-0.003
Dominant Eigenvalue	0.823	0.651	0.780	0.979
Alpha_S	0.560	0.465	0.164	0.055
Phase	-0.422	-0.002	0.254	0.601
Tau Angle (Helicity)	-0.019	0.006	0.004	0.000
Shallow Summer				
Psi Angle	0.107	0.045	-0.028	-0.006
Dominant Eigenvalue	0.782	0.653	0.662	0.846
Alpha_S	0.749	0.596	0.333	0.167
Phase	-0.099	0.079	-0.002	-0.025
Tau Angle (Helicity)	-0.107	-0.029	-0.002	0.003
Medium Summer				
Psi Angle	-0.074	-0.014	0.002	-0.001
Dominant Eigenvalue	0.748	0.657	0.697	0.938
Alpha_S	0.696	0.536	0.241	0.116
Phase	0.099	0.188	-0.235	0.149
Tau Angle (Helicity)	0.048	0.008	-0.001	0.002
Steep Summer				
Psi Angle	0.089	0.050	-0.068	0.026
Dominant Eigenvalue	0.740	0.671	0.730	0.981
Alpha_S	0.727	0.446	0.198	0.053
Phase	-0.120	0.130	0.009	0.454
Tau Angle (Helicity)	-0.092	0.012	-0.004	0.000

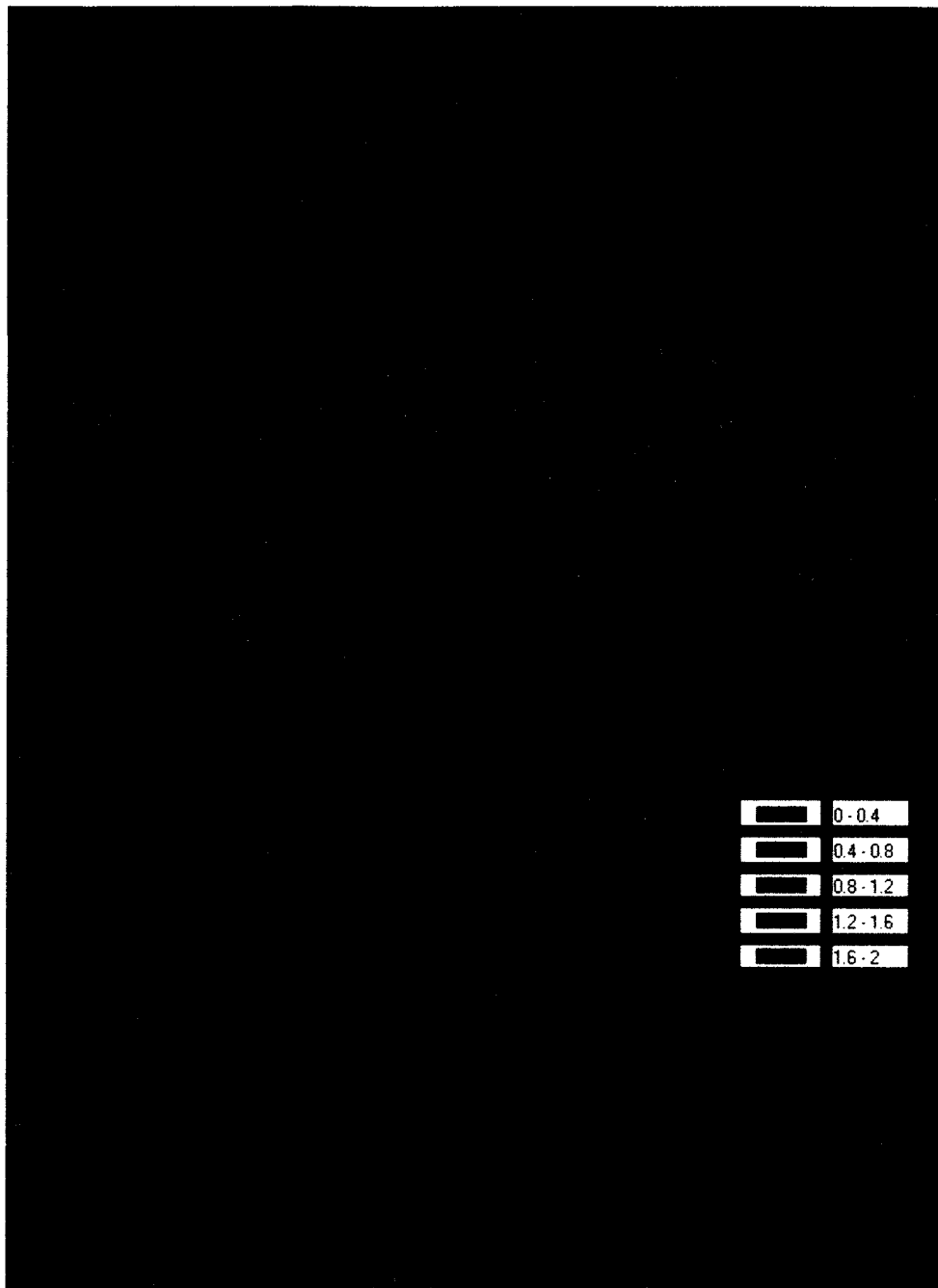


Figure 32: Spring season Touzi decomposition images representing the Alpha_S parameter for the Long Point and Big Creek study areas. Top to bottom: steep, medium, shallow incidence angles, respectively. A decrease in incidence angle increases homogeneity of the Alpha_S parameter over vegetation.

The Phase parameter (Figure 33) was shown to be most useful for identifying the *P. australis* class in the spring imagery at a steep incidence angle where its value was highly negative (~ -0.4 radians). In the same image, the Cattail (~ 0), Grass (~ 0.2), and Water (~ 0.6) classes also showed distinct average values. As the incidence angle became shallower the gap between these values decreased. In the summer imagery the values for the Phase parameter did not show any recognizable patterns. These findings indicate that *P. australis* produces a complex signal, possibly due to the multiple scattering types, which was exemplified by the analysis of the Alpha_S parameter. The Helicity parameter showed some variation among the classes, but at a smaller scale than the other parameters. For the vegetation classes, in the shallow spring imagery the Helicity was highest for *P. australis* (0.056) and lower for Cattail (0.024) and Grass (-0.009). It is possible that these differences could be used to classify *P. australis* vs. Other vegetation classes in certain images. Likewise, Helicity decreased for *P. australis* as the incidence angle steepened in the spring imagery. These patterns are important and are taken into consideration in the separability analysis, which is discussed later.

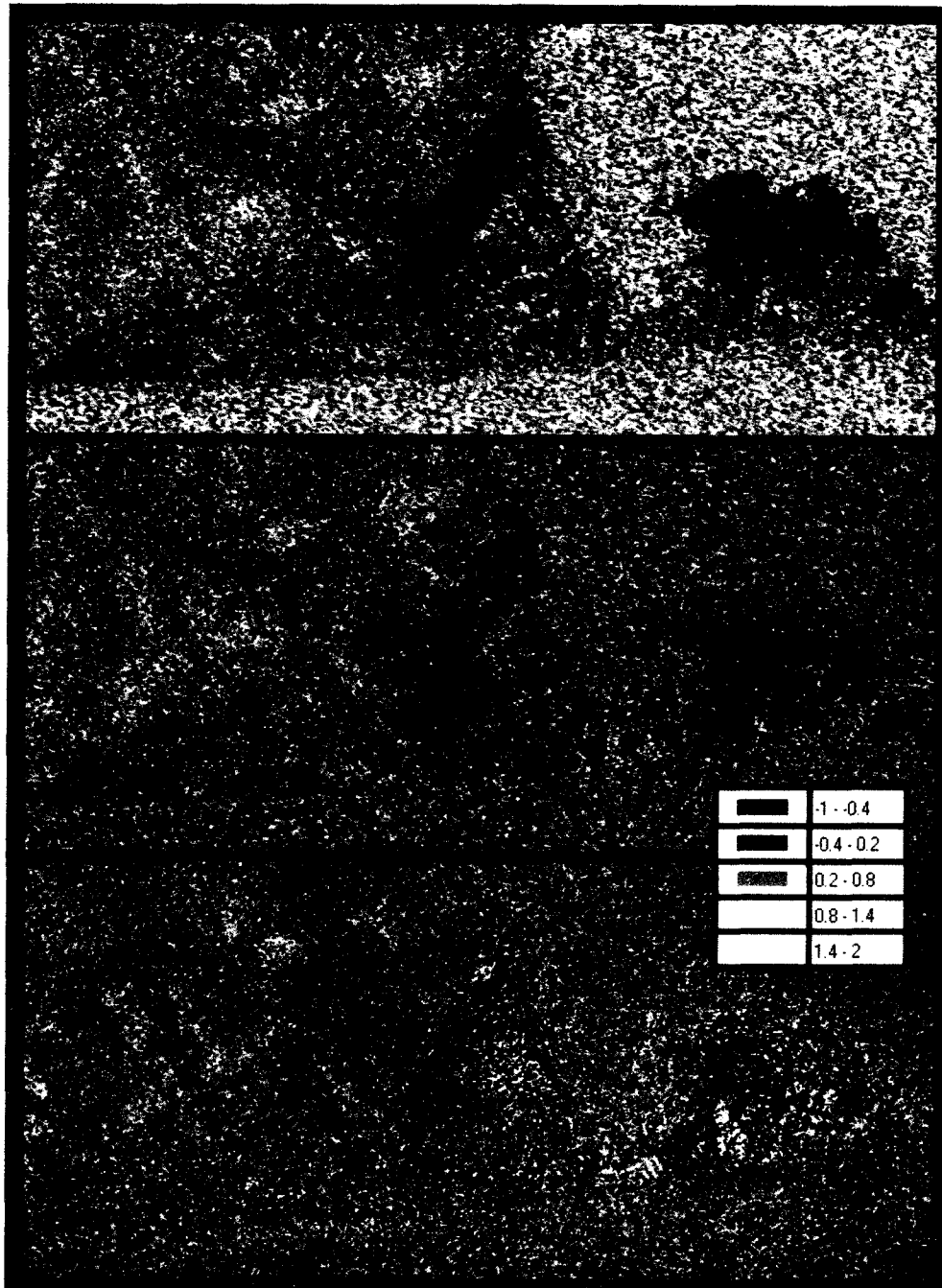


Figure 33: Spring season Touzi decomposition maps representing the Touzi_Phase parameter for the Long Point and Big Creek study areas. Top down: steep, medium, shallow incidence angles. A steep incidence angle displays more heterogeneity over the study area.

In general, the Psi angle and Dominant Eigenvalue were found to poorly characterize individual classes within all of the imagery as they did not display any highly significant pattern or distinct features (very high or low values). There were a few features to note, such as the decrease in Dominant Eigenvalue across the classes: Water (highest), *P. australis*, Grass and then Cattail (lowest), except in the shallow incidence angle spring imagery. The mean and standard deviations of these values often overlapped, so while the order could be used in a classifier, the output may not represent a high degree of overall accuracy. Table 22 and Figures 34 and 35 display this information.

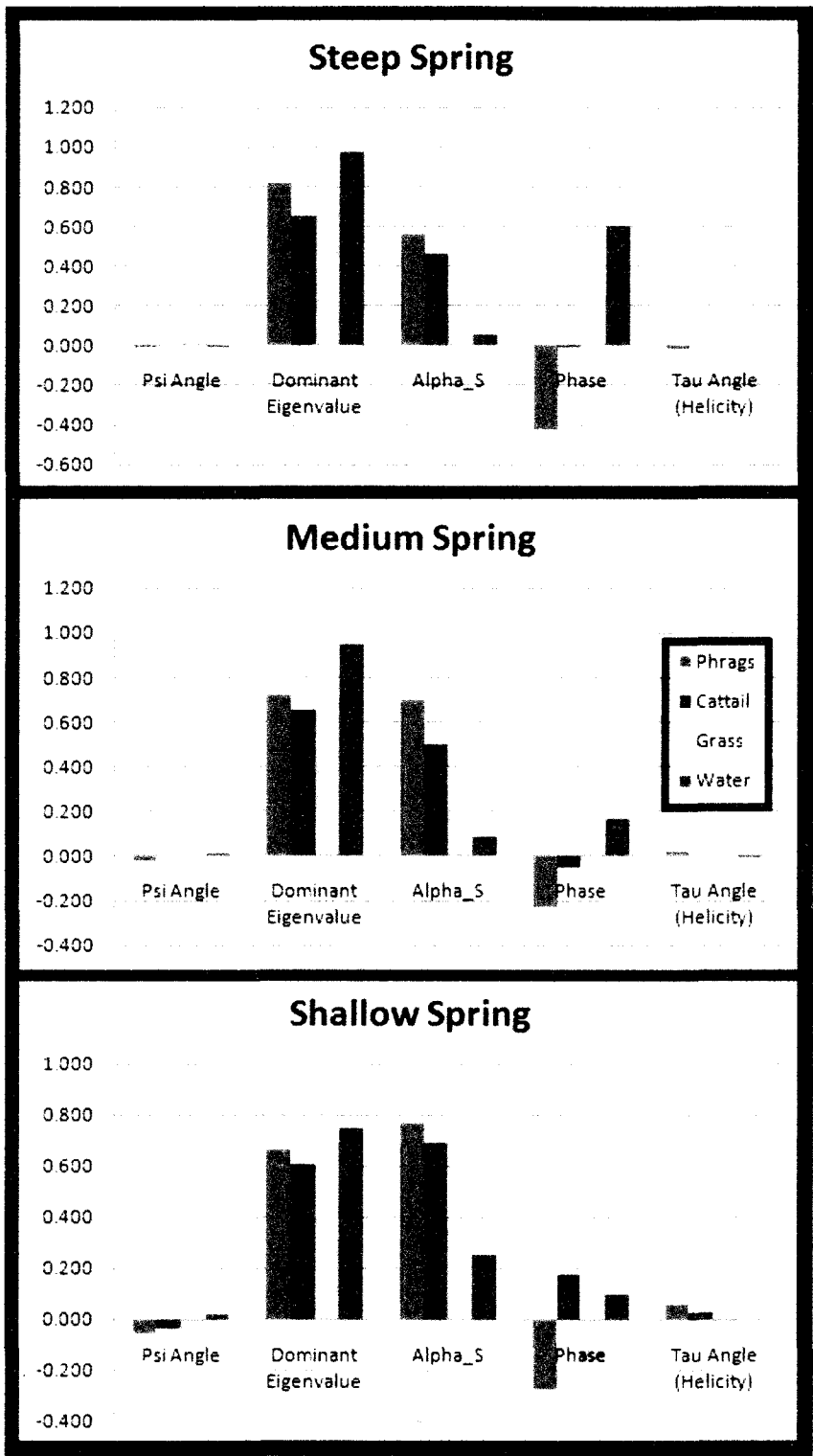


Figure 34: Spring season Touzi decomposition parameters at 3 incidence angles.

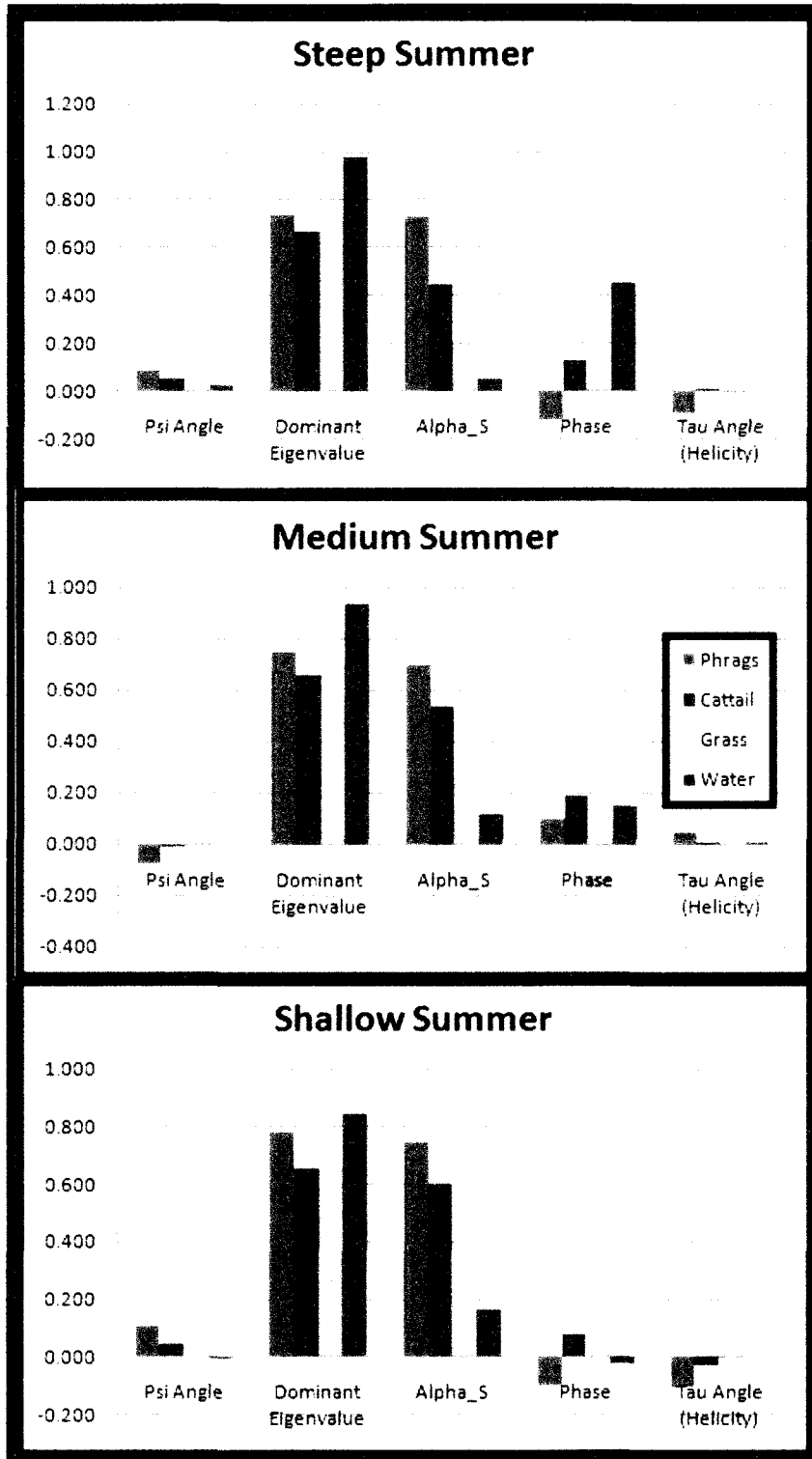


Figure 35: Summer season Touzi decomposition parameters at 3 incidence angles.

4.3 Separability Analysis of Polarimetric Decompositions

The average separability (within-class and cross-class) for each of the 18 image combinations was calculated and is presented in Table 23. The majority of image combinations resulted in “poor” or “very poor” average separability, which indicated that these images were homogeneous. All of the images that were classified as either “good” or “very good” contain only spring imagery, indicating that the addition of the summer season imagery decreases the average separability. This makes sense since the analysis of the polarimetric decompositions showed much less distinction between classes in the summer imagery. The best separability was achieved using only the Touzi decomposition, but the Cloude-Pottier decomposition and combination of the Touzi and Cloude-Pottier decompositions also produced high average separability values.

Table 23: Average BD separability results for the 3 image combinations.

Image Composition	Average Separability	Minimum Separability	Maximum Separability	Separability Class
Touzi_Spring	1.9	1.5	2.0	Very Good
Touzi_CP_Spring	1.9	1.4	2.0	Very Good
CP_Spring	1.8	1.4	2.0	Good
Touzi_Filtered_Spring	1.8	1.2	2.0	Good
CP_Filtered_Spring	1.8	1.2	2.0	Good
Spring_Filtered	1.7	1.2	2.0	Good
All_Touzi	1.6	0.9	2.0	Poor
All_CP	1.6	0.8	2.0	Poor
Touzi_Filtered	1.5	0.3	2.0	Poor
CP_Filtered	1.3	0.3	2.0	Poor
Touzi_CP	1.2	0.8	2.0	Poor
Touzi_Summer	1.0	0.9	1.8	Poor
Touzi_CP_Summer	0.9	0.8	1.8	Very Poor
CP_Summer	0.9	0.8	1.7	Very Poor
Touzi_Filtered_Summer	0.8	0.3	1.7	Very Poor
CP_Filtered_Summer	0.8	0.3	1.7	Very Poor
All_Radar_Filtered	0.8	0.3	1.7	Very Poor
Summer_Filtered	0.6	0.3	1.7	Very Poor

4.3.1 Improving Separability through Image Reduction

Since the spring imagery with decompositions applied produced the highest average separability the next factor to test was incidence angle. The Touzi and Cloude-Pottier decompositions were broken down further in order to test separability on single spring image sets. The Touzi images each contained 5 channels, while the Cloude-Pottier images contained 4. Table 24 displays the separability results for the single images.

Table 24: Average BD separability results for single decomposed spring imagery at varying incidence angles.

Image Composition	Average Separability	Minimum Separability	Maximum Separability	Separability Class
CP_Steep	1.9	1.7	2.0	Very Good
Touzi_Steep	1.9	1.6	2.0	Very Good
CP_Shallow	1.7	0.9	2.0	Good
Touzi_Medium	1.7	1.5	2.0	Good
Touzi_Shallow	1.7	0.9	1.9	Good
CP_Medium	1.6	1.1	1.9	Poor

As was expected, based on the previous examination of specific decompositions, the imagery acquired at a steep incidence angle produced the best separability results. All of the shallow and some of the medium incidence angle imagery had previously shown high levels of confusion due to the lack of vegetation penetration (related to water detection/interaction) and inability of the shallow/medium imagery to capture structural differences such as vegetation height. This is most visible in the Van Zyl decomposition imagery where the volume scattering component saturates the imagery at shallow incidence angles.

4.3.2 Separability of *P. australis* vs. Other Samples

The above results show that spring imagery acquired at a steep incidence angle produces the highest average separability values when either the Touzi or Cloude-Pottier decomposition is applied. However, since the above separability analyses included within- and between-class samples, these results do not show whether separability only between classes (*P. australis* vs. Other) is high. The overall between-class separability is shown in Table 25. The Touzi decomposition applied to a steep incidence angle image produced the best cross-class separability and is therefore considered the optimal method for discriminating *P. australis* from other vegetation.

Table 25: Overall separability between *P. australis* and the Other class for single images, representing varying incidence angles, with decompositions applied.

Image Composition	Overall Separability
Touzi_Steep	1.816
CP_Steep	1.756
CP_Shallow	1.323
Touzi_Medium	1.211
Touzi_Shallow	0.909
CP_Medium	0.810

4.3.3 Combining Decomposition Parameters

Since the Touzi and Cloude-Pottier decompositions applied to the spring imagery produced similar levels of between-class separability it was possible that combining

specific channels (decomposition parameters) could produce even higher separability. Based on the in-depth analysis of individual decompositions in the previous sections, several parameters were selected as input into a further separability analysis. From the Touzi decomposition, Alpha_S, Phase, Helicity and Dominant Eigenvalue were selected, and from the Cloude-Pottier decomposition, Entropy, Anisotropy and Alpha were selected. A simple pair-wise Pearson correlation was applied to all parameters in order to ensure that they were not highly correlated before being input into the separability analysis. These seven parameters derived from the steep incidence angle spring imagery were input as channels into several separability analyses. All possible combinations of these channels, utilizing anywhere from 1 – 7 at a time, were assessed. Table 26 displays the three best results.

Table 26: Best three results from the permutative channel separability analysis for P. Australis vs. the Other class, using the steep incidence angle spring imagery.

Channel Combinations	Overall Separability
Alpha_S, Phase, Entropy	1.867
Alpha_S, Phase	1.863
Alpha_S, Phase, Entropy, anisotropy	1.821

The highest between-class separability was achieved using only 3 channels from the Touzi and Cloude-Pottier decompositions, Alpha_S and Phase from Touzi and Entropy from Cloude-Pottier. The addition of Entropy only increased separability by 0.004. The addition of other Touzi or Cloude-Pottier parameters reduced separability. Since the addition of Entropy as a parameter did not significantly increase separability, only the two primary Touzi parameters are discussed for the remainder of the analysis.

4.3.4 Examination of Physical and Textural Characteristics of *P. australis*

The average Touzi parameters found to be most useful in identifying *P. australis* (Phase and Alpha_S) were examined for the three (of 10) most separable samples from the separability analysis (Table 27), which was only concerned with cross-class separability (*P. australis* vs. Other). The three least separable cross-class samples from the separability analysis are shown in Table 28.

The transect lengths in these cases are not as informative as those found in the Big Creek study area where the patches were all circular and relatively small. In the Long Point study area transects could not always be completed through the entire “patch” since they were much larger and often extended into a very saturated coastal area that was not possible to traverse. There was a marked difference between the water levels in both the spring and summer imagery for the three most and three least separable patches. The water levels for the three least separable patches were significantly lower, especially in the summer when there was no surface water present at all for two patches. This is in contrast to the least identifiable patches in the single-polarized analysis that had a significant amount of surface water. The least separable patches in the single-polarized analysis also had low percent cover, which is not true of the least separable patches in the quad-pol imagery. This could have contributed to the fact that the summer imagery was found to have very poor separability overall. The height and percent cover for all patches in the study area were found to be similar.

Table 27: Physical and average Touzi decomposition parameters for the 3 most separable samples derived from the quad-polarized radar imagery.

	Transect Length (m)	Average Water Depth (cm)			Dominant Height (m)	Maximum Height (m)	Percent (%) Cover	Average Phase	Average Alpha_S
		Spring	Summer	Average					
Patch 4	100+	20	10	10	4.5	5	85	-4.45	0.57
Patch 6	100+	20	10	10	5	5	80	-3.81	0.38
Patch 9	80	25	15	15	4.5	5	90	-4.01	0.47

Table 28: Physical and average Touzi decomposition parameters for the 3 least separable samples derived from the quad-polarized radar imagery.

	Transect Length (m)	Average Water Depth (cm)			Dominant Height (m)	Maximum Height (m)	Percent (%) Cover	Average Phase	Average Alpha_S
		Spring	Summer	Average					
Patch 1	80	5	0	0	5	5	90	-0.01	0.16
Patch 3	100+	5	0	0	4.5	4.5	70	-2.94	0.25
Patch 7	50	10	5	5	4.5	5	85	-0.11	0.31

An examination of the field data showed that the least separable patches were found inland, whereas the three most separable patches were on a coastline. In addition to this, the inland patches of *P. australis* were generally much smaller (<150m x 150m) than the coastal patches which were often several hundred metres across. The lack of surface water and location of the inland patches could explain why they are not as separable from the other vegetation types in the study area.

This examination of the field variables was repeated again on 10 randomly selected field samples in order to determine if similar results could be obtained using another set of data. Table 29 displays the average and standard deviation of the Touzi parameters for the steep incidence angle, quad-polarized radar image obtained from averaging the 6 most separable samples.

Table 29: Average, 1 standard deviation, and 2 standard deviation statistics for the Touzi parameters derived from the steep, quad-polarized radar imagery.

	Average Phase	Average Alpha_S
Average	-4.13	0.48
1 StDev (68%)	0.68	0.11
2 StDev (95%)	1.36	0.22

4.3.5 Modelling and Mapping *P. australis* Distribution

As in the single-polarized analysis, separability was found to be high overall, but the separability analysis could not indicate whether or not a sample was actually composed of *P. australis* without the input of known field (training) data. In order to

used low Alpha_S values (<0.1) and high Phase values (>0.4) to classify water. After areas of land and water were classified, *P. australis* was identified as pixel values that fell between +2 and -1 standard deviations of the mean for Alpha_S and between +1 and -2 standard deviations from the mean for Phase. The same procedure as for the single-polarized classification (Section 3.4.4) was implemented. Figure 37 is the resulting map.



Figure 37: Classification map showing large patches of *P. australis* (red) identified by the model as well as areas classified as water (blue) and Other (green).

4.3.6 Accuracy Assessment of the Output Map

There were a total of 13 large patches identified as *P. australis* on the map. An examination of the field data and aerial imagery showed that there were 4 patches of *P. australis* that were present on the ground but not identified by the model. The detection accuracy of the model/map was 76% (13 of 17 correctly identified patches of *P. australis*). Ignoring patch specifics, 83% of the total area of *P. australis* interpreted from the imagery was accurately classified using this method.

All of the patches that were missed were found to be located within the interior section of the study area, away from the shoreline. Since the analysis of field data showed that these patches were poorly separable from other vegetation, it makes sense that they would not be identified by the model, given that their Touzi parameter values were significantly different when compared to the more separable patches.

Overall, the patch diameters on the map were within 30-40m of those recorded in the field for the four transects that traversed the whole patch. Given the pixel size of the imagery (8m), this can be considered an acceptable result.

5.0 Discussion and Conclusions

5.1 Single-Polarized Imagery: Significant Findings

Overall, this analysis showed that it is possible to separate *P. australis* from surrounding vegetation, given that the right combination of imagery is used and because that *P. australis* occurs in a monoculture separated from other vegetation and not spatially mixed with other vegetation. Multiple polarizations and multiple incidence angles are required in order to achieve detection accuracies of 75% for circular *P. australis* monocultures. Using image texture (e.g. GLCM Mean) produced better results in separability analysis when compared with raw image intensity values. Reducing the number of input parameters can increase the separability and also decrease the cost and complexity of image acquisition.

Since radar backscatter directly depends on the characteristics of the target being imaged it is necessary to be able to distinguish between specific targets based on physical attributes. The height differences between *P. australis* and other vegetation, along with low spring cover (more surface water interaction) are quantifiable characteristics that can improve detection given the proper polarization and incidence angle. These findings are similar to those of Pope et al. (1997) who found that classifications relied heavily upon an examination of the known relation between water levels and vegetation type such as the presence of tall emergent vegetation (sawgrass) in areas of high water.

This study showed that steep incidence angle, spring imagery at both the HH and VV polarization is best for detecting *P. australis*, but the addition of a shallow incidence angle VV image increases overall separability. It is not possible to accurately detect circular *P. australis* patches with one single-polarized image, regardless of polarization or incidence angle.

The least separable cross-class (*P. australis* vs. Other) patches of *P. australis* were those found to have texture and intensity values falling far from the average. For example, patches that did not have any surface water present obviously produced very different backscatter characteristics. When working with multiple samples from the same class of vegetation, those samples which fall far from the mean values broaden the range of values for the class. If all of these samples were included in a model, chances are that the large range would start to overlap with other vegetation classes and result in omission and commission errors. The lack of commission error found in the final model/map indicates that the methods implemented in this study are functional and fairly accurate; however, with 25% omission error on patch detection there is room for improvement. The fact that the majority of these errors occurred in one confined section of the map indicates that the model fails to capture the unique characteristics of this smaller area. Since the patch characteristics in this area are known (high surface water, low percent cover) they can be included in the model, but as stated above, this increases the risk of commission errors since the range of values included in the model will be broadened, therefore causing possible inclusion of vegetation that is not *P. australis* that possesses similar physical characteristics.

5.2 Single-Polarized Imagery: Research Limitations and Recommendations

This analysis found that *P. australis* could be detected with good accuracy, but only if three images were used (Steep HH, Steep VV, and Shallow VV). If a researcher wanted to repeat this study, only for the purpose of *P. australis* detection, it may be more suitable to use a high resolution optical image. This would be cheaper than acquiring several single-polarized radar images and more viable since patches can be easily identified in high resolution imagery. It is reasonable to believe that common 1m optical satellite imagery could perform well at this task. This analysis does show that physical characteristics, such as surface water, can be derived from the radar imagery, so it has application beyond just detecting individual patches. If optical and radar imagery were combined it may be possible to more accurately detect patches of *P. australis* using the optical imagery while at the same time deriving physical characteristics such as water presence using the radar imagery.

Omission errors were the strongest source of negative results in this study. The model could not capture very small patches (<40m in diameter) or patches of *P. australis* that were not circular monocultures. There were areas in the Big Creek study area where *P. australis* grew along small channels and were less than 3m across, however these were not used in the creation or validation of the model. The resolution of the raw imagery, combined with the speckle reduction and the production of texture images makes it impossible to detect very small patches.

The timing of the image acquisitions may have affected the results of this study since some of the images were acquired a few weeks apart. The conditions in the field did not change drastically during this time, but there might have been some variation in local water levels.

Lastly, the accuracy assessment utilized in this research was not completely independent as a trial-and-error method was used to narrow the texture values down in order to capture the greatest number of patches of *P. australis* without an excess of commission errors and some of the same sampled used to develop the classifier were used in accuracy assessment.

5.3 Quad-Polarized Imagery: Significant Findings

This analysis examined several ways in which to quantify the radar backscatter from wetland vegetation. A quick examination of the radar intensity scatter plots showed that *P. australis* displayed the most distinct signature in steep incidence angle, spring imagery. It also showed that the other vegetation classes did not display unique intensity characteristics in most of the imagery, as there was found to be a significant amount of overlap between their backscatter values. One of the most interesting findings was the amount of overlap between the vegetation and Water classes in co-polarized summer imagery. A scatter plot analysis can be used to quickly eliminate imagery that does not provide the necessary class separability.

Polarimetric plots and their associated pedestal heights provide more in-depth information on target interactions. When an average of multiple samples was used to

create these plots the backscatter characteristics of the wetland targets became clearer. Each of the four classes displayed unique features which could be used to identify similar targets throughout the study area. In addition to being able to distinguish individual classes, information about physical target characteristics could be inferred. For example, for *P. australis* there was higher response in VV, relative to HH, in the steep incidence angle spring imagery which indicated that there was a greater amount double-bounce and surface scattering and lesser amount of volume when compared the Cattail and Grass classes. This finding indicates that the structure of the vegetation is very important for surface water detection as *P. australis* provides openings for the wave to penetrate as opposed to requiring a longer wavelength (e.g. L-band) to penetrate the physical parts (leaves/stem) of the vegetation. For this study, the polarimetric plots were useful for verifying that the different classes had contrasting characteristics and some of these characteristics could be used to infer information about the physical features that would be found on the ground.

An examination of four different decomposition techniques led to several conclusions. The Van Zyl and Freeman-Durden decompositions are both simple in application and provide limited information in regards to complex scattering, however, they both provided information regarding the dominant scattering class present at each pixel and gave some insight into the amount of mixing between scatterers. This information is invaluable in terms of initial analysis. Overall, the Van Zyl decomposition cannot be used to separate vegetation classes, but it can provide some information with regards to the dominant scattering at a given location and can therefore be useful for

detecting anomalies, such as vegetated areas dominated by surface scattering. The Freeman-Durden decomposition output information similar to that of the polarimetric plots and can be considered a good first step in the analysis of the mixing of scattering types.

The Cloude-Pottier and Touzi decompositions are significantly more complex than the Van Zyl and Freeman-Durden decompositions and through the inclusion of parameters such as Entropy, Alpha_S, and Phase it is possible to derive more detailed information from targets on the ground. Since the Touzi Alpha_S and Phase parameters are unique to that particular decomposition it illustrates the value of the Touzi decomposition over previous methods for the purpose of detecting *P. australis*. Using the Cloude-Pottier and Touzi decompositions it was possible to determine that wetland vegetation, especially *P. australis*, consistently produced a complex signal as a result of multiple scattering types.

Inputting the complex decomposition parameters into a separability analysis allowed for the determination of the parameters which best characterized *P. australis* based on wave-target interactions. By first constraining the imagery for season, incidence angle, and decomposition method, separability was found to be highest using spring season imagery acquired at a steep incidence angle; the Touzi and Cloude-Pottier decomposition methods produced similar separability results. Once the imagery was narrowed down it was possible to apply a permutative analysis which allowed for the testing of all possible decomposition parameters in order to determine the optimal set

for detecting *P. australis*. In the end it was found that the Alpha_S and Phase parameters derived from the Touzi decomposition produced only slightly lower separability results than the two same parameters with the Cloude-Pottier Entropy parameter also included. As an operational method it is easier to apply just one decomposition method to a given image and it was therefore determined that the best method for detecting expansive patches of *P. australis* is with a steep incidence angle spring image with the Touzi decomposition applied. In contrast to other studies and for this specific research it was found that the use of multi-date imagery (e.g. Wang et al. 1998) and multiple incidence angles (Novo et al., 1998) did not increase detection and classification accuracy since the vegetation structure of all classes was very similar in the summer imagery and the shallower incidence angles produced very homogenous images.

In contrast to the single-polarized analysis, the *P. australis* patches with lower water levels were found to be least detectable. This may be a result of the physical location of the large patches (interior of the wetland complex), a result of physical differences between the study areas (Big Creek vs. Long Point), or as a result of the properties of the radar sensor, such as the inability of 8 m imagery to detect small patches.

Overall, the method outlined in this research is cost effective, since it requires only a single image, and straightforward, as it invokes only one decomposition method that can easily be automated in a batch process if the detection of *P. australis* is to be

done across a large area, such as the entire Lake Erie shoreline. While it is possible that optical satellite imagery may perform well at detecting *P. australis*, the data used in this study contains more information than data from previous radar sensors (e.g. higher resolution polarimetric data) and the methods have shown that fully polarized RADARSAT-2 imagery can be successfully used for vegetation discrimination and physical characteristics of vegetation types can be inferred. As new research opportunities arise, the prospect of using fully polarized radar data for vegetation applications can therefore be considered promising.

5.4 Quad Polarized Imagery: Research Limitations and Recommendations

This analysis found that *P. australis* could be detected with a high level of accuracy using only a single image and decomposition method. It was found that adding additional quad-polarized images did not increase the overall accuracy of this method. In order to obtain better results it may be possible to combine the radar imagery with optical imagery, however, this would significantly increase the cost of such a project.

Omission errors brought the overall accuracy down as a result of the inability of this method to detect patches of *P. australis* located within the interior of the wetland complex and with very low water levels. Broadening the range of values included in the mapping effort risks an increase in commission errors given that there is an overlap in decomposition parameter values across vegetation classes. This finding is consistent

with other studies where it was found that continuous water cover provides a consistent and known surface roughness and dielectric constant which simplifies wave-vegetation interactions (Hess et al., 1990).

Lastly, the inability of the quad-polarized imagery to detect smaller patches of *P. australis* may be a hindrance to early detection and removal of new *P. australis* colonies.

5.5 Conclusions

Protecting wetlands from invasion is increasingly becoming of paramount importance in Canada and across the globe. Remote sensing technology enhances the ability of researchers and organizations to monitor and control invasion in these delicate, and often remote, ecosystems. This research investigated the capacity for single-polarized and fully polarimetric radar (RADARSAT-2) to be used for the purpose of detecting the invasive common reed (*P. australis*) in southern Ontario marshlands. Using single-polarized 3m pixel radar imagery, it was shown that small, circular patches of *P. australis* could be distinguished from neighbouring vegetation types with an accuracy of approximately 75%; the best results were achieved using a combination of three images acquired in the spring: Steep HH, Steep VV, and Shallow VV.

Fully polarimetric 8m pixel imagery was found to be capable of distinguishing larger patches of *P. australis* using advanced decomposition (Cloude-Pottier, Touzi) parameters. Steep incidence angle, spring season imagery was found to produce the

highest overall detection accuracies (~75%) when decomposition parameters (Alpha_S, Phase) were extracted. The physical characteristics of the wetland vegetation (density, water level, height) played a direct role in the detection of *P. australis*.

This research aimed to apply existing methods and technologies to an application (vegetation discrimination) that has not received a lot of attention from researchers using SAR technology. The utility of these methods proved to be fairly successful and it is likely that similar work can expand upon the positive findings presented in this study.

REFERENCES

- Arzandeh, S., and Wang, J. 2003. Monitoring the change of *Phragmites* distribution using satellite data. *Canadian Journal of Remote Sensing*, 20: 24-35.
- Augusteijn, M. and Warrender, C. 1998. Wetland classification using optical and radar data and neural network classification. *International Journal of Remote Sensing*, 19: 1545–1560.
- Bourgeau-Chavez, L., Kasischke, E., Brunzell, S., Mudd, J., Smith, K. and Frick, A. 2001. Analysis of space-borne SAR data for wetland mapping in Virginia riparian ecosystems. *International Journal of Remote Sensing*, 22: 3665–3687.
- Bourgeau-Chavez, L.L., Kasischke, E.S., and Smith, K. 1996. Using satellite radar imagery to monitor flood conditions in wetland ecosystems of southern Florida. *Proceedings EUROPTO Series, Taormina, Italy, 23-26 September 1996*, 29-59.
- Brady, N. C., and Weil, R.R. 2002. *The Nature and Properties of Soils*. New Jersey: Prentice Hall. 960p.
- Buckley, Y.M. 2008. The role of research for integrated management of invasive species, invaded landscapes and communities. *Journal of Applied Ecology*, 45: 397-402.
- Canadian Space Agency. 2008. Radarsat-2 Information Resources. <http://www.radarsat2.info/> [cited 2 December 2010]
- Canada Centre for Remote Sensing. 2008. Educational Resources for Radar Remote Sensing. <http://www.ccrs.nrcan.gc.ca/> [cited 9 January 2010]
- CCRS. 2001. Table 1. <http://www.ccrs.nrcan.gc.ca/> [cited 9 January 2010]
- Chambers, R., Meyerson, L. and Saltonstall, K. 1999. Expansion of *Phragmites australis* into tidal wetlands of North America. *Aquatic Botany*, 64: 261–273.
- Chanton, J., Whiting, G., Happell, J. and Gerard, G. 1993. Contrasting rates and diurnal patterns of methane emission from emergent aquatic macrophytes. *Aquatic Botany*, 46: 111–128.
- Cloude, S.R., and Pottier, E. 1996. A review of target decomposition theorems in radar polarimetry. *IEEE Transactions on Geoscience and Remote Sensing*, 34 :498-518.
- Coops, H., Geilen, N., Verheij, H., Boeters, R. and van der Velde, G. 1996. Interactions between waves, bank erosion, and emergent vegetation: an experimental study in a wave tank. *Aquatic Botany*, 53: 187–198.
- Cooper, P. F., Hobson, J. A. and Findlater, C. 1990. The use of reed bed treatment systems in the UK. *Water Science Technology*, 22: 57–64.

- Costa, M. and Telmer, K. 2006. Utilizing SAR imagery and aquatic vegetation to map fresh and brackish lakes in the Brazilian Pantanal wetland. *Remote Sensing of Environment*, 105: 204-213.
- Crevier, Y., Pultz, T., Lukowski, T. and Toutin, T. 1996. Temporal analysis of ERS-1 SAR backscatter for hydrology applications. *Canadian Journal of Remote Sensing*, 22: 65–77
- Cronk, J., and Fennessy, M.S. 2001. *Wetland Plants: Biology and Ecology*. London: CRC Press, Taylor & Francis Group. 462p.
- Crowder, A.A., and Bristow, J.M. 1988. The future of waterfowl habitats in the Canadian lower Great Lakes wetlands. *Journal of Great Lakes Research*, 14: 115-127.
- Daily, G.C., Alexander S., Ehrlich P.R., Goulder L., Lubchenco J. 1997. Ecosystem services: Benefits supplied to human societies by natural ecosystems. *Issues in Ecology*, 1: 1-18.
- Duke, J.A. 1983. Handbook of energy crops [online]. Available from http://www.hort.purdue.edu/newcrop/duke_energy/Phragmites_australis.html [cited 14 February 2010].
- Dunbabin, J. and Bowmer, K. 1992. Potential use of constructed wetlands for treatment of industrial wastewaters containing metals. *Science of the Total Environment*, 111: 151–168.
- Environment Canada. 2009. Long Point National Wildlife Area. http://www.on.ec.gc.ca/wildlife/nwa/eng/longpoint/longpoint_htm-e.html [cited 20 February 2010]
- Foley, J. A., DeFries, R., Asner, G.P., Barford, C., Bonan, G., Carpenter, S.R. 2005. Global consequences of land use. *Science*, 309: 570-574.
- Frappart, F., Seyler, F., Martinez, J.-M., Leo´ N, J.G. and Cazenave, A. 2005. Floodplain water storage in the Negro River basin estimated from microwave remote sensing of inundation area and water levels. *Remote Sensing of Environment*, 99: 387–399.
- Freeman, A., and Durden, S.L. 1998. A three-component model for polarimetric SAR imagery. *IEEE Transactions on Geoscience and Remote Sensing*, 34: 963-973.
- Frost, V.S. 1982. A model for radar images and its application to adaptive digital filtering of multiplicative noise. *IEEE Transactions on Pattern Analysis & Machine Intelligence*, N PAMI-4, 2.
- Gassner, W. and Neugebohrn, L. 1994. The significance of higher plants for degradation of phenols in aquatic systems. *Archaeological Hydrobiology*, 31: 129.

- Grenier, M., A-M. Demers, S. Labrecque, M. Benoit, R. A. Fournier, and B. Drolet. 2007. An object-based method to map wetland using RADARSAT-1 and Landsat ETM images: test case on two sites in Quebec, Canada. *Canadian Journal of Remote Sensing*, 33: 28-45.
- Hansen, R.M. 1978. Shasta ground sloth food habits, Rampart Cave, Arizona. *Paleobiology*, 4: 302-319.
- Henderson, H. and Lewis, L. 2008. Radar detection of wetland ecosystems: a review. *International Journal of Remote Sensing*, 29: 5809-5835.
- Herdendorf, C.E. 1992. Lake Erie coastal wetlands: an overview. *Journal of Great Lakes Research*, 18: 533-551.
- Hess, L.L., Melack, J.M., Filoso, S., and Wang, Y. 1995. Delineation of inundated area and vegetation along the Amazon floodplain with SIR-C synthetic aperture radar. *IEEE Transactions on Geoscience and Remote Sensing*, 33: 896-904.
- Hess, L., Melack, J. and Simonett, D. 1990. Radar detection of flooding beneath the forest canopy: a review. *International Journal of Remote Sensing*, 11: 1313-1325.
- Hocking, P. J., Finlayson, C. M. and Chick, A. J. 1983. The biology of Australian weeds. 12. *Phragmites australis* (Cav.) Trin. ex Steud. *Australian Institute of Agricultural Research*, 49: 123-132.
- Horowitz, P., Lindsay, M., and O'Connor, M. 2001. Biodiversity, endemism, sense of place and public health: inter-relationships for Australian inland aquatic systems. *Ecosystem Health*, 7: 253-265.
- Jensen, J.R. 2007. *Remote Sensing of the Environment: An Earth Resource Perspective*. Prentice Hall: NJ.
- Kasischke, E. and Bourgeau-Chavez, L., 1997. Monitoring south Florida wetlands using ERS-1 SAR imagery. *Photogrammetric Engineering and Remote Sensing*, 63: 281-291.
- Kasischke, E., Smith, K., Bourgeau-Chavez, L., Romanowics, E., Brunzell, S. and Richardson, C., 2003. Effects of seasonal hydrologic patterns in south Florida wetlands on radar backscatter measured from ERS-2 SAR imagery. *Remote Sensing of Environment*, 88: 423-441.
- Kuan, D.T., Sawchuk, A.A., Strand, T.C., and Chavel, P. 1987. Adaptive restoration of images with speckle. *IEEE Transactions on Acoustic Speech and Signal Processing*, 35: 373-383.
- Lavoie, C. 2008. The Common Reed (*Phragmites australis*): A Threat to Quebec's Wetlands? *Report for the Government of Quebec's Interministerial Committee on the common reed for Ducks Unlimited Canada*, 1-41.

- Lee, J. 1981. Speckle analysis and smoothing of synthetic aperture radar images. *Computer Graphics and Image Processing*, 17: 24-32.
- Lee, J.S., Jurkevich, I. 1994. Speckle filtering of synthetic aperture radar images: A review. *Remote Sensing Reviews*, 8: 313-340.
- Li, J., and W. Chen. 2005. A rule-based method for mapping Canada's wetlands using optical, radar and DEM data. *International Journal of Remote Sensing*, 26: 5051-5069.
- Lillesand, T.M., Keifer, R.W., Chipman, J.W. 2004. Remote Sensing and Image Interpretation. 5th ed. Wiley and Sons: NJ.
- Lopes, A., Touzi, R., and Nezry, E. 1990. Adaptive speckle filters and scene heterogeneity. *IEEE Transactions on Geoscience and Remote Sensing*, 28: 992-1000.
- Mal, T.K., Narine, L. 2003. The biology of Canadian weeds. 129. *Phragmites australis* (Cav.) Trin. Ex. Steud. *Canadian Journal of Plant Science*, 84: 265-396.
- Manual, P. M. 2003. Cultural perceptions of small urban wetlands: cases from the Halifax regional municipality, Nova Scotia, Canada. *Wetlands*, 23: 921-940.
- Marks, M., Lapin, B. and Randall, J. 1994. *Phragmites australis* (*P. communis*): Threats, management and monitoring. *Natural Areas Journal*, 14: 285-294.
- Meindl, C. F. 2004. Southerners and their swamps: the view from middle Georgia. *Southeastern Geographer*, 44: 74-89.
- Millennium Ecosystem Assessment. 2005. Ecosystems and Human Well Being. Wetlands and Water Synthesis (Washington, DC: World Resources Institute).
- Mitsch, W.J., and Gosselink, J.G. 2007. Wetlands. Hoboken: John Wiley & Sons, Inc. p. 582.
- Morrissey, L., Durden, S., Livingston, G., Stearn, J. and Guild, L. 1996. Differentiating methane source areas in Arctic environments with multitemporal ERS-1 SAR data. *IEEE Transactions on Geoscience and Remote Sensing*, 34: 667-672.
- Mougin, E., Proisy, C., Fromard, M.F., Puig, H., Betoulle, J.L. and Rudant, J.P. 1999. Multifrequency and multipolarization radar backscattering from mangrove forests. *IEEE Transactions on Geoscience and Remote Sensing*, 37: 94-102.
- National Wetlands Working Group. 1988. Wetlands of Canada. Ecological Land Classification Series No. 24. Sustainable Development Branch, Environment Canada, Ottawa, Ontario, and Polyscience Publications Inc., Montreal, Quebec. 452p.

- National Wetlands Working Group. 1997. The Canadian Wetland Classification System, Second Edition. Eds. B.G. Warner and C.D.A. Rubec. Wetlands Research Centre, University of Waterloo, Waterloo, Ontario. 68p.
- Novitzki, R., Smith, R. and Fretwell, J. 1996. Wetland functions, values and assessment. In National Water Summary on Wetland Resources, USGS Water Supply Paper 2425, J. Fretwell, J. Williams and P. Redman (compilers), pp. 79–86 (Washington, DC: U.S. Geological Survey).
- Novo, E.M., Costa, M.F. and Mantovani, J. 1998. Exploratory survey on macrophyte biophysical parameters in tropical reservoirs. *Canadian Journal of Remote Sensing*, 24: 367–375.
- Ormsby, J.P., Blanchard, B.J., and Blanchard, A.J. 1985. Detection of lowland flooding using active microwave systems. *Photogrammetric Engineering and Remote Sensing*, 51: 317-328.
- Petrie, S.A. 1998. Waterfowl and Wetlands of Long Point Bay and Old Norfolk County: Present Conditions and Future Options for Conservation. *Unpublished Norfolk Land Stewardship Council Report*. Long Point Waterfowl and Wetlands Research Fund, Port Rowan, Ontario.
- Pope, K., Rejmankova, E., Paris, J. and Woodruff, R. 1997. Detecting seasonal flooding cycles in marshes of the Yucatan peninsula with SIR-C polarimetric radar imagery. *Remote Sensing of Environment*, 59: 157–166.
- Pope, K.O., Rey-Benayas, J.M., and Paris, J.F. 1994. Radar remote sensing of forest and wetland ecosystems in the Central American tropics. *Remote Sensing of Environment*, 48: 205-219.
- Poulter, B., Christensen Jr., N.L., and Halpin, P.N. 2006. Carbon emissions from a temperate peat fire and its relevance to interannual variability of trace atmospheric greenhouse gases. *Journal of Geophysical Research*, 111: 1-11.
- Pultz, T.J., and Brown, R.J. 1987. SAR Image Classification of Agricultural Targets Using First and Second-Order Statistics. *Canadian Journal of Remote Sensing*, 13: 85-91.
- Racine, M.-J., Bernier, M. and Ouarda, T. 2005. Evaluation of RADARSAT-1 images acquired in fine mode for the study of boreal peatlands: a case study in James Bay, Canada. *Canadian Journal of Remote Sensing*, 31: 450–467.
- Ramsey, E., III. 1995. Monitoring flooding in coastal wetlands by using radar imagery and ground-based measurements. *International Journal of Remote Sensing*, 16: 2495–2505.

- Ramsey, E. W. 1998. Radar remote sensing of wetlands *IN* Remote Sensing Change Detection: Environmental Monitoring Methods and Applications. Eds. R.S. Lunetta and C.D Elvidge. Chelsea: Sleeping Bear Press, Inc. 318p.
- Ramsey, E., III, Nelson, G., Sapkota, S., Laine, S., Verdi J. and Krasznay, S. 1999. Using multiple-polarization L-band radar to monitor marsh burn recovery. *IEEE Transactions on Geoscience and Remote Sensing*, 37: 635–639.
- Rice, D., Rooth, J., and Stevenson, J.C. 2000. Colonization and expansion of *Phragmites australis* in upper Chesapeake Bay tidal marshes. *Wetlands*, 20: 280-299.
- Richards, J.A. 1994. Remote Sensing digital image analysis: An Introduction. Springer-Verlag, New York.
- Richards, J.A., Woodgate, P.W., and Skidmore, A.K. 1987. An explanation of enhanced radar backscatter from flooded forests. *International Journal of Remote Sensing*, 8: 1093-1100.
- Saltonstall, K. 2002. Cryptic invasion by a non-native genotype of the common reed, *Phragmites australis*, into North America. *Proceedings of the National Academy of Science*, 99: 2445–2449.
- Schleyer, M. and Roberts, G. 1987. Detritus cycling in a shallow coastal lagoon in Natal, South Africa. *Journal of Experimental Marine Biology and Ecology*, 110: 27–40.
- Sgrenzaroli, M., Baraldi, A., De Grandi, G.D., Eva, H. and Achard, F. 2004. A novel approach to the classification of regional-scale radar mosaics for tropical vegetation mapping. *IEEE Transactions on Geoscience and Remote Sensing*, 42: 2654–2669.
- Simard, J., Degrandi, G., Saatchi, S. and Mayaux, P. 2002. Mapping tropical coastal vegetation using JERS-1 and ERS-1 radar data with a decision tree classifier. *International Journal of Remote Sensing*, 23: 1461–1474.
- Smith, P.G., Glooschenko, V., and Hagan, D.A. 1991. Coastal wetlands of three Canadian Great Lakes: Inventory, current conservation initiatives, and patterns of variation. *Canadian Journal of Fish and Aquatic Science* 48: 1581-1594.
- Soil Classification Working Group. 1998. The Canadian System of Soil Classification. Agriculture and Agri-Food Canada Publishing, 1646 (Revised) 187p.
- Sokol, J. 2003. Monitoring Northern Atlantic Canadian Wetlands using Remote Sensing Techniques. *Carleton University Masters Thesis*, 88-93.
- Tanis, F.J., Bourgeau-Chavez, L.L., and Dobson, M.C. 1994. Applications of ERS-1 SAR for coastal inundation. *Proceedings of the International Geoscience and Remote Sensing Symposium (IGARSS'94), Pasadena, California, 8-12 August 1994*, IEEE Catalog No. 94CH3378-7, 1481-1483.

- Touzi, R., Deschamps, A., and Rother, G. 2009. Phase of target scattering for wetland characterization using polarimetric C-band SAR. *IEEE Transactions on Geoscience and Remote Sensing*, 47: 3241-3261.
- Touzi, R., Deschamps, A. Rother, G. 2007. Wetland characterization using polarimetric RADARSAT-2 capability. *Canadian Journal of Remote Sensing*, 33: 56-67.
- Treitz, P.M. and Howarth, P.J. 2000. High Spatial Resolution Remote Sensing Data for Forest Ecosystem Classification: - An Examination of Spatial Scale. *Remote Sensing of Environment*, 72: 268-289.
- Treitz, P.M., Howarth, P.J., Rotunno Filo, O., and Soulis, E.D. 2000. Agricultural Crop Classification using SAR Tone and Texture Statistics. *Canadian Journal of Remote Sensing*, 26: 18-29.
- Tu, M. Hurd, C., and Randall, J.M. 2001. Weed Control Methods Handbook: Tools and Techniques for Use in Natural Areas. Available from <<http://tncweeds.ucdavis.edu/handbook.html>> [cited 18 February 2010]
- van Zyl, J., Zebker, H., and Elachi, C. 1987. Imaging radar polarization signatures: Theory and observation. *Radio Science*, 22: 529-543.
- Verhoeven, J.T.A., Arheimer, B., Yin, C., and Hefting, M.M. 2006. Regional and global concerns over wetlands and water quality. *TRENDS in Ecology and Evolution*, 21: 96-103.
- Walfir, P., Souza Filho, M. and Renato Pardella, W. 2005. Use of RADARSAT-1 fine mode and Landsat-5 TM selective principal component analysis for geomorphological mapping in a macrotidal mangrove coast in the Amazon Region. *Canadian Journal of Remote Sensing*, 31: 214-224.
- Wang, J., Shang, J., Brisco, B. and Brown, R. 1998. Evaluation of multirate ERS-1 and multispectral Landsat imagery for wetland detection in Southern Ontario. *Canadian Journal of Remote Sensing*, 24: 60-68.
- Ward, R.C., and Robinson, M. 2000. Principles of Hydrology. London: McGraw-Hill Publishing Company. 450p.
- Wikum, D.A., and Shanholtzer, G.F. 1978. Application of the Braun-Blanquet cover-abundance scale for vegetation analysis in land development studies. *Environmental Management*, 2: 323-329.
- Wilcox, K.L., Petrie, S.A., Maynard, L.A., Meyer, S.W. 2003. Historical distribution and abundance of *Phragmites australis* at Long Point, Lake Erie, Ontario. *Journal of Great Lakes Research*, 29: 664-680.

- Windham, L. and Lathrop, R. G. 1999. Effects of *Phragmites australis* (common reed) invasion on aboveground biomass and soil properties in brackish tidal marsh of the Mullica River, New Jersey. *Estuaries*, 22: 927–935.
- Winter, T.C., and Llamas, M.R. 1993. Introduction to the 28th International Geological Congress Symposium on the Hydrogeology of Wetlands. *Journal of Hydrology*, 141:1-3.
- Woodward, R. T., and Y-S Wui. 2001. The economic value of wetland services: a meta-analysis. *Ecological Economics*, 37: 257-270.
- Yamagata, Y. and Yasuoka, Y. 1993. Classification of wetland vegetation by texture analysis methods using ERS-1 and JERS-1 images, Proceedings of IGARSS'93, 4: 1614-1616

APPENDIX 1

Scatter plots displaying the cross-polarized (VV/HV) intensity ratios for the spring and summer quad-pol imagery at varying incidence angles.

